

**Method Development for Approximate Density Functional Theory
and
Applications to Complex Molecular Systems**

(近似的密度汎関数法のための手法開発と複雑な分子系への応用)

NISHIMOTO Yoshio

西本 佳央

Contents

1	Introduction	1
	Bibliography	4
2	Theoretical Backgrounds	8
2.1	Many-Electron Problems to Hartree-Fock Approximation	8
2.2	Density Functional Theory	11
2.3	Density Functional Tight Binding Method	15
2.3.1	Tight-Binding Theory and Nonself-Consistent-Charge (NCC) DFTB	16
2.3.2	Self-Consistent-Charge (SCC) DFTB	17
2.3.3	Further Extensions of DFTB	19
2.3.4	Electronic Temperature	23
2.4	Fragment Molecular Orbital (FMO) Approach	24
	Bibliography	25
3	Density-Functional Tight-Binding Combined with the Fragment Molecular Orbital Method	29
3.1	Introduction	29
3.2	Methodology	31
3.2.1	Density-Functional Tight-Binding (DFTB).	31
3.2.2	Formulation of FMO-DFTB	33
3.2.3	Gradient of FMO-DFTB	36
3.2.4	Dispersion Interaction for FMO-DFTB	37
3.2.5	Computational Details	38
3.3	Results and Discussion	40
3.3.1	Accuracy of FMO-DFTB	40
3.3.2	Scaling of FMO-DFTB	49
3.3.3	Parallelization of FMO-DFTB and Its Application to a Fullerite Geometry Optimization	52
3.4	Conclusions	53
	Bibliography	54
4	Simulation of Vibrational Spectra of Large Molecular Systems with Radical or Metallic Electronic Structure	60

4.1 Introduction	60
4.2 Methodology	61
4.3 Results and Discussion	62
4.3.1 Benchmark Calculation with Nitronyl Nitroxide Radicals	62
4.3.2 Theoretical IR and Raman Spectra of Polyanulene	63
4.3.3 Computational Timings of Numerical and Analytical Second Derivatives	65
4.4 Summary	66
Computational Details	67
Bibliography	67
 5 Super-Reduced Polyoxometalates: Excellent Molecular Cluster Battery Components and Semipermeable Molecular Capacitors	 72
5.1 Introduction	72
5.2 Computational Details	74
5.3 Results and Discussion	75
5.3.1 Molecular Structure of the Negative Keggin POM ³⁻	75
5.3.2 Strategies for Modeling the Molecular and Electronic Structures of Reduced POMs	77
5.3.3 Geometry Optimizations of Super-Reduced POMs	78
5.3.4 Molecular Dynamics Simulations of Super-Reduced POMs	79
5.3.5 Four Metal Atom Triangles in Super-Reduced Keggin POMs	83
5.3.6 MO Analysis of POM Super-Reduction	84
5.3.7 Super-Reduced POM ²⁷⁻ as a Semipermeable Molecular Capacitor	88
5.3.8 Reversibility of the Structural Changes	90
5.3.9 Design Principles for Improved MCB Cathod Materials	92
5.4 Summary	92
Bibliography	94
 6 Summary and Outlook	 98
 Acknowledgement	 101
 Appendix	 102

A. Derivation of Second-Order Geometrical Derivatives of Free Energy for Density-Functional Tight-Binding (DFTB) Method with Fractional Occupation Numbers (FONs)	102
B. Structures and Vibrational Frequencies of Nitroxyl Radicals	113
C. Molecular Dynamics Simulations of Super-Reduced POM with Sodium Atoms	115
Bibliography	117
List of Publications	118

Chapter 1

Introduction

Acceleration in increasing of computer power has enabled us to witness tremendous achievements in theoretical and computational research. As having predicted by Moore in 1965,^{1,2} CPU power has been increased roughly twice per year, known as Moore's law, and this fact has opened many new fields of computational research up. The concept of the modern computer was first introduced by Turing in 1936,³ and Zuse build a set of first computers called Z1 to Z4 between 1936 and 1945.⁴ After about 70 years from the birth of the working tool, almost all human beings are blessed with very powerful and efficient, and yet small and cheap, equipment, and it is very common that researcher has their own *personal* computers and work with it in processing obtained data and writing papers. As a result of wide spreading of amazingly useful tool, theoretical investigation particularly with computer is no longer an exclusive means for theoreticians but is now routinely available approach even for experimentalists. Of course, a plenty of computational resources is helpful for theoreticians too, in that they have strengthened the power of cutting-edge methodologies such as, for instance, linear-scaling methods⁵⁻⁷ and highly parallel computing programs.⁸⁻¹⁰

However, theoreticians' pursue of truly useful computational method for many possible practical applications is still on the endless way. Although it is generally known that full configuration interaction (FCI)¹¹ gives the exact solution of considered system under the non-relativistic time-independent particles with Born-Oppenheimer approximation, its computational cost is out of question in terms of application.^{12,13} Theoreticians have imported many appropriate approximations and have developed so called wave function methods such as Hartree-Fock (HF),¹¹ perturbation theory such as MP2,¹⁴⁻¹⁷ configuration interaction (CI), and coupled cluster (CC)^{11,18} methods, and as another stream of development, the well-known density functional theory (DFT),^{19,20} which originally comes from electron-gas theory founded by Thomas and Fermi in 1927.^{21,22} The development of DFT enriched many tools which are easily handled by chemists who engages themselves experiments on work station machines. The most representative term is the "Gaussian" as a package of quantum mechanics (QM) calculation. It is now very common that theoretical investigation occupies a part of discussion in many experiment papers.

As some simple calculations are now done by experimentalists, theoreticians have to consider how they help experimentalists. Although there have been many

studies using QM calculations particularly utilizing the efficiency and accuracy of DFT recently, they have one pitfall: the computational cost of QM calculations scales formally at least cubic ($O(N^3)$) to system size N . The reason of the cubic scaling is attributed to the diagonalization step of Fock matrix which describes electron-electron and electron-nuclear interaction in the system of interest. Post Hartree-Fock calculations, what is worse, scales as $O(N^7)$ in the case of CC with single and double excitations and perturbative triples. This means that doubling a system results in being required more than hundred times more expensive computation. One possible solution is adding further approximations so as to omit the diagonalization and the calculation of electron correlation steps. This primitive idea generated molecular mechanics (MM) method based on Newton’s laws of motion with classical force field, which describes the interaction between a pair of atom using a kind of harmonic potential. One-million-atom molecular dynamics (MD) simulation of the complete satellite tobacco mosaic virus has been reported in 2006²³ using one of the most powerful, massive parallel supercomputers. Since force field parameters are usually optimized for specific systems such as proteins and DNAs,²⁴⁻²⁶ we can perform long simulations in a good accuracy, in terms of energy and geometry, for these systems. However, unfortunately, force field calculations have some limitations. For example, it is well-known that force field calculation is particularly poor at describing bond formation and cleavage during simulation, because one has to assign atom type before simulation. This deficiency is critical when MM method is applied for chemical reactions. In the view of material science and enzymes, it is important to consider chemical reactions and charge transfer effect and even excited state, therefore force field calculation is not generally be warmly welcomed in these regions.

Another possible solution is dividing a target molecule into pieces. Since the behavior of steep scaling becomes significant only when the target system is bigger, the computational cost of small piece of large molecule must be very low. The idea of fragmentation is that summation of energies of small fragments up recovers the total energy of the whole large molecule. Such a fragmentation method is nowadays famous for the names of fragment molecular orbital (FMO)²⁷⁻³¹ or divide-and-conquer (DC)^{7,32,33} for example. The concept of FMO method is very close to our intuition: large molecule is divided into fragments (monomers) and obtain the density of each monomer self-consistently. Total energy of the system is recovered by arithmetically manipulating the energies of monomers and dimers/trimers. The latter, DC, method recovers density matrix by summing that of each subsystem up, and therefore this method is more oriented to physics. Although the scaling of these methods is generally close to linear,

applications have been limited to a few hundred thousand atoms,³⁴ which is still not sufficient for full simulation of proteins. Calculation of each fragment is much faster than the calculation of a full system, however the pre-factor of *ab initio* methods is not negligibly small. One motivation in this thesis is to develop a method with low pre-factor. Chapter 3 discusses such method utilizing a semi-empirical method based on DFT and demonstrates that the method beats the barrier of one-million-atom calculation with QM method.

Although structure and its stability, which are determined by the zeroth- and first-order geometrical derivatives of the total energy, are of significantly importance in understanding structural properties, the second-order derivative also tells much information in identifying and predicting vibrational properties such as infrared (IR) and Raman spectroscopy, for instance. There are a number of spectroscopic research of nanomaterials,³⁵⁻³⁷ however that of GNRs is rather limited.^{38,39} It can be attributed to the fact that the synthesis of high-quality GNRs with smooth edges and narrow and constant widths is of great difficulty, even with many possible experimental methods for GNR synthesis.⁴⁰ In terms of theoretically work, on the other hand, extended systems exhibit open-shell character which is very hard for ordinary DFT and even DFTB to tackle with. Not only methodological difficulty, computational cost is also an embarrassing problem. The motivation here is to develop a method which is applicable for large open-shell molecular systems with low computational cost. Because of economic computational cost of DFTB, the development of such a method along with DFTB must be one of the best approaches. This work focuses on the derivation and the application of second-order geometrical derivatives to open-shell GNRs with DFTB wave function in Chapter 4.

Development of a new method certainly helps the activity of theoreticians, however scientists', including theoreticians, goal should be to contribute to the improvement of our lives. In this sense, development of method is only a start point of the theoreticians' contribution to our lives. Apart from this approach, how can a theoretician contribute to society? The role of theoreticians is not to produce a visible entity but rather to support the activity of experimentalists, such as giving a strategy and an insight for a better molecule/material and uncovering a hidden physical background of observed phenomenon. Although experimentalists lately do theoretical works to support their ideas by themselves, some difficulties remain in many fields of science. One difficult and yet important field of science for both experimental and theoretical work is the development of rechargeable battery,⁴¹⁻⁴³ whose importance is growing because of rapid spread of portable devices. Strong demanding of stable battery with high

efficiency and large capacity stirs up both experimentalists and theoreticians to develop better materials. In spite of a number of experimental efforts, atom-resolved properties are not very well understood due to the limit of current experimental technique. Recent experimental findings of molecular cluster batteries (MCBs)⁴⁴⁻⁴⁸ have accelerated its possibility of applications as a cathode active material of rechargeable battery. Experimental observations have revealed the high discharging capacity and fast discharging property. These advantages of MCBs are attributed to the multi-step reduction of metal complex which is easily reduced and oxidized repeatedly and to their large surface area to contact with lithium atoms. The highest capacity reached 320 Ah/kg as a hybrid with carbon nanotube.⁴⁶ In spite of promising high capacity, atom-resolved properties of cathode active material in MCBs are almost unknown yet. Molecule consisting of cathode active material exhibits a “super-reduced state” in the discharging process. As can be guessed, molecules at super-reduced state is so unstable that only partial information is experimentally available.^{47,48} The present work focuses on the theoretical prediction of structural and electronic properties of the super-reduced polyoxometalate (POM²⁷⁻)^{46,48} cluster through fast DFT calculation. This work, including suggestions of strategies for improved material, is explained in Chapter 5 in detail.

The rest of the thesis is organized as follows. In Chapter 2, important theoretical aspects of DFT and DFTB methods and FMO approach are briefly presented. In Chapter 3, the combination of FMO approach with DFTB method is founded and its applicability is investigated. In Chapter 4, the derivation of second-order geometrical derivatives for open-shell molecular systems and the application of for GNRs are briefly presented. In Chapter 5, the details of the computation, results, and possible future design strategy of POM are discussed. Finally, conclusions and future prospects of these works are shown in Chapter 6.

Bibliography

- (1) Moore, G. E. *Electronic* **1965**, 38, 114-117.
- (2) Moore, G. E. *Proc. IEEE* **1998**, 86, 82-85.
- (3) Turing, A. M. *Proc. London Math. Soc.* **1937**, s2-42, 230-265.
- (4) Rojas, R. The Zuse Computers. In *Computer RESURRECTION The Bulletin of the Computer Conservation Society*; Enticknap N., Eds.; British Computer Society: UK, 2006; pp 8-13.
- (5) Goedecker, S. *Rev. Mod. Phys.* **1999**, 71, 1086-1123.

- (6) Ochsenfeld, C.; Kussmann, J.; Lambrecht, D. S. Linear-Scaling Methods in Quantum Chemistry. In *Reviews in Computational Chemistry*; Lipkowitz, K. B., Boyd, D. B., Cundari, T. R., Eds.; John Wiley & Sons, Inc.: Hoboken, New Jersey, 1996; Vol. 23, pp 1-82.
- (7) *Linear-Scaling Techniques in Computational Chemistry and Physics*; Zalesny, R., Papadopoulos, M. G., Mezey, P. G., Leszczynski, J., Eds.; Springer: New York, 2011.
- (8) Schmidt, N. W.; Baldrige, K. K.; Boatz, J. A.; Elbert, S. T.; Gordon, M. S.; Jensen, J. H.; Koseki, S.; Matsunaga, N.; Nguyen, K. A.; Su, S.; Windus, T. L.; Dupuis, M.; Montgomery, J. A. *J. Comput. Chem.* **1993**, *14*, 1347-1363.
- (9) Valiev, M.; Bylaska, E. J.; Govind, N.; Kowalski, K.; Straatsma, T. P.; van Dam, H. J. J.; Wang, D.; Niepolocha, J.; Apra, E.; Windus, T. L.; de Jong, W. A. *Comput. Phys. Commun.* **2010**, *181*, 1477-1489.
- (10) Werner, H.-J.; Knowles, P. J.; Knizia, G.; Manby, F. R.; Schütz, M. *WIREs Comput. Mol. Sci.* **2012**, *2*, 242-253.
- (11) Szabo, A.; Ostlund, N. S. *Modern Quantum Chemistry: Introduction to Advanced Electronic Structure Theory*; Macmillan Publishing Co., Inc.: New York, 1982.
- (12) Knowles, P. J.; Handy, N. C. *Chem. Phys. Lett.* **1984**, *111*, 315-321.
- (13) Olsen, J.; Roos, B. O.; Jørgensen, P.; Aa. Jensen, H. J. *J. Chem. Phys.* **1988**, *89*, 2185-2192.
- (14) Head-Gordon, M.; Pople, J. A.; Frisch, M. J. *Chem. Phys. Lett.* **1988**, *153*, 503-506.
- (15) Frisch, M. J.; Head-Gordon, M.; Pople, J. A. *Chem. Phys. Lett.* **1990**, *166*, 275-280.
- (16) Frisch, M. J.; Head-Gordon, M.; Pople, J. A. *Chem. Phys. Lett.* **1990**, *166*, 281-289.
- (17) Head-Gordon, M.; Head-Gordon, T. *Chem. Phys. Lett.* **1994**, *220*, 122-128.
- (18) Barless, R. J.; Musiał, M. *Rev. Mod. Phys.* **2007**, *79*, 291-352.
- (19) Hohenberg, P.; Kohn, W. *Phys. Rev.* **1964**, *136*, B864-B871.
- (20) Kohn, W.; Sham, L. J. *Phys. Rev.* **1965**, *140*, A1133-A1138.
- (21) Thomas, L. H. *Proc. Cambridge Phil. Soc.* **1927**, *23*, 542-548.
- (22) Fermi, E. *Rend. Accad. Naz. Lincei* **1927**, *6*, 602-607.
- (23) Freddolino, P. L.; Arkhipov, A. S.; Larson, S. B.; McPherson, A.; Schulten, K. *Structure* **2006**, *14*, 437-449.
- (24) Rappé, A. K.; Casewit, C. J.; Colwell, K. S.; Goddard III, W. A.; Skiff, W. M. *J. Am. Chem. Soc.* **1992**, *114*, 10024-10035.

- (25) Cornell, W. D.; Cieplak, P.; Bayly, C. I.; Gould, I. R.; Merz, K. M.; Ferguson, D. M.; Spellmeyer, D. C.; Fox, T.; Caldwell, J. W.; Kollman, P. A. *J Am. Chem. Soc.* **1995**, *117*, 5179-5197.
- (26) Jorgensen, W. L.; Maxwell, D. S.; Tirado-Rives, J. *J. Am. Chem. Soc.* **1996**, *118*, 11225-11236.
- (27) Kitaura, K.; Ikeo, E.; Asada, T.; Nakano, T.; Uebayasi, M. *Chem. Phys. Lett.* **1999**, *313*, 701-706.
- (28) *The Fragment Molecular Orbital Method: Practical Applications to Large Molecular Systems*; Fedorov, D. G., Kitaura, K., Eds.; CRC Press: Boca Raton, FL, 2009.
- (29) Fedorov, D. G.; Kitaura, K. *J. Phys. Chem. A* **2007**, *111*, 6904-6914.
- (30) Fedorov, D. G.; Nagata, T.; Kitaura, K. *Phys. Chem. Chem. Phys.* **2012**, *14*, 7562-7577.
- (31) Tanaka, S.; Mochizuki, Y.; Komeiji, Y.; Okiyama, Y.; Fukuzawa, K. *Phys. Chem. Chem. Phys.* **2014**, *16*, 10310-10344.
- (32) Yang, W.; Lee, T.-S. *J. Chem. Phys.* **1995**, *103*, 5674-5678.
- (33) Akama, T.; Kobayashi, M.; Nakai, H. *J. Comput. Chem.* **2007**, *28*, 2003-2012.
- (34) Canfield, P.; Dahlbom, M. G.; Hush, N. S.; Reimers, J. R. *J. Chem. Phys.* **2006**, *124*, 024301.
- (35) *Raman Spectroscopy for Nanomaterials Characterization*; Kumar, C. S. S. R., Ed.; Springer – Verlag: Berlin, 2012.
- (36) *Chemistry of Nanocarbons*; Akasaka, T., Wudl, F., Nagase, S., Eds.; John Wiley & Sons, Ltd. Publication: Chichester, U.K., 2010.
- (37) Reichenbacher, M.; Popp, J.; *Challenges in Molecular Structure Determination*; Springer – Verlag: Berlin, 2012.
- (38) Kosynkin, D. V.; Higginbotham, A. L.; Sinitskii, A.; Lomeda, J. R.; Dimiev, A.; Price, B. K.; Tour, J. M. *Nature* **2009**, *458*, 872-876.
- (39) Chitara, B.; Panchakarla, L. S.; Krupanidhi, S. B.; Rao, C. N. R. *Adv. Mater.* **2011**, *23*, 5419-5424.
- (40) Ma, L.; Wang, J.; Ding, F. *Chem. Phys. Chem.* **2013**, *14*, 47-54.
- (41) Tarascon, J.-M.; Armand, M. *Nature* **2001**, *414*, 359-367.
- (42) Armand, M.; Tarascon, J.-M. *Nature* **2008**, *451*, 652-657.
- (43) Bruce, P. G.; Scrosati, B. Tarascon, J.-M. *Angew. Chem. Int. Ed.* **2008**, *47*, 2930-2946.
- (44) Yoshikawa, H.; Kazama, C.; Awaga, K.; Satoh, M.; Wada, J. *Chem. Commun.* **2007**, 3169-3170.

- (45) Yoshikawa, H.; Hamanaka, Y.; Miyoshi, Y. Kondo, Y.; Shigematsu, S.; Akutagawa, N.; Sato, M.; Yokoyama, T.; Awaga, K. *Inorg. Chem.* **2009**, *48*, 9057-9059
- (46) Kawasaki, N.; Wang, H.; Nakanishi, R.; Hamanaka, S.; Kitaura, R.; Shinohara, H.; Yokoyama, T.; Yoshikawa, H.; Awaga, K. *Angew. Chem., Int. Ed.* **2011**, *123*, 3533-3536.
- (47) Wang, H.; Hamanaka, S.; Yokoyama, T.; Yoshikawa, H.; Awaga, K. *Chem. Asian J.* **2011**, *6*, 1074-1079.
- (48) Wang, H.; Hamanaka, S.; Nishimoto, Y.; Irle, S.; Yokoyama, T.; Yoshikawa, H.; Awaga, K. *J. Am. Chem. Soc.* **2012**, *134*, 4918-4924.

Chapter 2

Theoretical Backgrounds

In this chapter, basic theoretical backgrounds to describe the electronic and molecular structures and properties are introduced so as to enlighten the subsequent chapters. Good materials are referred as refs. 1 to 6.

2.1 Many-Electron Problems to Hartree-Fock Approximation

As described in Chapter 1, classical force field methods have pitfalls because of poor description of electrons. Beyond classical force field methods, we need quantum mechanics (QM) methods,^{1,3,4,6} which complicates many electron problems. As for QM, one of the most important and well-known equation is the Schrödinger equation,

$$\mathcal{H}\Psi = \mathcal{E}\Psi. \quad (2.1)$$

where \mathcal{H} is the Hamiltonian operator for a system consisting of nuclei and electrons. Although the equation looks very simple, no one has yet found the general analytical solution of this equation, therefore the history of QM has been the history of finding good approximate solutions of it from the birth of QM. It should also be noted that this equation is restricted for non-relativistic and time-independent. The Hamiltonian operator \mathcal{H} can simply and analytically be written as

$$\mathcal{H} = -\frac{1}{2}\sum_{i=1}^N \nabla_i^2 - \frac{1}{2}\sum_{A=1}^M \frac{1}{M_A} \nabla_A^2 - \sum_{i=1}^N \sum_{A=1}^M \frac{Z_A}{r_{iA}} + \sum_{i=1}^N \sum_{j>i}^N \frac{1}{r_{ij}} + \sum_{A=1}^M \sum_{B>A}^M \frac{Z_A Z_B}{R_{AB}}, \quad (2.2)$$

where N and M represent numbers of electrons and nuclei, M_A is the ratio of the mass of nucleus A to the mass of an electron, and Z_A is the atomic number of nucleus A , and r_{iA} , r_{ij} , and R_{AB} represent the distance between the i th electron and A th nucleus, the i th and j th electrons, and A th and B th nucleus respectively. The Laplacian operator involves differentiation with respect to the coordinates of either electron or nucleus, giving the kinetic energy of particles. Although this Hamiltonian exactly depicts the behavior of non-relativistic time-independent particles, one cannot again solve the Schrödinger equation with the exact Hamiltonian analytically, therefore an approximation, called Born-Oppenheimer approximation, is introduced. The approximation neglects the movement of nuclei accompanying the movement of electrons. It is justified by the fact that nuclei are much heavier than electrons, and therefore they move more slowly. The remaining Hamiltonian operator, called electronic Hamiltonian, becomes

$$\mathcal{H}_{\text{electron}} \approx -\frac{1}{2} \sum_{i=1}^N \nabla_i^2 - \sum_{i=1}^N \sum_{A=1}^M \frac{Z_A}{r_{iA}} + \sum_{i=1}^N \sum_{j>i}^N \frac{1}{r_{ij}}. \quad (2.3)$$

This expression simplifies eq. (2.1) as if it is free from the motions of nuclei. Since we assume that nuclei are fixed, we can treat the contribution of nuclear potential to electrons, nuclear-nuclear repulsion, and total energy as if it is a parameter.

It must be mentioned that we additionally have to consider spin of electrons so that our electronic Hamiltonian is applicable for chemical problems. However, our Hamiltonian does not have any information of spin from its appearance, and thus simple addition of spin coordinate ω does not improve the description. Considering the basic principle of QM, as electrons being fermion with 1/2 spin, the wave function of electrons have to obey what we call Pauli exclusion principle. This states that “two identical fermions cannot occupy the same quantum state simultaneously”, and it requires our wave function to be antisymmetrized,

$$\Psi(\mathbf{x}_1, \dots, \mathbf{x}_i, \dots, \mathbf{x}_j, \dots, \mathbf{x}_N) = -\Psi(\mathbf{x}_1, \dots, \mathbf{x}_j, \dots, \mathbf{x}_i, \dots, \mathbf{x}_N), \quad (2.4)$$

where \mathbf{x} collectively represents three spatial coordinates \mathbf{r} and one spin coordinate ω . Exact wave function has to satisfy both the Schrödinger equation and the antisymmetry principle. Before thinking about the antisymmetry principle, it will be convenient to define Hartree product, as a many-electron wave function,

$$\Psi^{\text{HP}}(\mathbf{x}_1, \mathbf{x}_2, \dots, \mathbf{x}_N) = \chi_i(\mathbf{x}_1) \chi_j(\mathbf{x}_2) \cdots \chi_k(\mathbf{x}_N), \quad (2.5)$$

where χ_i represents the i -th spin orbital, product of spatial orbital ψ_i and spin function, either α or β . The physical description of Hartree product come from the fact that Hartree-Fock (HF) approximation assumes that electrons are uncorrelated (or independent). However, Hartree product does not satisfy the antisymmetry principle. It is easily satisfied by introducing the concept of Slater determinant, which can be written as following in a general form,

$$\begin{aligned} \Psi(\mathbf{x}_1, \mathbf{x}_2, \dots, \mathbf{x}_N) &= \frac{1}{\sqrt{N!}} \begin{vmatrix} \chi_i(\mathbf{x}_1) & \chi_j(\mathbf{x}_1) & \cdots & \chi_k(\mathbf{x}_1) \\ \chi_i(\mathbf{x}_2) & \chi_j(\mathbf{x}_2) & \cdots & \chi_k(\mathbf{x}_2) \\ \vdots & \vdots & & \vdots \\ \chi_i(\mathbf{x}_N) & \chi_j(\mathbf{x}_N) & \cdots & \chi_k(\mathbf{x}_N) \end{vmatrix} \\ &= |\chi_i(\mathbf{x}_1) \chi_j(\mathbf{x}_1) \cdots \chi_k(\mathbf{x}_N)\rangle. \end{aligned} \quad (2.6)$$

Interestingly, Slater determinant simultaneously satisfies the antisymmetry principle and another important property QM: indistinguishability of electrons, which is not taken into account with the simple Hartree product (eq. (2.5)) which inherently assigns the occupation of the spin orbital χ_i with the electron 1 (\mathbf{x}_1), etc.

Now, the most difficult part is how to evaluate the last term which stands for electron-electron interactions, raising an N -body problem. As an approximate approach for solving such a problem, the Hartree-Fock approximation is introduced as a primitive way. Although this approximation is hardly used for practical applications nowadays, its solution is still widely used as a starting point of electron correlation problems. To tackle with the N -body problem, the variational principle which states that the best wave function gives the lowest expectation value (energy) is a very powerful tool. Mathematically speaking, the lowest expectation value E_0 achieved only when the orthonormalized wave function $|\Psi\rangle$ becomes exact,

$$E_0 \leq \langle \Psi | \mathcal{H} | \Psi \rangle, (2.7)$$

where the equal sign holds only when the orthonormalized wave function is exact: $|\Psi\rangle = |\Psi_0\rangle$. The constraint of wave function normalization requires to introduce the Lagrangian's method of undetermined multiplier, however in practice, this eigenvalue problem directly derived in this line is not suited for being solved, therefore it is benefit to introduce "basis functions" and to write spatial orbitals by the linear combination of basis functions (atomic orbitals; LCAO) ϕ_i : $\psi_i = \sum_{\mu} c_{\mu i} \phi_{\mu}$. With the modified spatial orbital expression, we arrive an expression of Lagrangian's method,

$$\mathcal{L} = E - \sum_{ij} \varepsilon_{ij} \left(\sum_{\mu\nu} c_{\mu i} c_{\nu j} S_{\mu\nu} - 1 \right), (2.8)$$

where ε_{ij} is the undetermined Lagrange multiplier and $S_{\mu\nu} = \langle \phi_{\mu} | \phi_{\nu} \rangle$, corresponding to the overlap between atomic orbitals ϕ_{μ} and ϕ_{ν} . \mathcal{L} has to be minimized with respect to molecular orbital (MO) coefficient ($c_{\mu i}$), and as a result, we obtain a set of (pseudo-)eigenvalue problem,

$$\sum_{\nu} c_{\nu i} F_{\mu\nu} = \varepsilon_i \sum_{\nu} c_{\nu i} S_{\mu\nu}, (2.9)$$

where $F_{\mu\nu} = \langle \phi_{\mu} | f | \phi_{\nu} \rangle$, and

$$f(i) = -\frac{1}{2} \nabla_i^2 - \sum_{A=1}^M \frac{Z_A}{r_{iA}} + v^{\text{HF}}(i), (2.10)$$

where $v^{\text{HF}}(i)$ represents a sort of averaged potential experienced by the i -th electron in the presence of the other $N-1$ electrons. The essence of the Hartree-Fock approximation is to replace the complicated and sometimes complex many-electron problem by a one-electron problem in which electron-electron repulsion is treated in an average way.¹ Since Hartree-Fock potential (eq. (2.10)) depends on the electronic structure of the system through $v^{\text{HF}}(i)$, the solution of the Hartree-Fock equation cannot be obtained by a simple

(non-iterative) eigenvalue problem. The procedure in obtaining a set of solution is called self-consistent field (SCF) procedure, and it is continued until certain threshold is satisfied. The criteria differ by programs, but usually the difference of density matrix and/or energy of consecutive SCF cycles are compared with pre-defined thresholds.

2.2 Density Functional Theory

Hartree-Fock approximation has been historically important, however it is critical that the correlation between electrons (in other words, concerted movement of electrons) is completely neglected by definition. In order to take electron correlation into account, many MO based methods have been proposed such as configuration interaction (CI),¹ Møller-Plesset perturbation,⁷⁻¹⁰ coupled cluster^{1,11} theories. Apart from these methods, density functional theory (DFT)^{2,5,12,13} has been developed from 1960's. The root of DFT can be originated from Thomas-Fermi electron gas model,^{14,15} where they expressed the kinetic energy of electrons as a functional form of electron density,

$$T_{\text{TF}}[\rho(\mathbf{r})] = \frac{3}{10} (3\pi^2)^{2/3} \int \rho^{5/3}(\mathbf{r}) d\mathbf{r} . (2.11)$$

If we use a classical expression of electron-nuclear and electron-electron interaction, we can write the electronic energy of a system as a functional of electron density,

$$\begin{aligned} E_{\text{TF}}[\rho(r)] = & \frac{3}{10} (3\pi^2)^{2/3} \int \rho^{5/3}(\mathbf{r}) d\mathbf{r} - Z \int \frac{\rho(\mathbf{r})}{r} d\mathbf{r} \\ & + \frac{1}{2} \iint \frac{\rho(\mathbf{r}_1)\rho(\mathbf{r}_2)}{r_{12}} d\mathbf{r}_1 d\mathbf{r}_2 . (2.12) \end{aligned}$$

The novelty of the modified energy expression looks nothing, however their work showed that the electronic energy is completely given only with electron density $\rho(\mathbf{r})$, and therefore this is the very first DFT calculation.

DFT we call nowadays was greatly developed by Hohenberg and Kohn in 1964 by their two theorems.¹² Quoting the their original first theorem with modified notations for consistency, the first Hohenberg-Kohn theorem states that

$v(\mathbf{r})$ is (to within a constant) a unique functional of $\rho(\mathbf{r})$; since, in turn $v(\mathbf{r})$ fixes \mathcal{H} we see that the full many particle ground state is a unique functional of $\rho(\mathbf{r})$

where $v(\mathbf{r})$ is an external potential. The theorem states that a given ground state density, ρ_0 , uniquely defines an external potential, and the ground state energy E_0 is uniquely defined as

$$E_0[\rho_0(\mathbf{r})] = \int \rho_0(\mathbf{r}) V_{\text{Ne}} d\mathbf{r} + T[\rho_0(\mathbf{r})] + E_{\text{ee}}[\rho_0(\mathbf{r})]. \quad (2.13)$$

The first term, which represents nuclear-electron interaction energy, depends on the coordinates of nuclei, on the other hand remaining two terms, kinetic and electron-electron interaction energies, are a kind of universal functional in the sense that these interactions do not depend on system, i.e. positions of nuclei. It should be noted that we can partially explicitly write the $E_{\text{ee}}[\rho(\mathbf{r})]$ term,

$$E_{\text{ee}}[\rho(\mathbf{r})] = E_{\text{ncl}}[\rho(\mathbf{r})] + \frac{1}{2} \iint \frac{\rho(\mathbf{r}_1)\rho(\mathbf{r}_2)}{r_{12}} d\mathbf{r}_1 d\mathbf{r}_2, \quad (2.14)$$

where the first term represents the non-classical electron-electron interactions, and the second term is classically defined, Coulomb interaction.

Hohenberg and Kohn proved another important theorem (second Hohenberg-Kohn theorem), stating that the lowest energy is achieved only when the input density is the ground state density. This theorem is tightly connected to the well-known variational principle. Applicability of DFT to chemical problems has been shown with two Hohenberg-Kohn theorems without any approximations, however the form of equation is not very well suited for computational approach.

In 1965, Kohn and Sham suggested a practical procedure for computer algorithms using orbital-based approach, and fundamental applications for computational chemistry were established.¹³ They proposed to start with the approximation to use non-interacting system as a reference and to use Kohn-Sham orbitals in a self-consistent interactions procedure. This approximation introduces the concept that the movement of an electron does not depend on that of other electrons, therefore in a sense this treatment is close to the Hartree-Fock approximation. The true kinetic energy $T[\rho(\mathbf{r})]$ is divided into two terms without any approximations: kinetic energies of non-interacting system $T_s[\rho(\mathbf{r})]$ and the residual contribution $T_c[\rho(\mathbf{r})]$. No one yet found the exact expression of the residual contribution again, nevertheless, this is an important and useful approximation, because the non-interacting kinetic energy $T_s[\rho(\mathbf{r})]$ is simply written with the interacting density as

$$T_s[\rho(\mathbf{r})] = -\frac{1}{2} \sum_i^N \langle \psi_i | \nabla_i^2 | \psi_i \rangle. \quad (2.15)$$

Finally, the total energy functional of non-interacting system is written with only one unknown term in orbital-based formulation,

$$E[\rho(\mathbf{r})] = T_s[\rho(\mathbf{r})] + \frac{1}{2} \iint \frac{\rho(\mathbf{r}_1)\rho(\mathbf{r}_2)}{r_{12}} d\mathbf{r}_1 d\mathbf{r}_2 + \int \rho(\mathbf{r}) V_{\text{Ne}} d\mathbf{r} + E_{\text{xc}}[\rho(\mathbf{r})], \quad (2.16)$$

where $E_{xc}[\rho(\mathbf{r})]$ is called exchange-correlation energy, which includes the difference between interacting and non-interacting kinetic energies $T_c[\rho(\mathbf{r})]$, and non-classical electron-electron interaction terms $E_{ncl}[\rho(\mathbf{r})]$. Unfortunately, the exact form of exchange-correlation energy has not been uncovered, and the exchange-correlation term contains everything which are unknown, so it is like “a kind of junkyard where everything is stowed away which we do not know how to handle exactly.”⁵ Even in such a situation, many approximate exchange-correlation functionals have been proposed, and among them BP86^{16,17} and B3LYP^{18,19} functionals are briefly reviewed.

The BP86 is one of generalized gradient approximation (GGA) functionals and uses the representation by Becke in 1988 for non-local exchange contribution¹⁶ and by Perdew in 1986 for correlation contribution.¹⁷ The exchange contribution of GGA is usually written as

$$E_X^{GGA} = E_X^{LDA} - \sum_{\sigma} \int F(s_{\sigma}) \rho_{\sigma}^{\frac{4}{3}}(\mathbf{r}) d\mathbf{r}, \quad (2.17)$$

where E_X^{LDA} is the exchange contribution derived from the formula of local density approximation (LDA) proposed sometimes referred Dirac-Slater functional,^{20,21} and s_{σ} is

$$s_{\sigma} = \frac{|\nabla \rho_{\sigma}(\mathbf{r})|}{\rho_{\sigma}^{4/3}(\mathbf{r})}. \quad (2.18)$$

The representation by Becke in 1988¹⁶ is

$$F(s_{\sigma}) = \frac{\beta s_{\sigma}^2}{1 + 6\beta s_{\sigma} \sinh^{-1} s_{\sigma}}, \quad (2.19)$$

where $\beta = 0.0042$ is an empirical parameter, determined by least square fits. LDA functional only depends on the electron density around \mathbf{r} , however this apparently fails to cover detailed description of electrons where electron density fluctuates steeply. GGA improves the description by taking account the reduced density gradient (eq. (2.19)).

The representation for correlation contribution by Perdew in 1986¹⁷ is much more complicated formalism

$$E_C = \int n \epsilon_C(n_{\uparrow}, n_{\downarrow}) d\mathbf{r} + \int \frac{d^{-1} e^{-\Phi} C(n) |\nabla n|^2}{n^{4/3}} d\mathbf{r}, \quad (2.20)$$

where n indicates the sum of the density of alpha and beta electrons, n_{\uparrow} and n_{\downarrow} , respectively, and $\epsilon_C(n_{\uparrow}, n_{\downarrow})$ is the correlation energy per particle of the uniform electron gas.²²

The B3LYP is a little bit different from the BP86 functional in that it uses exact Hartree-Fock exchange for exchange contribution. Such a functional is called hybrid functional. The B3LYP formula¹⁹ is

$$E_{XC}^{B3LYP} = (1 - a_0)E_X^{LSD} + a_0E_X^{HF} + a_X\Delta E_X^{B88} + E_C^{LYP} + (1 - a_C)\Delta E_C^{VWN}, \quad (2.21)$$

where a_0 , a_X and a_C are the semi-empirical coefficients determined by an appropriate fit to experimental data, E_X^{HF} is the exact exchange contribution based on Hartree-Fock theory, ΔE_X^{B88} is the non-local exchange contribution represented by Becke (Eq. (24)~(26)), and E_C^{LYP} and ΔE_C^{VWN} are the local and non-local correlation contribution represented by Lee, Yang and Parr in 1988¹⁸ and by Vosko, Wilk and Nusair in 1980.²² Since the functional uses three semi-empirical coefficients, it is referred as “B3LYP”. The performance of B3LYP functional is usually better than BP86 functional,⁵ however due to the requirement of exact Hartree-Fock exchange evaluation, the computational cost is more expensive than pure-GGA functionals, such as BP86 mentioned above.

It should be mentioned that there is no assurance that orbitals obtained by DFT is true MOs, because there is no proof that the ground state density is uniquely defined by only one wave function.⁵ These orbitals are often distinguished by calling Kohn-Sham orbitals, nevertheless Kohn-Sham orbitals are known to describe MOs qualitatively and are used as if they are MOs (sometimes equivalently).

In the end of theoretical background of DFT, one approximate method is being reviewed. One of the most time consuming steps in DFT calculation is the evaluation of Coulomb interaction, the second term of eq (2.16). Because the term depends on four MO indices, the scaling of its computational cost grows as quartic ($O(L^4)$) with respect to the number of basis functions L , which can be more expensive than solving (pseudo-)eigenvalue problems whose cost scales as cubic formally. The RI approximation²³ is the technique to expand spatial electron density, $\rho(\mathbf{r})$, by atom centered auxiliary basis sets, denoted α (and β),

$$\rho(\mathbf{r}) \approx \sum_{\alpha} c_{\alpha} \alpha(\mathbf{r}) = \tilde{\rho}(\mathbf{r}). \quad (2.17)$$

The coefficient c_{α} of atom centered auxiliary basis set after expansion of spatial electron density is determined to minimize the difference between expanded and real density. This manipulation is mathematically equivalent to the replacement

$$(ij|kl) \approx \sum_{\alpha\beta} (ij|\alpha)(\alpha|\beta)^{-1}(\beta|kl). \quad (2.18)$$

This approximation formally resembles the resolution of the identity in Hilbert space theory for nonorthogonal basis functions: hence using the acronym, we call this method

RI approximation.²⁴ The Coulomb energy after expansion the electron density using auxiliary basis sets is expressed as

$$J \approx \tilde{J} = \frac{1}{2}(\rho | \tilde{\rho}) \approx \frac{1}{2}(\tilde{\rho} | \tilde{\rho}) = \frac{1}{2} \sum_{\alpha} \sum_{\beta} c_{\alpha} c_{\beta} (\alpha | \beta) \quad (2.19)$$

and matrix elements of the Coulomb operator are

$$J_{ij} \approx \tilde{J}_{ij} = \sum_{\alpha} c_{\alpha} (ij | \alpha) \quad . \quad (2.20)$$

As the four-center integral is approximately expressed by the products of two- and three-center integrals, the approximation reduces the computational cost for evaluating Coulomb integrals from $O(L^4)$ to $O(L^2K)$, where K is the number of auxiliary basis functions.⁵ The RI approximation is sometimes referred as “density fitting”, and it is recently extended to exchange integrals for hybrid functionals in a similar way.^{25,26}

2.3 Density-Functional Tight-Binding Method

Although there have been many techniques to achieve efficient and/or linear scaling MO-based and DFT methods, their computational cost remains marginally expensive. For instance, famous linear scaling method is referred as the fragment molecular orbital (FMO)²⁷⁻³¹ and divide-and-conquer³²⁻³⁴ methods. The details of the first method will be reviewed briefly in the following section. The expensive computational cost is mainly because (1) large dimension of (pseudo-)eigenvalues problem and (2) a large number of integral calculations, have to be considered. The first problem should be related to the fact that functions of higher angular momentum must be included in variational space to obtain accurate result. The dependence of accuracy upon basis set size becomes more critical for MO-based method.⁶ The second problem can partly be solved by introducing the RI approximation, nevertheless a large number of integrals has to be still considered, and unfortunately calculations of integral are not very cheap.

One can of course use molecular mechanics (MM) methods using force field model, however as mentioned in the previous chapter, the QM description is no longer taken account. As an alternative approach, efficient calculation, leaving QM description remain, can be attained by semi-empirical methods such as AM1,³⁵ PM6,^{36,37} and the density-functional tight-binding (DFTB) method³⁸⁻⁴³ which introduces tight-binding approach over DFT. As a difference between these methods, while AM1 and PM6 use atom-dependent parameters, DFTB uses atom-pair-dependent parameters. This is the

central reason that DFTB attains better accuracy compared to other semi-empirical methods. As a matter of fact, DFTB is comparable to a low-level DFT calculation.⁴⁴⁻⁴⁶

Since DFTB method is of great importance in latter Chapters, it is in detail explained dividing into several subsections. The first subsection briefly reviews the central concept of DFTB method, and the second develops to self-consistent-charge (SCC) model. As the third subsection, some extensions of DFTB are to be presented.

2.3.1 Tight-Binding Theory and Nonself-Consistent-Charge (NCC) DFTB

The central concept of DFTB method is, obvious from its name, the tight-binding theory. It is originated from Bloch's work in 1928⁴⁷ and Slater and Koster's work in 1954,⁴⁸ and can be simply stated that "electrons are tightly bound to atom" and cannot move (freely) between atoms. Therefore it is pretty reasonable that the space where electrons can move around an atom is expanded with the atom-centered localized orbitals, like LCAO, as already introduced in Hartree-Fock method.

In the derivation of DFTB method, the starting point is the electronic energy of DFT (eq. (2.16)), and additionally electron density is expanded by a small fluctuation $\delta\rho(\mathbf{r})$ of density from reference density $\rho_0(\mathbf{r})$, that is

$$\rho(\mathbf{r}) = \rho_0(\mathbf{r}) + \delta\rho(\mathbf{r}). \quad (2.21)$$

With this approximation for DFTB, electronic energy is in generally transformed as

$$\begin{aligned} E[\rho(\mathbf{r})] = & E[\rho_0(\mathbf{r})] + \frac{1}{2} \iint \frac{\delta^2 E}{\delta\rho(\mathbf{r}_1)\delta\rho(\mathbf{r}_2)}|_{\rho_0(\mathbf{r})} \delta\rho(\mathbf{r}_1)\delta\rho(\mathbf{r}_2) d\mathbf{r}_1 d\mathbf{r}_2 \\ & + \mathcal{O}(\delta\rho(\mathbf{r})^2). \end{aligned} \quad (2.22)$$

Applying it for the total energy (electronic energy + nuclear repulsion energy) of DFT,

$$\begin{aligned} E[\rho(\mathbf{r})] = & \sum_i^{\text{occ}} \langle \psi_i | \mathcal{H}_0 | \psi_i \rangle - \frac{1}{2} \iint \frac{\rho_0(\mathbf{r}_1)\rho_0(\mathbf{r}_2)}{r_{12}} d\mathbf{r}_1 d\mathbf{r}_2 + E_{\text{XC}}[\rho_0(\mathbf{r})] \\ & - \int \rho_0(\mathbf{r}) V_{\text{XC}}[\rho_0(\mathbf{r})] d\rho(\mathbf{r}) + E_{\text{nuc}} + \mathcal{O}(\delta\rho(\mathbf{r})^2), \end{aligned} \quad (2.23)$$

where \mathcal{H}_0 represents the Hamiltonian which is generated with the reference density as input, and E_{nuc} is the nuclear repulsion term. The terms linear in $\delta\rho(\mathbf{r})$ cancel each other at any arbitrary input density. In NCC-DFTB,³⁸ first five terms of eq. (2.23) are considered, and the second-order fluctuation terms are neglected, leading to a simple equation,

$$E^{\text{NCC}} = \sum_i^{\text{occ}} \langle \psi_i | \mathcal{H}_0 | \psi_i \rangle + E_{\text{rep}}. \quad (2.24)$$

The second, third, and fourth terms of eq. (2.23) now only depends the reference density, we can therefore put these energies into a term E_{rep} which is independent from the electronic structure (or fluctuation of electron density). Applying the variational principle to Eq. (2.24), we obtain an eigenvalue problem,

$$\sum_v^{\text{AO}} c_{vi} (H_{\mu\nu}^0 - \varepsilon_i S_{\mu\nu}) = 0, \quad (2.25)$$

where $H_{\mu\nu}^0 = \langle \phi_\mu | \mathcal{H}_0 | \phi_\nu \rangle$ and $S_{\mu\nu} = \langle \phi_\mu | \phi_\nu \rangle$ called Hamiltonian and overlap matrix elements. Although these matrix elements at a glance require an integral calculation, it is not the case for DFTB, because these integral terms are pre-computed for each atomic pair and tabulated in a file discretely. During production calculations, the interpolation of tabulated values returns these integral values immediately. The Hamiltonian matrix element $H_{\mu\nu}^0$ is defined as

$$H_{\mu\nu}^0 = \begin{cases} \varepsilon_\mu^{\text{neutral free atom}} & \text{if } \mu = \nu \\ \langle \phi_\mu^A | \hat{T} + V_0^A + V_0^B | \phi_\nu^B \rangle & \text{if } A \neq B \\ 0 & \text{otherwise} \end{cases}, \quad (2.26)$$

where A and B are the indices of atoms. Since the Hamiltonian matrix element does not depend on the electronic structure (i.e., electron density or density matrix), NCC-DFTB is a simple eigenvalue problem, thus iterative SCF procedure is not needed.

2.3.2 Self-Consistent-Charge (SCC) DFTB

NCC-DFTB is a good approximation for homogeneous systems with little charge polarization and has been successfully applied for some systems.^{38,39} However, it is unfortunately not a good approximation when it comes to the application for charged systems such as proteins and DNAs. The most sensible and effective extension is to include the truncated second-order charge fluctuation term,

$$E_{2\text{nd}} = \frac{1}{2} \iint \frac{\delta\rho(\mathbf{r}_1)\delta\rho(\mathbf{r}_2)}{r_{12}} d\mathbf{r}_1 d\mathbf{r}_2 + \frac{1}{2} \iint \frac{\delta^2 E_{\text{XC}}}{\delta\rho(\mathbf{r}_1)\delta\rho(\mathbf{r}_2)}|_{\rho_0(\mathbf{r})} \delta\rho(\mathbf{r}_1)\delta\rho(\mathbf{r}_2) d\mathbf{r}_1 d\mathbf{r}_2 \quad (2.27)$$

After some transformations applying approximations, the $E_{2\text{nd}}$ term is written simply as

$$E_{2\text{nd}} \approx \frac{1}{2} \sum_{A,B}^M \gamma_{AB} \Delta q_A \Delta q_B, \quad (2.28)$$

where γ_{AB} depends on the distance between atom A and B and their chemical hardness, and Δq_A is the deviation of the Mulliken population on atom A from that in the neutral atom q_A^0 that is $\Delta q_A = q_A - q_A^0$, where

$$q_A = \frac{1}{2} \sum_i n_i \sum_{\mu \in A} \sum_v (c_{\mu i} c_{v i} S_{\mu v} + c_{v i} c_{\mu i} S_{v \mu}), \quad (2.29)$$

where n_i is the number of electrons that occupy i -th MO. We now can define the total energy of SCC-DFTB³⁹ as

$$E^{\text{SCC}} = \sum_i^{\text{occ}} \langle \psi_i | \mathcal{H}_0 | \psi_i \rangle + \frac{1}{2} \sum_{A,B}^M \gamma_{AB} \Delta q_A \Delta q_B + E_{\text{rep}}. \quad (2.30)$$

Applying the variational principle to eq. (2.30) again, we obtain an eigenvalue problem, however now Hamiltonian matrix element is

$$H_{\mu\nu} = H_{\mu\nu}^0 + \frac{1}{2} S_{\mu\nu} \sum_C^M (\gamma_{AC} + \gamma_{BC}) \Delta q_C. \quad (2.31)$$

The second term of eq. (2.31) depends on Δq_C , which depends on MO coefficients we can obtain as a solution of an eigenvalue problem. Since $H_{\mu\nu}$ cannot be determined uniquely, SCC-DFTB requires to perform iterative SCF cycles. For this reason, SCC-DFTB is usually 5 to 20 times more expensive, however the extension opened DFTB to wider range of applications.

Energy represents only the zeroth order property of electronic structure. It is certainly enough to discuss the energy difference, however in practical application, the analytical first- and second-order geometrical derivatives, usually called gradient and Hessian respectively, are important as well. Both derivatives can be evaluated numerically, however this needs at least $3M$ and $9M^2$ times energy evaluations without symmetry constraint, and it is certainly computationally demanding for large systems. Therefore the analytic derivatives are certainly very important items. Many details of both derivatives are discussed in Appendix A, so only final gradient F_a ³⁹ and Hessian G_{ab} ⁴⁹ of SCC-DFTB are presented here,

$$F_a = \sum_i^{\text{MO}} n_i \sum_{\mu\nu}^{\text{AO}} c_{\mu i} c_{v i} \left\{ \frac{\partial H_{\mu\nu}^0}{\partial a} + (\Omega_{AB} - \varepsilon_i) \frac{\partial S_{\mu\nu}}{\partial a} \right\} + \sum_{CD}^M \frac{\partial \gamma_{CD}}{\partial a} \Delta q_C \Delta q_D + \frac{\partial E^{\text{rep}}}{\partial a} \quad (2.32)$$

and

$$\begin{aligned}
G_{ab} = & \sum_i^{\text{MO}} n_i \sum_{\mu\nu}^{\text{AO}} c_{\mu i} c_{\nu i} \left\{ \frac{\partial^2 H_{\mu\nu}^0}{\partial a \partial b} + (\Omega_{AB} - \varepsilon_i) \frac{\partial^2 S_{\mu\nu}}{\partial a \partial b} + \left(\frac{\partial \Omega_{AB}}{\partial b} - \frac{\partial \varepsilon_i}{\partial b} \right) \frac{\partial S_{\mu\nu}}{\partial a} \right\} \\
& + \sum_i^{\text{MO}} n_i \sum_{\mu\nu}^{\text{AO}} \sum_m^{\text{MO}} U_{mi}^b c_{\mu i} c_{\nu i} \left\{ \frac{\partial H_{\mu\nu}^0}{\partial a} + (\Omega_{AB} - \varepsilon_i) \frac{\partial S_{\mu\nu}}{\partial a} \right\} \\
& + \sum_{CD}^M \left(\Delta q_C \Delta q_D \frac{\partial^2 \gamma_{CD}}{\partial a \partial b} + \frac{\partial \gamma_{CD}}{\partial a} \frac{\partial q_D}{\partial b} \Delta q_D + \frac{\partial \gamma_{CD}}{\partial a} \Delta q_C \frac{\partial q_D}{\partial b} \right) \\
& + \frac{\partial^2 E^{\text{rep}}}{\partial a \partial b} \quad (2.33)
\end{aligned}$$

where

$$\Omega_{AB} = \frac{1}{2} S_{\mu\nu} \sum_C^M (\gamma_{AC} + \gamma_{BC}) \Delta q_C \quad (2.34)$$

and

$$\frac{\partial c_{\mu i}}{\partial a} = \sum_m^{\text{MO}} U_{mi}^a c_{\mu m} \quad (2.35)$$

2.3.3 Further Extensions of DFTB

As further extensions of DFTB method, (1) dispersion correction (DC), (2) unrestricted formalism, and (3) third-order DFTB are briefly overviewed in this subsection.

(1) Dispersion correction (DC)

It is well-known that DFT with LDA, GGA, and some of hybrid functionals cannot describe dispersion interactions, such as van der Waals or London forces. Since parameters for DFTB rely on DFT electronic and molecular structures, DFTB takes over this unfavorable character. In DFTB community, two flavors of DC are widely used, universal force-field (UFF)⁵⁰ and Slater-Kirkwood⁵¹ type DCs. Both DCs are independent from electronic structure. The UFF type DC for long-range interaction, where the distance between two atoms A and B is longer than a threshold ($r_{AB} > 2^{-1/6} R_{AB}$), has the form of

$$E_{AB}^{\text{disp}} = d_{AB} \left\{ -2 \left(\frac{R_{AB}}{r_{AB}} \right)^6 + \left(\frac{R_{AB}}{r_{AB}} \right)^{12} \right\} \quad (2.36)$$

where d_{AB} and R_{AB} are well depth and van der Waals distance respectively, whereas short-range interaction is

$$E_{AB}^{\text{disp}} = U_0 - U_1 r^n - U_2 r^{2n} \quad (2.37)$$

where $U_0 = \frac{395}{25} d_{AB}$, $U_1 = 2^{5/6} \frac{672}{25} \frac{d_{AB}}{r_{AB}^5}$, and $U_2 = -2^{2/3} \frac{552}{25} \frac{d_{AB}}{r_{AB}^{10}}$. Another flavor,

Slater-Kirkwood type DC⁵¹ is somewhat more complicated,

$$E_{AB}^{\text{disp}} = -f(r_{AB}) C_6^{AB} (r_{AB})^{-6}$$

where

$$f(r_{AB}) = \left(1 - \exp \left(-d \left(\frac{r_{AB}}{R_0^{AB}} \right)^n \right) \right)^m \quad (2.38)$$

and

$$R_0^{AB} = \frac{(R_0^A)^3 + (R_0^B)^3}{(R_0^A)^2 + (R_0^B)^2} \quad (2.39)$$

where R_0^A is the cutoff radius of atom A. The $C_6^{AB}(r_{AB})$ is defined as

$$C_6^{AB} = \frac{2C_6^A C_6^B p_A p_B}{p_A^2 C_6^B + p_B^2 C_6^A} \quad (2.40)$$

where $C_6^A = 0.75 \sqrt{N_A p_A^3}$, and N_A and p_A are the effective number of electrons and the static polarizability of atom A.

Not depending on electronic structure, DCs are conceptually classified into a classical interaction, therefore the implementation into a program is relatively easy and the computational requirement is fractional. DCs nevertheless improve stacking energy of DNA base pairs and give good agreement with more accurate MP2 calculations.⁵¹

(2) Unrestricted formalism

DFTB equations above assume restricted wave function, which uses same set of orbitals for both alpha and beta electrons (Figure 2.1A). Not all molecular and electronic structures can be well described by same set of orbitals in real. In contrast, unrestricted wave function uses different sets of orbitals for alpha and beta electrons (Figure 2.1B). The unrestricted formalism realizes to include spin-polarization effects either in a collinear or a non-collinear fashion as in the work by Köhler et al.⁵²⁻⁵⁴ In a collinear approach,^{52,53} the spin-spin interaction is described by first defining shell-resolved Mulliken spin density, $p_{Al} = q_{Al}^\alpha - q_{Al}^\beta$, where q_{Al}^α and q_{Al}^β are the shell-resolved Mulliken populations of alpha and beta electrons ($l \in A$), defined as Eq. (2.29) but μ runs over the AOs of shell l , not atom A. Within restricted wave function where a pair of alpha and beta electrons occupy single orbital, all spin density results in zero.

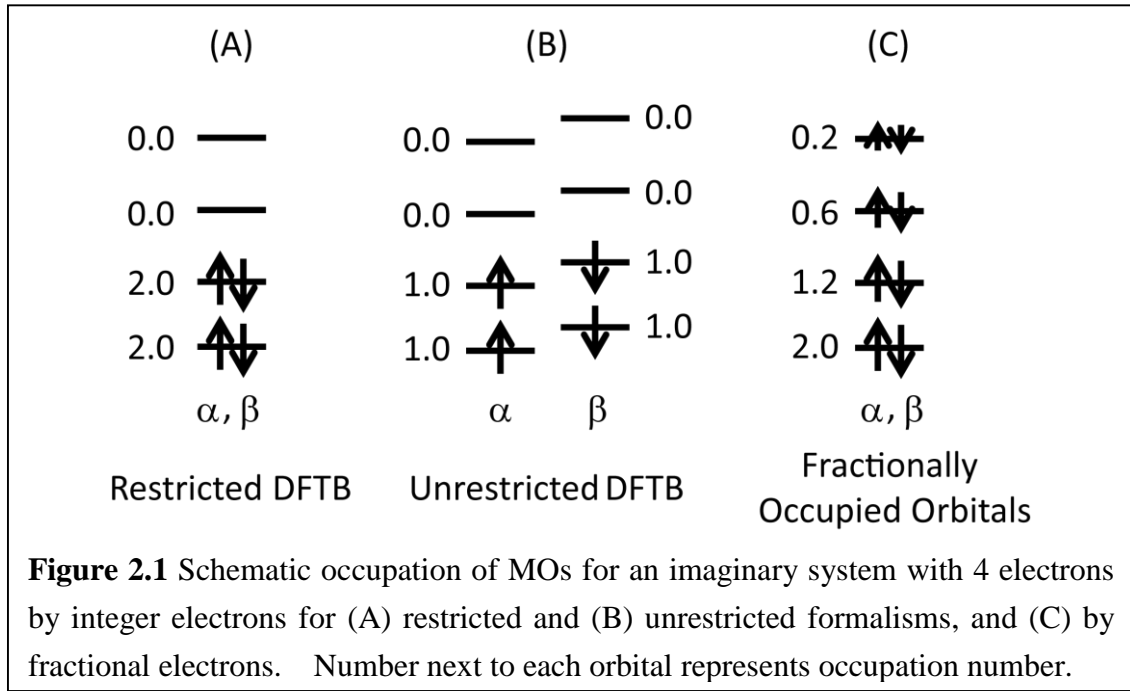
On the other hand, unrestricted wave function arises spin density, therefore spin-spin interaction, defined as

$$E_{\text{spin}} = \frac{1}{2} \sum_A \sum_{l \in A} \sum_{l' \in A} p_{Al} p_{Al'} W_{All'}, \quad (2.41)$$

where $W_{All'}$ is the atomic spin constant calculated as

$$W_{All'} = \frac{1}{2} \left(\frac{\partial \varepsilon_l^\alpha}{\partial n_{l'}^\alpha} - \frac{\partial \varepsilon_l^\alpha}{\partial n_{l'}^\beta} \right), \quad (2.42)$$

have to be included. The atomic spin constant values are calculated beforehand using DFT. It is known that DFTB has the capability of generating open-shell singlet wave function, where the sum of spin quantum number yields zero but at least one pair of alpha and beta electrons occupy different orbitals. Open-shell singlet state sometimes results in lower energy than triplet or restricted singlet state.



The Hamiltonian matrix element of unrestricted wave function needs one additional term which represents the spin-spin interaction,

$$H_{\mu\nu}^{\sigma} = H_{\mu\nu}^0 + \frac{1}{2}S_{\mu\nu} \sum_C^M (\gamma_{AC} + \gamma_{BC})\Delta q_C + \frac{1}{2}S_{\mu\nu}\delta_{\sigma} \left(\sum_{l'' \in A} W_{Al''} p_{Al''} + \sum_{l'' \in B} W_{Bl''} p_{Bl''} \right), \quad (2.43)$$

where $\delta_{\sigma} = \pm 1$ depending on the spin index $\sigma (= \alpha \text{ or } \beta)$. Since alpha and beta orbitals have to be treated separately, one has to solve the eigenvalue problem Eq. (2.25) twice per SCF iteration. For this reason, the computational cost of unrestricted wave function is estimated to be about twice, compared with the restricted case. Using a different set of orbitals for alpha and beta electrons causes the spin contamination problem, since alpha and beta eigenvectors are independently obtained by solving a different eigenvalue problem, and therefore alpha eigenvectors are not orthonormalized against beta and vice versa. The mismatch between alpha and beta orbitals gives a bigger expectation value of S^2 value than the expectation value without any spin contamination $\langle S^2 \rangle_{\text{Exact}}$, defined as¹

$$\langle S^2 \rangle = \langle S^2 \rangle_{\text{Exact}} + N^{\beta} - \sum_i^N \sum_j^N |\langle \psi_i^{\alpha} | \psi_j^{\beta} \rangle|^2. \quad (2.44)$$

Because of this spin contamination problem, unrestricted wave function is nothing but an approximate wave function. As a solution, restricted-open shell wave function has been proposed for *ab initio* calculations,⁵⁵ however there is no similar theory for DFTB.

(3) Third-order DFTB

A possible further extension of SCC-DFTB is to include the third-order charge fluctuation term,⁵⁶

$$E_{3\text{rd}} = \frac{1}{6} \iiint \frac{\delta^3 E_{\text{XC}}}{\delta \rho(\mathbf{r}_1) \delta \rho(\mathbf{r}_2) \delta \rho(\mathbf{r}_3)} |_{\rho_0(\mathbf{r})} \delta \rho(\mathbf{r}_1) \delta \rho(\mathbf{r}_2) \delta \rho(\mathbf{r}_3) d\mathbf{r}_1 d\mathbf{r}_2 d\mathbf{r}_3. \quad (2.45)$$

The simplification of the $E_{3\text{rd}}$ term results in

$$E_{3\text{rd}} \approx \frac{1}{3} \sum_{A,B}^M \Gamma_{AB} (\Delta q_A)^2 \Delta q_B \quad (2.46)$$

where Γ_{AB} is a newly introduced variable which depends on the distance between atom A and B , their chemical hardness, and the derivative of A 's chemical hardness. Physically, the chemical hardness of an atom has been constant with the second-order expansion (SCC-DFTB), however the third-order expansion allows different chemical

hardness value depending on charge state. This expansion improves the description of charged systems.⁵⁶

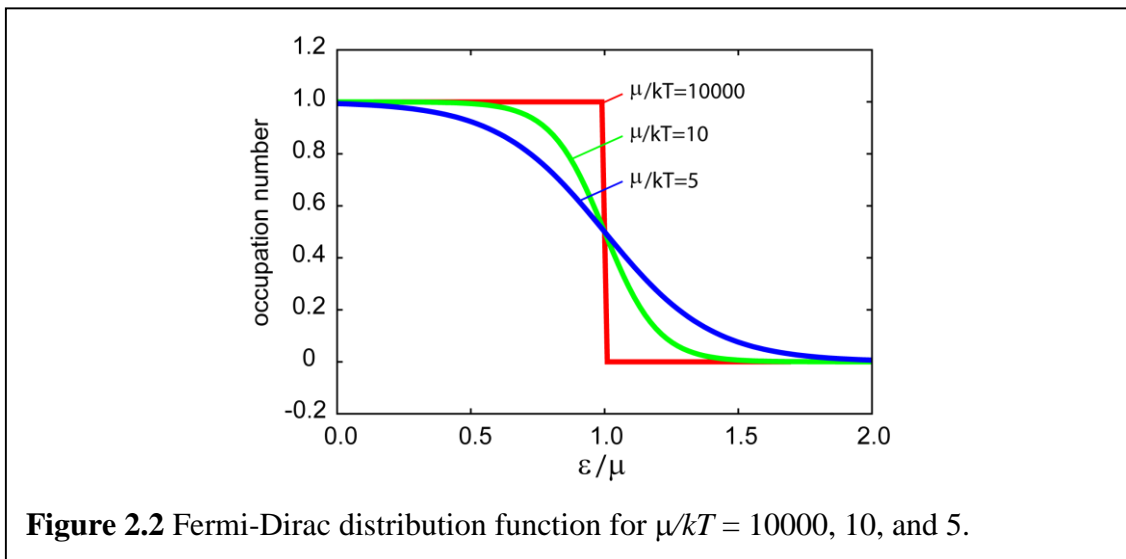
2.3.4 Electronic temperature

Our (pseudo-)eigenvalue problem sometimes cannot find a stable SCF solution. The instability most likely comes from the nearly-degenerated frontier orbitals. In such situation, integer occupation of orbitals creates so strong potential that the electronic structure determined previously is upset by the potential newly generated. A cheap solution applicable for DFTB is to utilize fractional occupation numbers for orbital occupation. The concept is to use a smooth function (Figure 2.) in determining occupation numbers of orbitals allowing fractionally occupied orbitals (Figure 2.1C), while the number of electrons in the system is kept constant. This prevents orbitals from inter-conversion during SCF calculation. As a smooth function, one of the functions that are widely used is the Fermi-Dirac distribution function.^{57,58} As a parameter of the function, electronic temperature T_e is defined, mimicking the degree of excitation of electrons.

Generally, in non-metallic system with a wide band gap, the electronic structure is well described as 0 K, and the orbital occupation numbers are represented as a step function switching from 1 to 0 at the Fermi energy, approximately shown by the red line in Figure 2.2. However, when T_e is set to a non-zero value, the occupation numbers in a system are no longer integer numbers, because the electrons are excited obeying the Fermi-Dirac distribution function,

$$f_i = \left(1 + \exp\left(\frac{\varepsilon_i - \varepsilon_F}{kT_e}\right) \right)^{-1} \quad (2.47)$$

where f_i is the fractional occupation number of the i -th molecular orbital, and ε_F is the chemical potential (or Fermi level), which is numerically determined so that the sum of all the functional number of electrons is equal to the total number of electrons N . This occupation smearing technique is especially useful, or sometimes necessary, for metal containing systems or insulators^{59,60} in which orbitals around Fermi level are degenerated.



2.4 Fragment Molecular Orbital (FMO) Approach

FMO method²⁷⁻³¹ is a method which aims at linear scaling. While traditional QM approaches treat whole system as it is, FMO method first fragments a large molecule into a sets of small fragments. Properties, i.e. energies,⁶¹ gradients,^{62,63} and so on, of the system are recovered by summing up those of fragments. For instance, the total energy of the whole system in the two-body FMO expansion⁶¹ is

$$E = \sum_I^L E_I + \sum_{I>J}^L (E_{IJ} - E_I - E_J), \quad (2.48)$$

where L is the number of fragments, and the E_X terms are the energies of fragments ($X = I$) and their pairs ($X = IJ$). Obvious from the equation that we need calculations of monomers and dimers that include one or two fragments. Although eq. (2.48) truncates higher order terms than two-body, the inclusions of three-⁶⁴ and four-body⁶⁵ terms are proposed and are known to improve the accuracy of approximation. Each fragment calculation has to be done under the presence of electrostatic potential (ESP) which mimics the environmental effects. It should be noted that the evaluation of ESP requires a number of integral calculations. Although the first problem of bottleneck which comes

from diagonalization of Fock matrix seems to be solved by fragmenting large molecule into fragments, the evaluation of ESP needs a number of integral calculations, because the number of environmental atoms remains same as the pristine molecule. Some approximations have already been proposed to decrease the integral calculations of ESP based on Mulliken AO or point charge (ESP-AOC and ESP-PTC).⁶⁶

Since the number of dimer calculations scales as quadratic ($L(L+1)/2$), the computational time also scales as quadratic. To achieve linear-scaling, the electrostatic dimer (ES-DIM) approximation⁶⁶ is usually used for far separated dimers, because there is almost negligible amount of charge transfer between such pairs. QM effect is taken account into consideration through charge transfer between two fragments, but if it is negligibly small, the energy of the dimer can easily be evaluated classically. The classical evaluation is far more economic than QM, and most dimers calculations are approximated in this way, therefore the computational cost of dimer eventually scales as linear.²⁸

For a system with covalent bonds, fragmentation is not very straightforward, because electrons and orbitals are usually delocalized between atoms and therefore we cannot define uniquely the assignment of numbers of electrons and orbitals per atom or spatially. In FMO framework, hybrid orbital projection (HOP)^{61,67,68} is used for fragmentation of covalent bonds. Suppose that there is a bond between two sp^3 atoms, which we call bond detached or bond attached atom (BDA or BAA). BDA presents in two fragments, so the orbitals of BDA have to be divided into two sets; the first set contains one hybrid orbital which is supposed to point BAA, and the second set contains other three hybrid orbitals on BDA. This procedure is accomplished with defining projection operators based on the pre-defined hybrid orbitals of BDAs. The projection operator for the X -th fragment is mathematically expressed as⁶¹

$$\hat{P}^X = \sum_{k \in X} B_k |\theta_k\rangle \langle \theta_k|$$

where $|\theta_k\rangle$ is a pre-defined hybrid orbital and the universal constant B_k is usually set to 10^6 . Later, adaptive frozen orbital (AFO) scheme was proposed and applied for solids and wire-like systems.^{69,70}

Bibliography

- (1) Szabo, A.; Ostlund, N. S. *Modern Quantum Chemistry: Introduction to Advanced Electronic Structure Theory*; Macmillan Publishing Co., Inc.: New York, 1982.

- (2) Parr, R. G.; Yang, W.; *Density-Functional Theory of Atoms and Molecules*; Oxford University Press, Inc.: New York, 1989.
- (3) Yamaguchi, Y.; Schaefer, H. F., III; Osamura, Y.; Goddard, J.; *A New Dimension to Quantum Chemistry: Analytical Derivative Methods in Ab Initio Molecular Electronic Structure Theory*; Oxford University Press: New York, 1994.
- (4) Helgaker, T.; Jørgensen, P.; Olsen, J.; *Molecular Electronic-Structure Theory*; Wiley: Chichester, 2000.
- (5) Koch, W.; Holthausen, M. C.; *A Chemist's Guide to Density Functional Theory*; WILEY-VCH Verlag GmbH: Weinheim, 2001.
- (6) Jensen, F.; *Introduction to Computational Chemistry*; John Wiley & Sons, Ltd.: England, 2007.
- (7) Head-Gordon, M.; Pople, J. A.; Frisch, M. J. *Chem. Phys. Lett.* **1988**, *153*, 503-506.
- (8) Frisch, M. J.; Head-Gordon, M.; Pople, J. A. *Chem. Phys. Lett.* **1990**, *166*, 275-280.
- (9) Frisch, M. J.; Head-Gordon, M.; Pople, J. A. *Chem. Phys. Lett.* **1990**, *166*, 281-289.
- (10) Head-Gordon, M.; Head-Gordon, T. *Chem. Phys. Lett.* **1994**, *220*, 122-128.
- (11) Barless, R. J.; Musiał, M. *Rev. Mod. Phys.* **2007**, *79*, 291-352.
- (12) Hohenberg, P.; Kohn, W. *Phys. Rev.* **1964**, *136*, B864-B871.
- (13) Kohn, W.; Sham, L. J. *Phys. Rev.* **1965**, *140*, A1133-A1138.
- (14) Thomas, L. H. *Proc. Cambridge Phil. Soc.* **1927**, *23*, 542-548.
- (15) Fermi, E. *Rend. Accad. Naz. Lincei* **1927**, *6*, 602-607.
- (16) Becke, A. D. *Phys. Rev. A* **1988**, *38*, 3098-3100. (61)
- (17) Perdew, J. P. *Phys. Rev. B* **1986**, *33*, 8822-8824. (63)
- (18) Lee, C.; Yang, W.; Parr, R. G. *Phys. Rev. B* **1988**, *37*, 785-789. (62)
- (19) Becke, A. D. *J. Chem. Phys.* **1993**, *98*, 5648-5652. (67)
- (20) Dirac, P. A. M. *Proc. Royal. Soc. (London) A* **1929**, *123*, 714-733. (57)
- (21) Slater, J. C. *Phys. Rev.* **1951**, *81*, 385-390. (58)
- (22) Vosko, S.; Wilk, L.; Nusair, M. *Can. J. Phys.* **1980**, *58*, 1200-1211. (59)
- (23) Eickorn, E.; Treutler, O.; Öhm, H.; Häser, M.; Ahlrichs, R. *Chem. Phys. Lett.* **1995**, *242*, 652-660.
- (24) Sierka, M.; Hogeckamp, A.; Ahlrichs, R. *J. Chem. Phys.* **2003**, *118*, 9136-9148.
- (25) Aquilante, F.; Pedersen, T. B.; Lindh, R. *J. Chem. Phys.* **2007**, *126*, 194106.
- (26) Boström, J.; Aquilante, F.; Pedersen, T. B.; Lindh, R. *J. Chem. Theory Comput.* **2013**, *9*, 204-212.
- (27) Kitaura, K.; Ikeo, E.; Asada, T.; Nakano, T.; Uebayasi, M. *Chem. Phys. Lett.* **1999**, *313*, 701-706.

- (28) *The Fragment Molecular Orbital Method: Practical Applications to Large Molecular Systems*; Fedorov, D. G., Kitaura, K., Eds.; CRC Press: Boca Raton, FL, 2009.
- (29) Fedorov, D. G.; Kitaura, K. *J. Phys. Chem. A* **2007**, *111*, 6904-6914.
- (30) Fedorov, D. G.; Nagata, T.; Kitaura, K. *Phys. Chem. Chem. Phys.* **2012**, *14*, 7562-7577.
- (31) Tanaka, S.; Mochizuki, Y.; Komeiji, Y.; Okiyama, Y.; Fukuzawa, K. *Phys. Chem. Chem. Phys.* **2014**, *16*, 10310-10344.
- (32) *Linear-Scaling Techniques in Computational Chemistry and Physics*; Zalesny, R., Papadopoulos, M. G., Mezey, P. G., Leszczynski, J., Eds.; Springer: New York, 2011.
- (33) Yang, W.; Lee, T.-S. *J. Chem. Phys.* **1995**, *103*, 5674-5678.
- (34) Akama, T.; Kobayashi, M.; Nakai, H. *J. Comput. Chem.* **2007**, *28*, 2003-2012.
- (35) Deward, M. J. S.; Zoebisch, E. G.; Healy, E. F.; Stewart, J. J. *J. Am. Chem. Soc.* **1985**, *107*, 3902-3909.
- (36) Stewart, J. J. *J. Comput. Chem.* **1989**, *10*, 209-220.
- (37) Stewart, J. J. *J. Comput. Chem.* **1989**, *10*, 221-264.
- (38) Porezag, D.; Frauenheim, T.; Köhler, T.; Seifert, G.; Kaschner, R. *Phys. Rev. B* **1995**, *51*, 12947-12957.
- (39) Seifert, G.; Porezag, D.; Frauenheim, T. *Int. J. Quantum Chem.* **1996**, *58*, 185-192.
- (40) Elstner, M.; Porezag, D.; Jungnickel, G.; Elsner, J.; Haugk, M.; Trauenheim, Th.; Suhai, S.; Seifert, G. *Phys. Rev. B* **1998**, *58*, 7260-7268.
- (41) Koskinen, P.; Mäkinen, V. *Comput. Mater. Sci.* **2009**, *47*, 237-253.
- (42) Seifert, G.; Joswig, J.-O. *WIREs Comput. Mol. Sci.* **2012**, *2*, 456-465.
- (43) Gaus, M.; Cui, Q.; Elstner, M. *WIREs Comput. Mol. Sci.* **2014**, *4*, 49-61.
- (44) Witek, H. A.; Morokuma, K. *J. Comput. Chem.* **2004**, *25*, 1858-1864.
- (45) Zheng, G.; Irle, S.; Morokuma, K. *Chem. Phys. Lett.* **2005**, *412*, 210-216.
- (46) Settergren, N. M.; Bühlmann, P.; Amin, E. A. *J. Mol. Struct.: THEOCHEM* **2008**, *861*, 68-73.
- (47) Bloch, F. *Z. Physik* **1928**, *52*, 555-600.
- (48) Slater, J. C.; Koster, G. F. *Phys. Rev.* **1954**, *94*, 1498-1524.
- (49) Witek, H. A.; Irle, S.; Morokuma, K. *J. Chem. Phys.* **2004**, *121*, 5163-5170.
- (50) Zhechkov, L.; Heine, T.; Patchkovskii, S.; Seifert, G.; Duarte, H. A. *J. Chem. Theory Comput.* **2005**, *1*, 841-847.

- (51) Elstner, M.; Hobza, P.; Frauenheim, T.; Suhai, S.; Kaxiras, E. *J. Chem. Phys.* **2001**, *114*, 5149-5155.
- (52) Köhler, C.; Seifert, G.; Gerstmann, U.; Elstner, M.; Overhpf, H.; Frauenheim, Th. *Phys. Chem. Chem. Phys.* **2001**, *3*, 5109-5114.
- (53) Köhler, C.; Seifert, G.; Frauenheim, Th. *Chem. Phys.* **2005**, *309*, 23-31.
- (54) Köhler, C.; Frauenheim, T.; Hourahine, B.; Seifert, G.; Sternberg, M. *J. Phys. Chem. A* **2007**, *111*, 5622-5629.
- (55) Roothaan, *Rev. Mod. Phys.* **1960**, *32*, 179-185.
- (56) Gaus, M.; Cui, Q.; Elstner, M. *J. Chem. Theory Comput.* **2011**, *7*, 931-948.
- (57) Fermi, E. *Redn. Lincei* **1926**, *3*, 145-149.
- (58) Dirac, P. A. M. *Proc. R. Soc. Lond. A* **1926**, *112*, 661-677.
- (59) Weinert, M.; Davenport, J. W. *Phys. Rev. B* **1992**, *45*, 13709-13712.
- (60) Chai, J.-D. *J. Chem. Phys.* **2012**, *136*, 154104.
- (61) Kitaura, K.; Ikeo, E.; Asada, T.; Nakano, T.; Uebayasi, M. *Chem. Phys. Lett.* **1999**, *313*, 701-706.
- (62) Kitaura, K.; Sugiki, S.; Nakano, T.; Komeiji, Y.; Uebayasi, M. *Chem. Phys. Lett.* **2001**, *336*, 163-170.
- (63) Nakata, T.; Brorsen, K.; Fedorov, D. G.; Kitaura, K.; Gordon, M. S. *J. Chem. Phys.* **2011**, *134*, 124115.
- (64) Fedorov, D. G.; Kitaura, K. *J. Chem. Phys.* **2004**, *120*, 6832-6840.
- (65) Nakano, T.; Mochizuki, Y.; Yamashita, K.; Watanabe C.; Fukuzawa, K.; Segawa, K.; Okiyama, Y.; Tsukamoto, T.; Tanaka, S. *Chem. Phys. Lett.* **2012**, *523*, 128-133.
- (66) Nakano, T.; Kaminuma, T.; Sato, T.; Fukuzawa, K.; Akiyama, Y.; Uebayasi, M.; Kitaura, K. *Chem. Phys. Lett.* **2002**, *351*, 475-480.
- (67) Nakano, T.; Kaminuma, T.; Sato, T.; Akiyama, Y.; Uebayasi, M.; Kitaura, K. *Chem. Phys. Lett.* **2000**, *318*, 614-618.
- (68) Nagata, T.; Fedorov, D. G.; Kitaura, K. *Chem. Phys. Lett.* **2010**, *492*, 302-308.
- (69) Fedorov, D. G.; Jensen, J. H.; Deka, R. C.; Kitaura, K. *J. Phys. Chem. A* **2008**, *112*, 11808-11816.
- (70) Fedorov, D. G.; Avramov, P. V.; Jensen, J. H.; Kitaura, K. *Chem. Phys. Lett.* **2009**, *477*, 169-175.
- (71) Gordon, M. S.; Fedorov, D. G.; Pruitt, S. R.; Slipchenko, L. V. *Chem. Rev.* **2012**, *112*, 632-672.

Chapter 3

Density-Functional Tight-Binding Combined with the Fragment Molecular Orbital Method

3.1 Introduction

In biochemistry, nanoelectronics and many other areas of molecular science it is often necessary to deal with systems containing a large number of atoms, typically between 10^3 to 10^7 . Simulations of chemical reactions, electron transfer, electronically excited states, and even accurate structure predictions for polar or hydrogen-bonded systems, require an accurate treatment of the electronic structure, which can in principle be accomplished with quantum chemical methods based on quantum mechanics (QM methods). However, traditional QM methods scale very steeply with the system size. For instance, even the fastest *ab initio* Hartree-Fock (HF) method scales as N^{2-3} , where N is the number of atoms, and for coupled cluster (CC) theory the scaling can be as high as N^7 . This means that, although QM calculations of small and medium size systems can be routinely conducted, increasing the system size by a factor of 100 results in a HF calculation that is up to a million time more expensive, and 100 trillion times more expensive in the case of CC. Such huge computational effort is accompanied by a similarly huge increase in required computer memory and disk storage.

At present, only classical molecular mechanics (MM) is capable of treating systems consisting of millions of atoms at the full atomistic level, yet molecular dynamics (MD) simulations using molecular mechanics force fields for such tremendously large systems require the most powerful, massively parallel supercomputers available today.¹ At the same time, there is an ongoing effort to develop efficient traditional QM methods²⁻⁴ with linear scaling⁵⁻⁷ and linear scaling semi-empirical approaches, partially designed to replace MM-MD simulations in the future by QM-MD.^{8,9} Alternatively, methods using fragmentation are also becoming increasingly popular.¹⁰⁻²⁶

Although these methods do succeed in enabling much larger calculations than traditional QM approaches, the reported maximum system sizes are still only on the order of 30,000 atoms²⁷⁻³² for full QM applications. We note that, using a piecewise approach, a geometry optimization of a 150,000 atomic system has been reported.³³ Even though

fragment-based approaches have been successfully applied to QM calculations at 0 K, MD simulations with full QM fragment-based methods of large systems are rather limited.^{34,35} The density-functional tight-binding (DFTB) method is a semi-empirical QM approach applicable towards large systems. It has its origin in the computational materials sciences,³⁶ and recently it has found broad applications in organic and biological systems.³⁷ The method itself has been described in the literature on several occasions, and we therefore suffice to only briefly describe the main features and options related to our work in Section 3.2, and refer the interested reader to recent reviews.^{37–40} Essentially, DFTB is an approximate density functional theory (DFT)^{41,42} method utilizing the tight binding approach within the framework of an optimized minimal Slater-type all-valence basis set and a two-center approximation for Hamiltonian matrix elements. There are several options available. One is the self-consistent-charge (SCC) formalism, in which the interaction between atomic charges is included in the energy expression, and the atomic charges are determined iteratively until self-consistency is reached.⁴³ This option is sometimes called “DFTB2”,³⁷ as it is a second order expansion of the DFT energy around a reference density. Higher-order expansions, such as third order corrections (“DFTB3”), have been recently developed and shown to be important in polar and hydrogen-bonded systems.⁴⁴ The SCC-DFTB method is similar in spirit to other DFTB-based self-consistent charge transfer tight-binding models.^{45,46} These iterative SCC methods are all related to the ideas of density expansion in tight-binding, proposed in 1989 by Foulkes and Haydock.⁴⁷ The earliest, and methodologically most simple approach of DFTB is the non-self-consistent-charge (NCC) option, in which the atomic charge-atomic charge interaction is neglected.⁴⁸ This option, nowadays sometimes called “DFTB1”,³⁷ is approximately five to twenty times faster than the SCC option since it is non-iterative, and may not be a bad approximation for homogeneous systems with little charge polarization. Although DFTB is fast, its scaling with system size is unfavorable with $O(N^3)$ because even though no integrals are calculated, it is still necessary to diagonalize the DFTB Hamiltonian. Its memory requirement is N^2 , and combined with the cubic scaling of the computational efforts, these limitations prevent the use of DFTB for calculations of truly large systems (loosely defined as systems containing more than 10 000 atoms). Recently, however, advances have been made to reduce the cubic scaling required for full Hamiltonian matrix diagonalization: for instance, an $O(N\log N)$ -scaling divide-and-conquer⁵ formulation⁴⁹ of DFTB (mDC-DFTB) has been developed by the York group. Using their code, they were able to obtain a converged electronic density for a 1 million atom containing water cluster in around 5 minutes on 8 Intel Xeon E5520 cores.⁵⁰ Using density matrix purification methods, true

$O(N)$ linear scaling with low prefactor was demonstrated for a similar density functional based tight binding method in energy conserving Born-Oppenheimer MD simulations of systems containing less than 1,000 atoms.⁵¹

An a posteriori treatment for dispersion interaction within the framework of DFTB was first proposed by Elstner et al. to describe base pair stacking in DNA.⁵² It employs lists of “van der Waals-active” interatomic contacts and a switching function to turn off the van der Waals potential at short distances. Similar corrections are nowadays added routinely in DFT calculations and have widely become known as “Grimme dispersion”.⁵³ In 2005, Zhechkov et al. developed an alternative dispersion interaction model based on the parameterization by Rappé et al.⁵⁴ which is available for all elements of the periodic table and does not require interatomic contact lists. In both approaches, the van der Waals interactions are evaluated as a sum over pair potentials between all atoms, and hence the dispersion term is a constant for a given nuclear geometry. It is independent of the electronic structure calculation and hence easy to implement, yet has been recognized as important in computational biological and materials sciences.

The fragment molecular orbital (FMO) method^{55–59} is one of the fragment-based approaches.¹⁰ In FMO, the system is divided into fragments (also called monomers), which are calculated in the embedding electrostatic potential (ESP), obtained from the density of all fragments. These monomer calculations are repeated iteratively until convergence is reached, followed by the calculation of fragment pairs (dimers) in the presence of the embedding ESP. FMO has been applied to a variety of molecular systems including proteins,^{60,61} DNA,^{62–64} polymers⁶⁵ and inorganic systems.^{66–70}

The accuracy and scaling of FMO based on regular DFT has been discussed.^{71–74} FMO-DFT has been used for a geometry optimization⁷⁵ of chignolin, containing 138 atoms. The total energy in FMO is expanded in the many-body series.^{76,77} In this work, we use only the two-body expansion (FMO2), often reliable enough for energetics and gradients, and develop the energy and gradient of FMO-based DFTB (FMO2-DFTB). We employ both non-self-consistent-charge (first-order, DFTB1, here called NCC-DFTB)^{48,78} and self-consistent charge (second-order, DFTB2, here called SCC-DFTB)⁴³ DFTB. The accuracy of FMO-DFTB is tested on a variety of representative molecules in terms of energy and optimized geometry, and the computational efficiency as well as scaling behavior with respect to system size and parallelism are discussed in detail.

3.2 Methodology

3.2.1 Density-Functional Tight-Binding (DFTB)

The DFTB method has been described in detail elsewhere,^{37–40,43,44} therefore we only provide a brief summary here. The total energy of NCC-DFTB, E^{NCC} , is written as

$$E^{\text{NCC}} = \sum_i \sum_{\mu\nu} n_i c_{\mu i}^* c_{\nu i} H_{\mu\nu}^0 + \sum_{A>B} E_{AB}^{\text{rep}} \quad (3.1)$$

where μ and ν denote atomic orbitals (AO), A and B label atoms, and n_i is the occupation number of the i -th molecular orbital (MO). The $c_{\mu i}$ are the expansion coefficients of the i -th MO in an AO basis. $H_{\mu\nu}^0$ is the non-perturbed (i.e., atomic- and diatomic-based) Hamiltonian in the basis of optimized AOs, precomputed for atoms and diatomic systems over a range of bond lengths in reference DFT calculations. E_{AB}^{rep} is the two-body repulsive energy term, which is precomputed and tabulated as a function of interatomic distance R_{AB} from DFT calculations of model systems containing the chemical elements of the A and B atoms. As a result of this approach, E_{AB}^{rep} is independent of the electronic structure and only a function of the interatomic distances. It is normally short-ranged and extends usually only up to maximally 1.5 times the equilibrium bond lengths.

The MO coefficients \mathbf{c} in eq 3.1 are variationally determined by solving the equation, $\mathbf{H}\mathbf{c} = \mathbf{S}\mathbf{c}\epsilon$, where \mathbf{S} is the overlap matrix, readily precomputed and tabulated for the optimized AOs used in the construction of as a function of R_{AB} . Because does not depend on \mathbf{c} , NCC-DFTB is a non-iterative method and hence computationally very economical. This method has been successfully applied to a number of systems,^{48,79–82} mostly for homopolar systems such as carbon-based nanostructures, although the bandstructure of heteropolar systems can also be described reasonably well.^{40,80,83}

In many polar systems one has to consider self-consistent, second-order terms of charge fluctuations.⁴³ In this case, the calculation of the charge density becomes iterative. Using routine density matrix update algorithms, typically between 5 and 20 SCC iteration cycles are required to achieve convergence. The total energy of SCC-DFTB, E^{SCC} , is written as

$$E^{\text{SCC}} = E^{\text{NCC}} + \frac{1}{2} \sum_{AB} \gamma_{AB} \Delta q_A \Delta q_B \quad (2)$$

where γ_{AB} depends on the distance R_{AB} between two atoms A and B and their chemical hardness.⁸⁴ γ_{AB} in the limit of long distances behaves as $1/R_{AB}$ and at short distances accounts for the chemical hardness of the chemical element in question, expressed by a Hubbard parameter U_A that is computed using DFT as a numerical derivative of the DFT atomic orbital energy (normally the highest occupied AO) with respect to its orbital occupation. The Hubbard U_A values are related to atomic ionization potentials and

electron affinities. Charge fluctuations $\delta\rho$ around the reference electron density ρ^0 in SCC-DFTB are expressed by a spherical point charge model with partial atomic charges Δq_A . It is the deviation of the Mulliken population on atom A from that in the neutral atom q_A^0 , that is $\Delta q_A = q_A - q_A^0$, where

$$q_A = \frac{1}{2} \sum_i n_i \sum_{\mu \in A} \sum_{\nu} (c_{\mu i}^* c_{\nu i} S_{\mu\nu} + c_{\nu i}^* c_{\mu i} S_{\nu\mu}) \quad (3.3)$$

Clearly, the last term in eq 3.2 requires an iterative calculation since atomic populations depend on the MO coefficients \mathbf{c} . We note that other charge partitioning schemes have been applied and reported for SCC-DFTB,⁸⁵ but Mulliken population analysis remains the most widely used method for determining atomic charges.

The derivative of eq 3.2 with respect to MO coefficients defines the SCC-DFTB Hamiltonian matrix in the AO basis,

$$H_{\mu\nu} = H_{\mu\nu}^0 + \frac{1}{2} S_{\mu\nu} \sum_C (\gamma_{AC} + \gamma_{BC}) \Delta q_C \quad \mu \in A, \nu \in B \quad (3.4)$$

The derivative of the SCC-DFTB energy with respect to the x coordinate of atom α (note that throughout this paper x in the derivatives can be replaced by y or z) is

$$\begin{aligned} \frac{\partial E^{\text{SCC}}}{\partial R_{\alpha x}} = & \sum_{A \neq \alpha} \sum_{\mu \in A} \sum_{\nu \in \alpha} \sum_i n_i c_{\mu i}^* c_{\nu i} \left\{ 2 \frac{\partial H_{\mu\nu}^0}{\partial R_{\alpha x}} \right. \\ & \left. - 2\varepsilon_i \frac{\partial S_{\mu\nu}}{\partial R_{\alpha x}} + \frac{\partial S_{\mu\nu}}{\partial R_{\alpha x}} \sum_C (\gamma_{AC} + \gamma_{\alpha C}) \Delta q_C \right\} \\ & + \Delta q_{\alpha} \sum_{A \neq \alpha} \Delta q_A \frac{\partial \gamma_{A\alpha}}{\partial R_{\alpha x}} + \sum_{A \neq \alpha} \frac{\partial E_{A\alpha}^{\text{rep}}}{\partial R_{\alpha x}}. \end{aligned} \quad (3.5)$$

3.2.2 Formulation of FMO-DFTB

The total energy E in the two-body FMO expansion (FMO2)⁵⁵ is

$$E = \sum_I^N E_I + \sum_{I>J}^N (E_{IJ} - E_I - E_J) \quad (3.6)$$

where N is the number of fragments, and the E_X terms are the energies of fragments ($X = I$) and their pairs ($X = IJ$). For SCC-DFTB, they are defined as

$$E_X = E'_X + E_X^V \quad (3.7)$$

whereas for NCC-DFTB, the expression is

$$E_X = E'_X \quad (3.8)$$

The internal energy of X is defined as

$$E'_X = \sum_{i \in X} \sum_{\mu\nu \in X} n_i^X c_{\mu i}^{X*} c_{\nu i}^X H_{\mu\nu}^{0,X} + \sum_{A>B \in X} E_{AB}^{\text{rep}} + \frac{1}{2} \sum_{AB \in X} \gamma_{AB} \Delta q_A^X \Delta q_B^X \quad (3.9)$$

and the embedding energy is

$$E_X^V = \sum_{A \in X} \sum_{K \neq X} \sum_{C \in K} \gamma_{AC} \Delta q_A^X \Delta q_C^K \quad (3.10)$$

Δq_A^X is the charge on atom A in fragment X . Note that A and C can be the same atom, if fragments X and K are connected via a covalent bond. The internal energy of fragment X includes the Coulomb interaction of charges within X , while the embedding energy is the interaction between charges in X and those outside of X (in all other fragments).

Using these definitions, in a same way as in other FMO methods,⁸⁶ it is possible to rewrite eq 3.6 for SCC-DFTB as follows,

$$E = \sum_I^N E'_I + \sum_{I>J}^N (E'_{IJ} - E'_I - E'_J) + \sum_{I>J}^N \Delta E_{IJ}^V \quad (3.11)$$

For NCC-DFTB the expression is (compare eqs 3.6 and 3.8)

$$E = \sum_I^N E'_I + \sum_{I>J}^N (E'_{IJ} - E'_I - E'_J) \quad (3.12)$$

In SCC-DFTB, the coupling of the charge transfer to the embedding potential is

$$\Delta E_{IJ}^V = \sum_{A \in IJ} \sum_{K \notin I,J} \sum_{C \in K} \gamma_{AC} \Delta \Delta q_A^{IJ} \Delta q_C^K \quad (3.13)$$

and the charge transfer between fragments I and J for atom A is

$$\Delta \Delta q_A^{IJ} = \Delta q_A^{IJ} - \Delta q_A^I \delta_{A \in I} - \Delta q_A^J \delta_{A \in J} \quad (3.14)$$

where $\delta_{A \in I} = 1$ when atom A belongs to fragment I , otherwise it is zero.

In NCC-DFTB the charge interaction is not considered, and thus $E_{IJ}' \approx E'_I + E'_J$. On the other hand, in SCC-DFTB one has to evaluate the fragment interactions for separated pairs, which scales in principle quadratic with system size N . However, the interfragment charge transfer is short-ranged and can be neglected if the interfragment

distance R_{IJ} is larger than a certain threshold. In this case, a self-consistent field (SCF) calculation of the far separated dimer is not required, and the interfragment interaction is evaluated using the electrostatic dimer (ES-DIM) approximation instead.⁸⁶ Thus, for dimers IJ calculated with this approximation, $\Delta\Delta q_A^{IJ} = \Delta E_{IJ}^V = 0$. Different from quantum-effects such as charge transfer and exchange-repulsion, the electrostatic interaction decays with distance R slowly as $1/R$ and has to be evaluated for all separated dimers.

The energy of a separated dimer in FMO-DFTB should in principle be given by

$$E'_{IJ} \approx E'_I + E'_J + \sum_{A \in I} \sum_{B \in J} (E_{AB}^{\text{rep}} + \gamma_{AB} \Delta q_A^I \Delta q_B^J) \quad (3.15)$$

However, the repulsion energy E_{AB}^{rep} quickly decays with the interatomic distance and with the typical value of the ES-DIM threshold, and therefore can be neglected. Therefore, the energy of far separated dimers in FMO-based SCC-DFTB is evaluated as

$$E'_{IJ} \approx E'_I + E'_J + \sum_{A \in I} \sum_{B \in J} \gamma_{AB} \Delta q_A^I \Delta q_B^J \quad (3.16)$$

For the energy gradient, one needs to define the Hamiltonian matrix of fragment X , which for SCC-DFTB is

$$H_{\mu\nu}^X = H_{\mu\nu}^{\text{SCC},X} + V_{\mu\nu}^X + P_{\mu\nu}^X \quad (3.17)$$

where $H_{\mu\nu}^{\text{SCC},X}$ is the Hamiltonian matrix of fragment X according to eq 3.4, which includes the Coulomb interaction for charges within X . For NCC-DFTB one has

$$H_{\mu\nu}^X = H_{\mu\nu}^{0,X} + P_{\mu\nu}^X \quad (3.18)$$

where $H_{\mu\nu}^{0,X}$ corresponds to $H_{\mu\nu}^0$ of fragment X in eq 3.4. The ESP acting on X is given by

$$V_{\rho\sigma}^X = \frac{1}{2} S_{\rho\sigma}^X \sum_{K \neq X} \sum_{D \in K}^N (\gamma_{AD} + \gamma_{BD}) \Delta q_D^K. \quad \rho \in A, \sigma \in B \quad (3.19)$$

is the hybrid orbital projection (HOP) operator,⁸⁷ which is introduced in FMO for fragments connected by detached covalent bonds (HOP is not used in molecular clusters). The HOP representation in AO basis is

$$P_{\mu\nu}^X = B \sum_{\rho\sigma} S_{\mu\rho}^X \tilde{D}_{\rho\sigma}^X S_{\sigma\nu}^X \quad (3.20)$$

where $\tilde{D}_{\mu\nu}^X$ is the density matrix of the hybrid orbitals⁸⁸ and B is a universal constant, usually set to 10^6 hartree. The hybrid orbitals are precomputed for each atom type using a suitable model compound, e.g. CH₄ when detaching bonds at sp³ carbons).

3.2.3 Gradient of FMO-DFTB

Below, we derive the gradient for a closed shell singlet, that is $n_i = 2$ for all occupied MOs, which simplifies the formulation of FMO-DFTB with the ES-DIM approximation. By taking the derivative of eq 3.9, one obtains

$$\begin{aligned} \frac{\partial E'_X}{\partial R_{\alpha x}} = & \sum_{(A \neq \alpha) \in X} \sum_{\mu \in A} \sum_{\nu \in \alpha} \left\{ 2D_{\mu\nu}^X \frac{\partial H_{\mu\nu}^{0,X}}{\partial R_{\alpha x}} - 2W_{\mu\nu}'^X \frac{\partial S_{\mu\nu}^X}{\partial R_{\alpha x}} \right. \\ & \left. + D_{\mu\nu}^X \frac{\partial S_{\mu\nu}^X}{\partial R_{\alpha x}} \sum_{C \in X} (\gamma_{AC} + \gamma_{\alpha C}) \Delta q_C^X + 2D_{\mu\nu}^X \frac{\partial P_{\mu\nu}^X}{\partial R_{\alpha x}} \right\} \\ & + \Delta q_\alpha^X \sum_{(A \neq \alpha) \in X} \Delta q_A^X \frac{\partial \gamma_{A\alpha}}{\partial R_{\alpha x}} + \sum_{(A \neq \alpha) \in X} \frac{\partial E_{A\alpha}^{\text{rep}}}{\partial R_{\alpha x}}. \end{aligned} \quad (3.21)$$

The derivative of the HOP matrix $P_{\mu\nu}^X$ in FMO-DFTB is the same as in regular FMO.⁸⁸ In the SCC-DFTB energy gradient for FMO, we did not include the derivatives of MO coefficients with respect to nuclear coordinates. The internal Lagrangian $W_{\mu\nu}'^X$ in eq 3.21 is defined by subtracting the ESP contribution from the usual Lagrangian $W_{\mu\nu}^X$

$$W_{\mu\nu}'^X = W_{\mu\nu}^X - \frac{1}{2} \sum_{\rho\sigma} D_{\mu\rho}^X V_{\rho\sigma}^X D_{\sigma\nu}^X \quad (3.22)$$

and

$$W_{\mu\nu}^X = \frac{1}{2} \sum_{\rho\sigma} D_{\mu\rho}^X H_{\rho\sigma}^X D_{\sigma\nu}^X \quad (3.23)$$

where $D_{\mu\nu}^X$ is the density matrix of fragment X .

Second, we need to calculate the derivative of the embedding energy in eq 3.13.

For atom α in dimer IJ ($\alpha \in IJ$) one obtains

$$\begin{aligned} \frac{\partial \Delta E_{IJ}^V}{\partial R_{\alpha x}} = & \Delta \Delta q_\alpha^{IJ} \sum_{K \neq I,J} \sum_{C \in K} \Delta q_C^K \frac{\partial \gamma_{\alpha C}}{\partial R_{\alpha x}} \\ & + \sum_{\mu \in \alpha} \sum_{\nu} \left(\Delta \tilde{W}_{\mu\nu}^{IJ,\alpha} S_{\mu\nu}^{IJ} + \Delta D_{\mu\nu}^{IJ} \frac{\partial S_{\mu\nu}^{IJ}}{\partial R_{\alpha x}} \right) \sum_{K \neq I,J} \sum_{C \in K} \gamma_{\alpha C} \Delta q_C^K \end{aligned} \quad (3.24)$$

and for $\alpha \in (K \neq I,J)$,

$$\begin{aligned} \frac{\partial \Delta E_{IJ}^V}{\partial R_{\alpha x}} &= \Delta q_{\alpha}^K \sum_{A \in IJ} \Delta \Delta q_A^{IJ} \frac{\partial \gamma_{A\alpha}}{\partial R_{\alpha x}} \\ &+ \sum_{\mu \in \alpha} \sum_{\nu} \left(\tilde{W}_{\mu\nu}^{K,\alpha} S_{\mu\nu}^K + D_{\mu\nu}^K \frac{\partial S_{\mu\nu}^K}{\partial R_{\alpha x}} \right) \sum_{A \in IJ} \gamma_{A\alpha} \Delta \Delta q_A^{IJ} \end{aligned} \quad (3.25)$$

where

$$\tilde{W}_{\mu\nu}^{X,\alpha} = -\frac{1}{2} \sum_{\rho\sigma} D_{\mu\rho}^X \frac{\partial S_{\rho\sigma}^X}{\partial R_{\alpha x}} D_{\sigma\nu}^X \quad (3.26)$$

$$\Delta \tilde{W}_{\mu\nu}^{IJ,\alpha} = \tilde{W}_{\mu\nu}^{IJ,\alpha} - \left(\tilde{W}_{\mu\nu}^{I,\alpha} \oplus \tilde{W}_{\mu\nu}^{J,\alpha} \right) \quad (3.27)$$

and

$$\begin{aligned} \tilde{W}_{\mu\nu}^{I,\alpha} \oplus \tilde{W}_{\mu\nu}^{J,\alpha} &= \tilde{W}_{\mu\nu}^{I,\alpha} + \tilde{W}_{\mu\nu}^{J,\alpha} && \text{for } \mu\nu \in I, J \\ &= \tilde{W}_{\mu\nu}^{I,\alpha} && \text{for } \mu\nu \in I \text{ and } \mu\nu \notin J \\ &= \tilde{W}_{\mu\nu}^{J,\alpha} && \text{for } \mu\nu \in J \text{ and } \mu\nu \notin I \\ &= 0 && \text{for all other cases.} \end{aligned}$$

The density difference matrix $\Delta D_{\mu\nu}^{IJ}$ is

$$\Delta D_{\mu\nu}^{IJ} = D_{\mu\nu}^{IJ} - \left(D_{\mu\nu}^I \oplus D_{\mu\nu}^J \right) \quad (3.28)$$

The gradient of the ES-DIM approximation is obtained by differentiating eq 3.16. For the derivative with respect to the x coordinate of atom $\alpha \in I$,

$$\begin{aligned} \frac{\partial E_{IJ}'}{\partial R_{\alpha x}} &= \Delta q_{\alpha}^I \sum_{B \in J} \Delta q_B^J \frac{\partial \gamma_{\alpha B}}{\partial R_{\alpha x}} \\ &+ \sum_{\mu \in \alpha} \sum_{\nu} \left(\tilde{W}_{\mu\nu}^{I,\alpha} S_{\mu\nu}^I + D_{\mu\nu}^I \frac{\partial S_{\mu\nu}^I}{\partial R_{\alpha x}} \right) \sum_{B \in J} \Delta q_B^J \gamma_{\alpha B} \end{aligned} \quad (3.29)$$

and for $\alpha \in J$,

$$\begin{aligned} \frac{\partial E_{IJ}'}{\partial R_{\alpha x}} &= \Delta q_{\alpha}^J \sum_{A \in I} \Delta q_A^I \frac{\partial \gamma_{A\alpha}}{\partial R_{\alpha x}} \\ &+ \sum_{\mu \in \alpha} \sum_{\nu} \left(\tilde{W}_{\mu\nu}^{J,\alpha} S_{\mu\nu}^J + D_{\mu\nu}^J \frac{\partial S_{\mu\nu}^J}{\partial R_{\alpha x}} \right) \sum_{A \in I} \Delta q_A^I \gamma_{A\alpha} \end{aligned} \quad (3.30)$$

Eqs 3.29 and 3.30 describe the gradients of the electrostatic (charge-charge) interaction between two fragments.

3.2.4 Dispersion Interaction for FMO-DFTB

We implemented the dispersion interaction model based on the formulation by Zhechkov et al.⁸⁹ The dispersion interaction E^{disp} is independent of the electronic

structure, and is given as a sum of all atomic pairwise contributions E_{AB}^{disp} for atoms A and B ,⁸⁹

$$E^{\text{disp}} = \sum_{A>B} E_{AB}^{\text{disp}} \quad (3.31)$$

In FMO, the above equation becomes for the dispersion energy of fragment X ,

$$E_X^{\text{disp}} = \sum_{A>B \in X} E_{AB}^{\text{disp}} \quad (3.32)$$

E_X^{disp} is added to the internal energy in eq 3.9. Also, in the separated dimer approximation, we add the dispersion contribution to $E_{IJ}' - E_I' - E_J'$,

$$\Delta E_{IJ}^{\text{disp}} = \sum_{A \in I} \sum_{B \in J} E_{AB}^{\text{disp}} \quad (3.33)$$

Parameters for the dispersion interaction are taken from the work by Rappé et al.⁵⁴ We denote the dispersion interaction with the suffix of “-D” hereafter. Although we implemented also the dispersion interaction formulated by Elstner et al.,⁵² we use in the present work the formulation by Zhechkov et al. for actual calculations. We verified by numeric tests that the dispersion energy in FMO-DFTB-D is identical to that in DFTB-D, as should be because it is a parametrized ad hoc correction independent of fragmentation.

3.2.5 Computational Details

The DFTB and FMO-DFTB methods were implemented in GAMESS-US.⁹⁰ In the DFTB implementation, the Broyden charge mixing⁹¹ was used to accelerate the convergence of SCF calculations with the same type of thresholds as in the rest of GAMESS. In both FMO-DFTB and full DFTB gradient calculations, the derivatives of the Hamiltonian and overlap matrix elements were calculated numerically, whereas other derivatives were computed analytically.

FMO-DFTB was parallelized with the generalized distributed data interface (GDDI)⁹² by assigning one monomer or dimer calculation per GDDI group. The main cost of a DFTB calculation is the matrix diagonalization, which is hard to efficiently parallelize for the matrix sizes we encounter in typical FMO fragments. Therefore, we always used the group size of 1 CPU core, i.e., individual monomer and dimer calculations in FMO-DFTB were executed sequentially on different CPU cores, whereas the load balancing of distributing these calculations was dynamic, as implemented in GAMESS/GDDI.⁹²

All computations of accuracy and scaling tests were performed using a PC cluster consisting of several nodes equipped with dual E5-2650 Xeon CPUs (2.0 GHz, 8 cores each), 64 GB of DDR3-1600 memory and a SATA hard disk. The nodes were connected with Infiniband (used in the IP mode). For the parallel efficiency tests we used 1 to 8 nodes (16-128 CPU cores).

We used the mio⁴³ set of DFTB parameters, except when performing calculations on DNA sequences, for which we used the matsci⁹³ set. Both parameter sets are freely available from the DFTB web site.⁹⁴ The ES-DIM approximation was used with the threshold value of 2.0 (unitless⁸⁶) applied to the interfragment distance, defined as the separation between two closest atoms in the two fragments divided by the sum of the atomic van der Waals radii.⁸⁶ For a typical case of the contact atoms being O and H, the distance of 2.0 corresponds to 9.83 bohr. The DFTB parameters are such that the interaction for distances exceeding 10 bohr are usually zero, which justifies the neglect of the repulsive energy term in the ES-DIM approximation (see eqs 3.15 and 3.16).

Geometry optimizations were performed until the root mean square (rms) and maximum gradient values became smaller than $1/3 \times 10^{-4}$ and 10^{-4} hartree/bohr, respectively (OPTTOL= 10^{-4} in GAMESS). Hybrid orbitals for HOP operators for sp^3 carbons were generated by performing the Pipek-Mezey localization⁹⁵ of SCC-DFTB MOs using the mio parameters for methane in its equilibrium geometry at the same level of theory. The fragmentation of polypeptides was performed at the C_α atoms, as usual in FMO. For DNA segments we compared two fragmentation schemes as described below.

The accuracy of single point energy calculations was evaluated for extended polyaniline (COMe-(Ala)_n-NHMe, $n = 10, 20, \dots, 200$) partitioned into fragments containing 1, 2, 4 and 5 amino acid residues. The accuracy of optimized geometries is discussed for (a) the α -helix, β -turn, and extended form of polyaniline COMe-(Ala)₂₀-NHMe, (b) a short double stranded DNA segment of CGATCG nucleotides (PDB: 1AGL), (C₁₁₅P₁₀N₄₆H₁₃₆O₇₈) and (c) a small Trp-cage protein (PDB: 1L2Y) with all residues neutralized using GaussView 5.0.⁹⁶

For Trp-cage we used the PDB structure as the initial geometry, whereas for all other systems the initial structures were constructed using the “protein” and the “nucleic” programs implemented in TINKER 6.0,⁹⁷ and they were subsequently optimized using the “minimize” program with the AMBER99 force field parameters.⁹⁸ Geometry optimizations⁹⁹ at full SCC-DFTB and FMO-DFTB were then performed using RUNTYP=OPTIMIZE in GAMESS, except for the optimization of the ~1 million atoms

system, for which we used RUNTYP=OPTFMO, and LBFGS when dispersion interaction is included.

For the evaluation of the FMO-DFTB scaling in terms of the system size, we used a series of globular water clusters $((\text{H}_2\text{O})_n, n = 256, 512, 1024, 2048, 3072, 4096, 5120, \text{ and } 6144)$, the α -helix of polyalanine ($\text{COMe}-(\text{Ala})_n\text{-NHMe}, n = 100, 200, \dots, 1900, \text{ and } 1998)$, and a quadratic slab of C_{60} fullerite with the square slabs containing from 1×1 to 7×7 unit cells of face centered cubic (fcc) fullerite with the fixed thickness of 3 layers of fullerenes (only its square length was varied, not the thickness). Water clusters were produced and optimized using the “addxyz” and the “minimize” modules in TINKER. For modeling the fullerite slab, a single C_{60} was first optimized with SCC-DFTB, then the optimized C_{60} molecules were aligned according to the fcc symmetry of fullerite with the unit cell length¹⁰⁰ of 14.04 Å.

The parallel efficiency was evaluated on a 40×40 lattice of fullerite, containing 590 520 atoms. Finally, we performed a full geometry optimization of a 53×53 unit cells of fullerite, containing 1 030 440 atoms, using 128 CPU cores (8 nodes). We performed this optimization with and without the dispersion interaction. This fullerite slab has the size of $74.4 \text{ nm} \times 74.4 \text{ nm}$. For comparison, the only inorganic system of comparable size fully optimized with FMO-DFT is the boron nitride (BN) nanoribbon ring with a diameter of 105 nm,⁶⁸ which contains a much smaller number of atoms (7878).

3.3 Results and Discussions

3.3.1 Accuracy of FMO-DFTB

The accuracy of FMO-DFTB compared to full SCC-DFTB was evaluated for the extended form of polyalanine (Figure 3.1) using SCC-DFTB. We note that throughout this section, all numerical results for FMO-DFTB were obtained with SCC-DFTB combined with FMO, so we use FMO-DFTB as a short-hand notation instead of FMO-SCC-DFTB. The number of atoms ranges from 112 to 2012, and we compared five fragmentations of n residues per fragment ($n = 1, \dots, 5$). The error decreases with the fragment size, as expected.

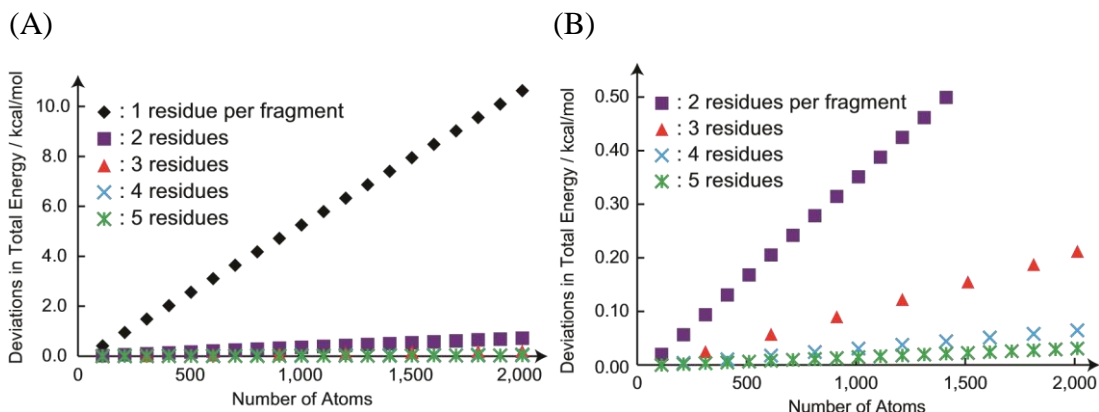


Figure 3.1. (A) Deviations of the total energy of FMO-DFTB from full SCC-DFTB for the extended polyalanine (COMe-(Ala) $_n$ -NHMe, $n = 10, 20, \dots, 200$). To show the deviations better, the same set of errors is plotted in (B) with a magnified scale.

The largest error is observed for the fragmentation of 1 residue per fragment: for 2012 atoms the error in total energy is about 10.6 kcal/mol. When the fragment size is doubled, this error is dramatically reduced to only 0.72 kcal/mol for the largest system, and by using a fragmentation of 3 (the edge fragments contain 4 residues), 4 and 5 residues per fragment, the errors become 0.21, 0.07 and 0.03 kcal/mol, respectively. The error is affected by the semantic periodicity (i.e., not a strict geometric periodicity) of the extended form, with the period of two residues. The CO groups face up and down alternatively, resulting in the two adjacent fragments having an opposite dipole moment. To test the accuracy of the ES-DIM approximation (eq 3.16), we performed a full calculation of the interfragment Coulombic interactions for comparison. The difference of the total energy computed with and without the approximation was negligibly small, 1.02×10^{-3} kcal/mol for COMe-(Ala) $_{200}$ -NHMe of the extended form with 1 residue per fragment. Thus we see that the ES-DIM approximation is very accurate in FMO-DFTB, in agreement with other FMO studies.⁷² It is also very efficient computationally, reducing the timing for the extended form of COMe-(Ala) $_{200}$ -NHMe with 1 residue per fragment from 171 to 10 seconds on 1 CPU core.

We note that the error of FMO in general and FMO-DFT in particular is known to increase with the basis size, which is related to the increased importance of interfragment quantum effects (such as charge transfer).^{72,75,101} On the other hand, FMO errors for minimum basis sets such as STO-3G are known to be very small.⁷² DFTB also uses a minimum basis set, hence the accuracy of FMO-DFTB is high.

To demonstrate that the dispersion in FMO-DFTB-D is exact, we performed a single point calculation with FMO-DFTB-D and full DFTB-D for

COMe-(Ala)₂₀₀-NHMe of the extended form with n residues per fragment ($n = 1, \dots, 5$). The dispersion energy in full DFTB-D and FMO-DFTB-D was exactly identical, 8.894040160 Hartree. The gradient of our dispersion implementation is also exact.

Next, to check the accuracy of optimized structures, we performed geometry optimizations with FMO-DFTB and full SCC-DFTB using fragments containing 1, 2, 4, and 5 residues and dividing COMe-(Ala)₂₀-NHMe into 20, 10, 5, and 4 fragments, respectively. Table 3.1 shows the relative energies and root-mean-square deviation (rmsd) for the optimized structures of the α -helix, β -turn, and extended form. Hydrogen atoms are included and massweighting is not used when rmsd values are calculated.

Table 3.1. FMO-DFTB and full SCC-DFTB total energies (Hartree) and rmsd (Å) for COMe-(Ala)₂₀-NHMe between geometries optimized with the two methods

	Conformer	1 res./fragm.	2 res./fragm.	4 res./fragm.	5 res./fragm.	Full SCC-DFTB
Energy	α -helix	-268.521608	-268.521370	-268.521072	-268.521342	-268.521568
	β -turn	-268.489373 (+20.2)	-268.490882 (+19.1)	-268.491555 (+18.7)	-268.491621 (+18.7)	-268.491889 (+18.6)
	extended	-268.445252 (+47.9)	-268.445374 (+47.7)	-268.445371 (+47.7)	-268.445394 (+47.7)	-268.445325 (+47.8)
rmsd	α -helix	0.031 (0.025)	0.044 (0.039)	0.028 (0.020)	0.008 (0.008)	0.000
	β -turn	0.118 (0.119)	0.082 (0.032)	0.081 (0.033)	0.031 (0.021)	0.000
	extended	0.148 (0.055)	0.124 (0.050)	0.099 (0.000)	0.175 (0.000)	0.000

^a The values in parentheses are the energies relative to the α -helix (kcal/mol).

^b rmsd values are shown for structures optimized with FMO-DFTB and full SCC-DFTB, starting from the same initial geometry. The values in parentheses almost always correspond to different local minima, obtained by taking FMO-DFTB structures as initial structures and reoptimizing them with full SCC-DFTB.

Full SCC-DFTB predicts the α -helix to be the most stable isomer, with the β -turn and extended form being less stable by 18.6 and 47.8 kcal/mol, respectively. This trend is in qualitative agreement with FMO-MP2 results¹⁰² for COMe-(Ala)₁₀-NHMe. To QM contributions one can add solvent¹⁰² and finite temperature¹⁰³ corrections. The relative energies of the three isomers of polyalanine obtained with FMO-DFTB are in good agreement with full SCC-DFTB: the largest deviation for relative energies of the β -turn is 1.6 kcal/mol for 1 residue per fragment and it is 0.1 kcal/mol for 5 residues per fragment. The relative energies of the extended form have errors of only 0.1 kcal/mol. With the partitioning of 2 residues per fragment, an accuracy of 1 kcal/mol with respect to the full SCC-DFTB calculation is achieved for all relative energies.

The optimized structures are also quite accurate with rmsd values not exceeding 0.175 Å, as shown in Table 1. The presence of many local minima complicates a systematic comparison, because the minimum search may converge to different minima in FMO-DFTB and full SCC-DFTB. Although the difference of gradient elements between these two methods is small, the geometry optimization pathway becomes notably different for the case of flat PESs. In order to eliminate the problem associated with the existence of many local minima, in addition to the optimization using FMO-DFTB and full SCC-DFTB using the same initial geometry, we reoptimized the structures at the full SCC-DFTB level starting from FMO-DFTB minima. The rmsd values obtained in this way gives the true deviation in the quality of optimized geometry between FMO-DFTB and full SCC-DFTB. These values, given in parentheses in Table 1, becomes much smaller than those outside parentheses for the fragmentations of 2 residues per fragment or more, whereas for 1 residue per fragment the improvement is not uniform. This shows that for 1 residue-fragmentation the error is not always related to the fact that the local minima are different, consistent with the larger error in total energies for this particular choice of fragment size. For the partitioning of 2 residues per fragment the rmsd values for the same local minima are 0.050 Å or smaller. This improvement is especially pronounced for the extended form, which is particularly flexible: the rmsd values of 0.124, 0.099, and 0.175 (Å) for 2, 4, and 5 residues per fragment when a different set of minima is compared become 0.050, 0.000, and 0.000 (Å) when the optimized FMO-DFTB structure is used as initial geometry in full SCC-DFTB geometry optimizations.

Table 2 shows a comparison of bond lengths and angles computed at the minima obtained with FMO-DFTB and full SCC-DFTB. The accuracy in reproducing bond lengths and bond angles is satisfactory, whereas some dihedral peptide angles vary by as much as 10.6 degrees for the fragmentation of 1 residue per fragment, reduced to 3.7

degrees by doubling the fragment size. The accuracy of FMO-DFTB in terms of rmsd, bond lengths and angles is similar or better compared to FMO-RHF/3-21G,⁹⁹ although we note that we use a polypeptide with twice as many residues, so the results are not directly comparable.

Table 3.2. rmsd between FMO-DFTB and full SCC-DFTB optimized geometrical parameters for COMe-(Ala)₂₀-NHMe. N indicates the number of fragments per residue, and the values in parentheses are maximum deviations. ϕ , ψ , and ω define the dihedral angles of C'(i-1)-N(i)-C_α(i)-C'(i), N(i)-C_α(i)-C'(i)-N(i+1), and C_α(i)-C'(i)-N(i+1)-C_α(i+1), respectively, where *i* is the residue number.

Conformer	<i>n</i>	Bond length (Å)	Bond angle (deg)	ϕ (deg)	ψ (deg)	ω (deg)
α -helix	1	0.0004 (0.0014)	0.065 (0.398)	0.80 (2.50)	0.47 (0.95)	0.22 (0.74)
	2	0.0003 (0.0010)	0.045 (0.178)	0.86 (2.53)	0.49 (1.36)	0.31 (0.69)
	4	0.0002 (0.0005)	0.017 (0.056)	0.33 (0.84)	0.20 (0.51)	0.13 (0.30)
	5	0.0001 (0.0003)	0.009 (0.030)	0.19 (0.46)	0.09 (0.21)	0.05 (0.08)
β -turn	1	0.0004 (0.0018)	0.124 (0.880)	2.83 (10.57)	1.52 (4.56)	0.73 (1.70)
	2	0.0002 (0.0009)	0.075 (0.336)	0.92 (2.05)	1.03 (3.71)	0.40 (1.08)
	4	0.0002 (0.0010)	0.065 (0.414)	0.90 (2.79)	1.01 (3.39)	0.39 (0.99)
	5	0.0001 (0.0006)	0.036 (0.216)	0.52 (1.76)	0.35 (0.87)	0.18 (0.33)
extended	1	0.0002 (0.0008)	0.055 (0.231)	0.35 (0.68)	0.27 (0.56)	0.21 (0.36)
	2	0.0001 (0.0004)	0.028 (0.121)	0.21 (0.48)	0.35 (0.63)	0.15 (0.29)
	4	0.0001 (0.0002)	0.022 (0.101)	0.21 (0.49)	0.30 (0.58)	0.13 (0.27)
	5	0.0001 (0.0004)	0.037 (0.154)	0.32 (0.62)	0.34 (0.65)	0.21 (0.58)

For the DNA benchmark system, a CGATCG double-stranded helix segment was optimized with both full SCC-DFTB and FMO-DFTB methods. We investigated two alternative fragmentation schemes by detaching bonds C-C bonds at the 4' and 5' carbon atoms as schematically shown in Figure 3.2A. The two resulting optimized structures are superimposed on the full SCC-DFTB geometry in Figure 3.2B. Compared to full SCC-DFTB, the difference of the total energy and the rmsd for optimized FMO-DFTB structures with the fragmentation at 5' carbon atoms was +2.12 kcal/mol and 0.071 Å, respectively. On the other hand, for the fragmentation at 4' carbon atoms the energy difference and rmsd of the optimized structures was -2.22 kcal/mol and 0.402 Å, respectively. The full SCC-DFTB single point calculation at the FMO-DFTB optimized geometry (with the fragmentation at 4' carbon atoms) shows that FMO-DFTB found a more stable local minimum by 3.92 kcal/mol than full SCC-DFTB. The geometry optimization with full SCC-DFTB starting with the FMO-DFTB optimized structure (with the fragmentation at 4' carbon atoms) resulted in a different local minimum, for which the rmsd between FMO-DFTB and full SCC-DFTB was 0.041 Å. The larger rmsd value obtained above (0.402 Å) stems from the difference in the local minima.

We also performed geometry optimizations for the neutralized Trp-cage (PDB: 1L2Y) 0.067 and 0.044 Å, for the fragmentation of 1 and 2 residues per fragment, respectively, whereas the errors in the total energy were +1.20 and +0.82 kcal/mol, respectively. The small rmsd values imply that the character of the minima found by FMO-DFTB is similar to those found using full SCC-DFTB (see Figure 3.3). The deviation of the optimized structures at FMO-DFTB is very small as demonstrated by their small rmsd values. Most importantly, the positions of backbone atoms and hydrogen bonds are well reproduced by FMO-DFTB.

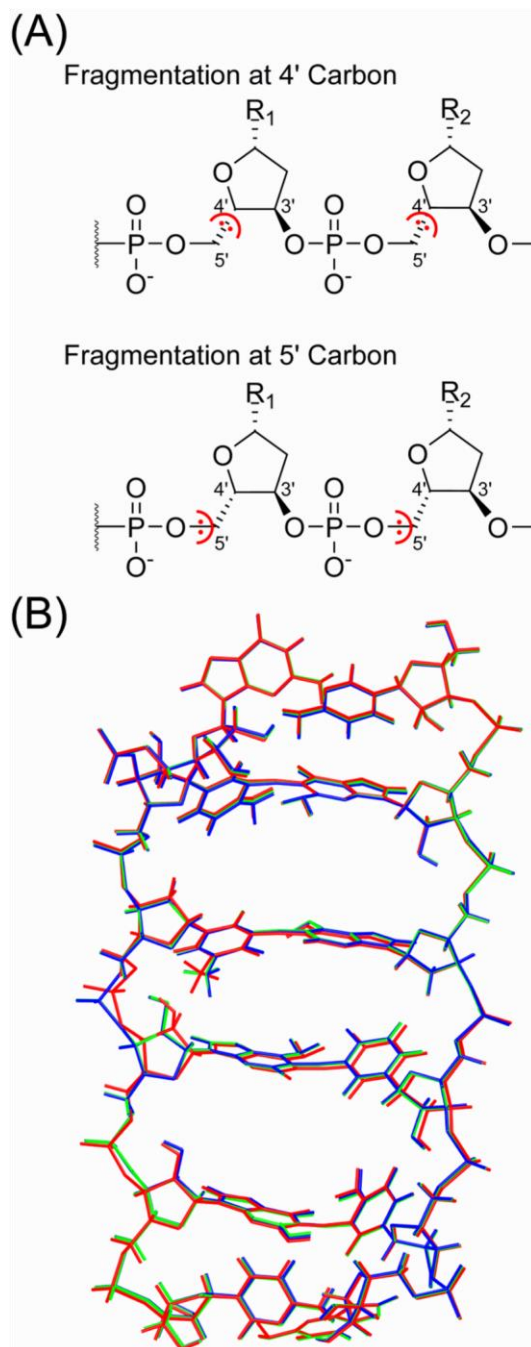


Figure 3.2. (A) Two alternative fragmentation schemes detaching C-C bonds at 4' and 5' carbon atoms, where red dots and curves show the fragment to which the detached covalent bond is assigned. (B) Overlay of the optimized structures of the CGATCG DNA. The blue, red and green lines represent the optimized structures obtained with full SCC-DFTB and FMO-DFTB with the fragmentation at 4' and 5' carbon atoms, respectively.

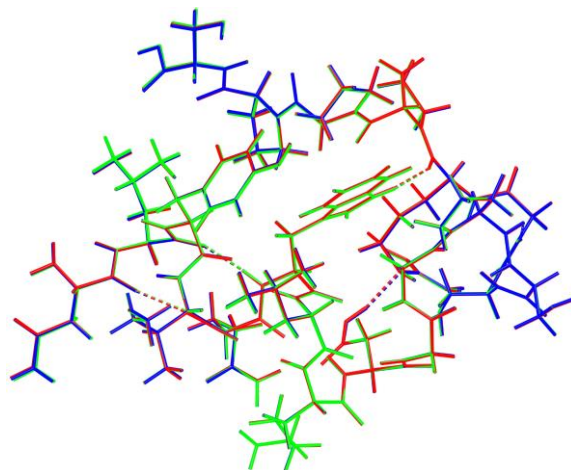


Figure 3.3. Superposition of the optimized structures of the neutralized Trp-cage protein. The blue, red and green lines are used to plot the optimized structures obtained with full SCC-DFTB and FMO-DFTB with 1 and 2 residues per fragment, respectively. The rmsd between FMO-DFTB and full SCC-DFTB was 0.067 and 0.044 Å for 1 and 2 residues per fragment, respectively. Dotted lines show hydrogen bonds.

3.3.2 Scaling of FMO-DFTB

For a comparison of timings, we performed FMO-DFTB and full SCC-DFTB calculations of water clusters, and the corresponding data is shown in Table 3. The calculation for a water cluster containing 12 288 atoms took 5.9 days for full SCC-DFTB, while FMO-DFTB took 109.7 seconds, with a speed-up factor of 4646. An extrapolation suggests that full SCCDFTB calculation will take about three weeks to finish the single point energy calculation of 18 432 atoms, whereas FMO-DFTB took only about 3 minutes.

Table 3.3. Comparison of wall-clock timings (seconds) for $(\text{H}_2\text{O})_n$ clusters calculated with full and FMO-based SCC-DFTB on 1 Xeon CPU core. The values in parentheses are extrapolated estimates.

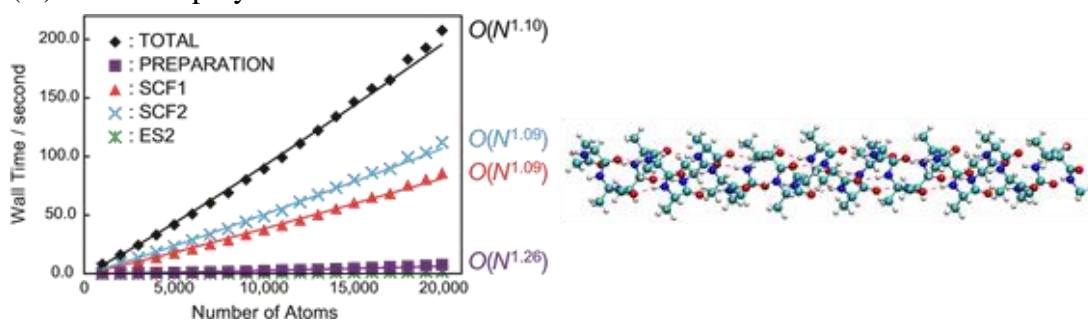
n	Full SCC-DFTB	FMO-DFTB
256	74.2	4.6
512	865.4	9.8
1024	7725.2	20.8
3072	63075.0	48.6
2048	221243.4	78.5

4096	509745.0	109.7
5120	(1030224.1)	154.1
6144	(1810687.4)	198.8
Scaling	$O(N^{3.09})$	$O(N^{1.21})$

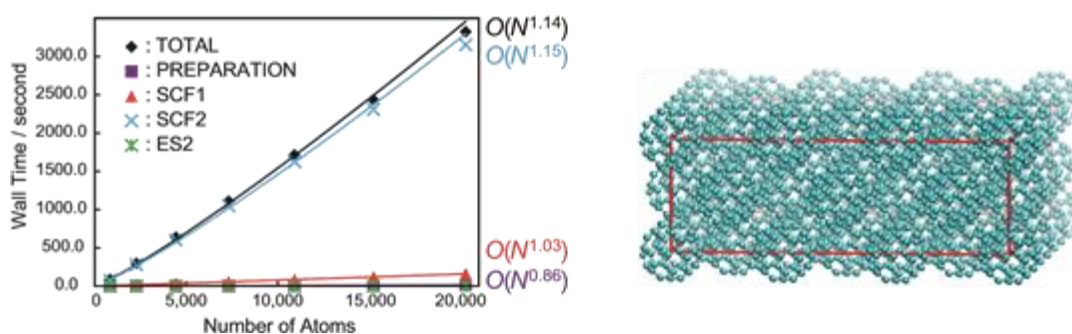
The scaling of FMO-DFTB was evaluated for the α -helix of polyalanine, fullerite slabs, and water clusters containing up to about 20 000 atoms. The fragmentation was 1 residue per fragment for polyalanine, and 1 molecule per fragment otherwise. The total wall-clock timings are shown in Figure 3.4, divided for the purpose of analysis into four steps: preparation (reading input file, processing fragmentation, etc), SCF1 (monomer SCF), SCF2 (dimer SCF), and ES2 (ES-DIM approximation).

The scaling based on the total wall-clock time of the α -helix, fullerite slab, and water cluster are $O(N^{1.10})$, $O(N^{1.14})$, and $O(N^{1.21})$, respectively. The preparation and ES2 steps do not require much time, thus the main time-consuming steps of FMO-DFTB are the calculations of monomers (SCF1) and dimers (SCF2), as in other FMO implementations. The number of monomers is N and the number of SCF dimers is proportional to N within the ES-DIM approximation. However, although the number of SCF calculations scales linearly with system size, in each of them we have to consider the ESP of the whole system. It is the inclusion of the embedding ESP that causes the increase in FMO-DFTB scaling from linear $O(N^{1.0})$ to the observed behavior of $O(N^{1.1-1.2})$. The computational bottleneck for all three examples given above was the SCF2 dimer calculation step.

(A) α -helix of polyaniline



(B) fullerite slabs



(C) water cluster

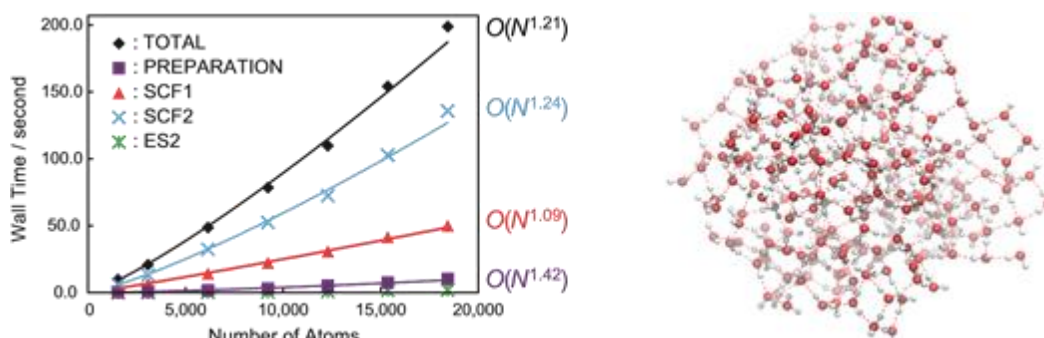


Figure 3.4. Timing of FMO-DFTB for (A) α -helices of polyaniline, (B) fullerite slabs, and (C) water cluster (in left), as measured on 1 Xeon CPU core. The representative structures of COMe-(Ala)₂₀-NHMe, 3×3 unit cells of fullerite, and (H₂O)₂₅₆ are shown on the right.

3.3.3 Parallelization of FMO-DFTB and its application to a fullerite geometry optimization

As described above, we parallelized FMO-DFTB in a fashion similar to other FMO methods, with each group of CPU cores doing a monomer or dimer calculation. In FMO-DFTB we chose to assign 1 CPU core per group. To test the parallelization efficiency, we used a fullerite slab with 40×40 unit cells, $(C_{60})_{9842}$, containing 590 520 atoms. As in the above described three benchmark systems, the computational bottleneck for the fullerite calculations was again the SCF2 dimer calculation step, and the required time for this step even more significant since each dimer contained 120 atoms. The SCF2 step took 92-95% of the total time, whereas the preparation and ES2 steps are almost negligible. We performed a single point energy calculation using 16, 32, 64, 96, and 128 CPU cores (1-8 nodes). The speed-up measured by the wall-clock time with a 1 node (16 CPU cores) calculation as reference is shown in Figure 5.

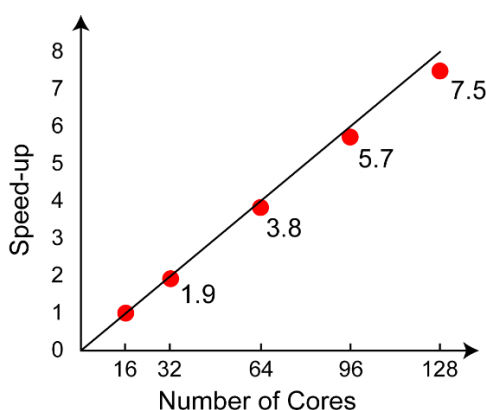


Figure 3.5. Speed-up of parallel FMO-DFTB calculations for the $(C_{60})_{9842}$ fullerite model system with respect to the number of cores are shown as red filled circles. The solid black line represents the ideal scaling with 100 % parallel efficiency.

We achieved a 7.5 time speed-up on 128 CPU cores (the parallel efficiency of 93.8 %). There is some loss of efficiency because of the load balancing and because a few steps remain sequential. In addition, there are no intergroup communications, so the deviation of the observed speed-up from the perfect results is mainly due to of the data exchange between groups, because of the large number of atoms and fragments. The data communication took 68.1 seconds for the total amount of 2.35 gigabytes of data. Table 3.4 shows the the timings for the geometry optimizations of some representative systems using our parallelized FMO-DFTB.

Table 3.4. The numbers of atom N_{AT} , fragments N , geometry steps N_{steps} and wall-clock timings T (min) for FMO-DFTB geometry optimizations, performed on 1 Xeon node (16 CPU cores) using RUNTYP=OPTFMO

	N_{AT}	N	N_{steps}	T (min)
COMe-(Ala) ₂₀ -NHMe (α -helix)	212	20	431	2.8
COMe-(Ala) ₂₀ -NHMe (β -turn)	212	20	265	1.7
COMe-(Ala) ₂₀ -NHMe (extended)	212	20	191	1.0
CGATCG DNA (fragmentation at 4' carbon)	385	12	1788	41.1
CGATCG DNA (fragmentation at 5' carbon)	385	12	2659	58.4
Trp-cage protein	303	10	675	6.98
Trp-cage protein	303	20	674	11.9

For demonstration purposes, we calculate the fullerite cluster consisting of 53×53 unit cells and containing 1 030 440 atoms. A single point calculation on 128 cores (8 nodes) took 4993 seconds (83.2 minutes). This relatively long wall-clock time is related to the fact that the fragment size is big: 60 atoms per fragment (one fullerene molecule per fragment). The equilibrium geometry of the fullerite containing over one million atoms was found in 16 steps, which took 99.4 hours on 8 Xeon nodes (128 cores). C_{60} is a nonpolar system and the interaction between fullerene molecules is governed by van der Waals forces. Thus, we repeated the geometry optimization of the fullerite system with a posteriori dispersion using FMO-DFTB-D. To accelerate geometry optimization, we constructed a new initial structure using the optimized cell length of 4×4 fullerite slab. Inclusion of dispersion interaction increased the wall-clock time by approximately 1.5 percent per geometry optimization cycle, and a minimum geometry with shorter cell length was found after 60 iterations. We found that the experimental cell length¹⁰⁰ of 14.04 Å became 13.91 and 14.02 Å with and without dispersion, respectively.

3.4 Conclusions

We have derived and implemented the combination of the density-functional tight-binding method (DFTB) with the fragment molecular orbital (FMO) method, for both SCC and NCC versions of DFTB, including a posteriori dispersion interaction. Full DFTB and FMO-DFTB methods have been implemented in GAMESS-US. We have parallelized FMO-DFTB with GDDI and demonstrated its reasonable parallel efficiency.

We have shown that the total energy of full SCC-DFTB calculations is reproduced in FMO-DFTB within 1 kcal/mol for a 2000 atom polypeptide, when the system is partitioned with fragment sizes of two or more residues. The structures optimized with FMO-DFTB had rmsd values of 0.1 Å or less, compared to the minima obtained with full SCC-DFTB. The comparison was somewhat complicated by the existence of many local minima on the corresponding potential energy surfaces, allowing FMO-DFTB and SCC-DFTB to converge to different stationary points when starting geometry optimizations from the same initial geometries. FMO-DFTB-D exactly reproduces the dispersion interaction of full DFTB-D calculations.

The computational scaling of FMO-DFTB with the number of atoms N was shown to be $O(N^{1.1-1.2})$ for 1D, 2D, as well as 3D systems, a little bit higher than the linear scaling. This is a huge improvement over the scaling of full SCC-DFTB, which is approximately cubic. The energy of a water cluster with 18 432 atoms was calculated with FMO-DFTB in about 3 minutes, whereas the corresponding full SCC-DFTB calculation is estimated to require about 3 weeks, which is about 4 orders of magnitude longer.

We have demonstrated the efficiency of FMO-DFTB by optimizing the structure of fullerite containing more than 1 million of atoms. Clearly, although purely periodic systems can be computed with periodic boundary conditions, the cluster approach is very useful for the structures with defects, doping and adsorption on the surface as well as for amorphous and other nonperiodic systems, which are very frequent in material science. In future, we plan to implement and develop the third-order DFTB,^{44,104} important for practical applications in particular in relation to biosystems. FMO has been applied to a number of biochemical¹⁰⁵ and inorganic⁶⁶⁻⁷⁰ systems,⁵⁹ although these simulations required considerable computational resources, sometimes top-class supercomputers.²⁷ With the introduction of FMO-DFTB, these simulations can be performed on small scale PC clusters or even single desktop computers, greatly increasing the accessibility of FMO to the end users.

Bibliography

- (1) Zhao, G.; Perilla, J. R.; Yufenyuy, E. L.; Meng, X.; Chen, B.; Ning, J.; Ahn, J.; Gronenborn, A. M.; Schulten, K.; Aiken, C.; Zhang, P. *Nature* **2013**, 497, 643–646.
- (2) Ufimtsev, I. S.; Luehr, N.; Martinez, T. J. *J. Chem. Theory Comput.* **2011**, 2, 1789–1793.
- (3) Sena, A. M. P.; Miyazaki, T.; Bowler, D. R. *J. Chem. Theory Comput.* **2011**, 7, 884–889.
- (4) Hirano, T.; Sato, F. *Phys. Chem. Chem. Phys.* **2014**, 16, 14496–14503.
- (5) Yang, W. *Phys. Rev. Lett.* **1991**, 66, 1438–1441.
- (6) Goedecker, S.; Scuseria, G. E. *Comp. Sci. Eng.* **2003**, 5, 14–21.

- (7) *Linear-Scaling Techniques in Computational Chemistry and Physics* ; Zalesny, R. , Papadopoulos, M. G. , Mezey, P. G. , Leszczynski, J. , Eds.; Springer: New York, 2011.
- (8) Nikitina, E.; Sulimov, V.; Zayets, V.; Zaitseva, N. *Int. J. Quantum Chem.* **2004**, *97*, 747–763.
- (9) Stewart, J. J. P. *J. Mol. Model.* **2009**, *15*, 765–805.
- (10) Gordon, M. S.; Fedorov, D. G.; Pruitt, S. R.; Slipchenko, L. V. *Chem. Rev.* **2012**, *112*, 632–672.
- (11) Otto, P.; Ladik, J. *Chem. Phys.* **1975**, *8*, 192–200.
- (12) Gao, J. J. *Phys. Chem. B* **1997**, *101*, 657–663.
- (13) Kobayashi, M.; Nakai, H. *J. Chem. Phys.* **2013**, *138*, 044102.
- (14) He, X.; Merz, K. M. *J. Chem. Theory Comput.* **2010**, *6*, 405–411.
- (15) Yu, H.; Leverentz, H. R.; Bai, P.; Siepmann, J. I.; Truhlar, D. G. *J. Phys. Chem. Lett.* **2014**, *5*, 660–670.
- (16) Tong, Y.; Mei, Y.; Zhang, J. Z. H.; Duan, L. L.; Zhang, Q. G. *J. Theor. Comp. Chem.* **2009**, *8*, 1265.
- (17) Söderhjelm, P.; Kongsted, J.; Ryde, U. *J. Chem. Theory Comput.* **2010**, *6*, 1726–1737.
- (18) Gao, J.; Wang, Y. *J. Chem. Phys.* **2012**, *136*, 071101. Collins, M. A. *Phys. Chem. Chem. Phys.* **2012**, *14*, 7744–7751.
- (19) Collins, M. A.; *Phys. Chem. Chem. Phys.* **2012**, *14*, 7744–7751.
- (20) Frank, A.; Möller, H. M.; Exner, T. E. *J. Chem. Theory Comput.* **2012**, *8*, 1480–1492.
- (21) Gordon, M. S.; Smith, Q. A.; Xu, P.; Slipchenko, L. V. *Annu. Rev. Phys. Chem.* **2013**, *64*, 553–578.
- (22) Kiewisch, K.; Jacob, C. R.; Visscher, J. *J. Chem. Theory Comput.* **2013**, *9*, 2425–2440.
- (23) Howard, J. C.; Tschumper, G. S. *J. Chem. Phys.* **2013**, *139*, 184113.
- (24) Wang, K.; Li, W.; Li, S. *J. Chem. Theory Comput.* **2014**, *10*, 1546–1553.
- (25) Sahu, N.; Yeole, S. D.; Gadre, S. R. *J. Chem. Phys.* **2013**, *138*, 104101.
- (26) Huang, L.; Massa, L. *Future Med. Chem.* **2012**, *4*, 1479–1494.
- (27) Ikegami, T. ; Ishida, T. ; Fedorov, D. G. ; Kitaura, K. ; Inadomi, Y. ; Umeda, H. ; Yokokawa, M. ; Sekiguchi, S. **2005**.
- (28) Huang, L.; Massa, L.; Karle, J. *Proc. Nat. Acad. Sci. U.S.A.* **2009**, *106*, 1731–1736.
- (29) Sawada, T.; Fedorov, D. G.; Kitaura, K. *J. Phys. Chem. B* **2010**, *114*, 15700–15705.
- (30) Ikegami, T.; Ishida, T.; Fedorov, D. G.; Kitaura, K.; Inadomi, Y.; Umeda, H.; Yokokawa, M.; Sekiguchi, S. *J. Comput. Chem.* **2010**, *31*, 447–454.
- (31) Fedorov, D. G.; Alexeev, Y.; Kitaura, K. *J. Phys. Chem. Lett.* **2011**, *2*, 282–288.

- (32) Mochizuki, Y.; Yamashita, K.; Fukuzawa, K.; Takematsu, K.; Watanabe, H.; Taguchi, N.; Okiyama, Y.; Tsuboi, M.; Nakano, T.; Tanaka, S. *Chem. Phys. Lett.* **2010**, *493*, 346–352.
- (33) Canfield, P.; Dahlbom, M. G.; Hush, N. S.; Reimers, J. R. *J. Chem. Phys.* **2006**, *124*, 024301.
- (34) Xie, W.; Orozco, M.; Truhlar, D. G.; Gao, J. *J. Chem. Theory Comput.* **2009**, *5*, 459–467.
- (35) Sato, M.; Yamataka, H.; Komeiji, Y.; Mochizuki, Y.; Ishikawa, T.; Nakano, T. *J. Am. Chem. Soc.* **2008**, *130*, 2396–2397.
- (36) Frauenheim, T.; Seifert, G.; Elstner, M.; Niehaus, T.; Kohler, C.; Amkreutz, M.; Sternberg, M.; Hajnal, Z.; Carlo, A. D.; Suhai, S. *J. Phys.: Cond. Matter* **2002**, *14*, 3015–3047.
- (37) Gaus, M.; Cui, Q.; Elstner, M. *WIREs Comput. Mol. Sci.* **2014**, *4*, 49–61.
- (38) Koskinen, P.; Mäkinen, V. *Comput. Mater. Sci.* **2009**, *47*, 237–253.
- (39) Oliveira, A. F.; Seifert, G.; Heine, T.; Duarte, H. A. *J. Braz. Chem. Soc.* **2009**, *20*, 1193–1205.
- (40) Seifert, G.; Joswig, J.-O. *WIREs Comput. Mol. Sci.* **2014**, *2*, 456–465.
- (41) Hohenberg, P.; Kohn, W. *Phys. Rev.* **1964**, *136*, B864–B871.
- (42) Kohn, W.; Sham, L. *J. Phys. Rev.* **1965**, *140*, A1133–A1138.
- (43) Elstner, M.; Porezag, D.; Jungnickel, G.; Elsner, J.; Haugk, M.; Frauenheim, T.; Suhai, S.; Seifert, G. *Phys. Rev. B* **1998**, *58*, 7260–7268.
- (44) Gaus, M.; Cui, Q.; Elstner, M. *J. Chem. Theory Comput.* **2011**, *7*, 931–948.
- (45) Finnis, M. W.; Paxton, A. T.; Methfessel, M.; van Schilfgaarde, M. *Phys. Rev. Lett.* **1998**, *81*, 5149–5152.
- (46) Sankey, O. F.; Demkov, A. A.; Windl, W.; Fritsch, J. H.; Lewis, J. P.; Fuentes-Cabrera, M. *Int. J. Quantum Chem.* **1998**, *69*, 327–340.
- (47) Foulkes, W. M. C.; Haydock, R. *Phys. Rev. B* **1989**, *39*, 12520–12536.
- (48) Porezag, D.; Frauenheim, T.; Köhler, T.; Seifert, G.; Kaschner, R. *Phys. Rev. B* **1995**, *51*, 12947–12957.
- (49) Hu, H.; Lu, Z.; Elstner, M.; Hermans, J.; Yang, W. *J. Phys. Chem. A* **2007**, *111*, 5685–5691.
- (50) Giese, T. J.; Chen, H.; Dissanayake, T.; Giambau, G. M.; Heldenbrando, H.; Huang, M.; Kuechler, E. R.; Lee, T.-S.; Panteva, M. T.; Radak, B. K.; York, D. M. *J. Chem. Theory Comput.* **2013**, *9*, 1417–1427.
- (51) Cawkwell, M. J.; Niklasson, A. M. N. *J. Chem. Phys.* **2012**, *137*, 134105.
- (52) Elstner, M.; Hobza, P.; Frauenheim, T.; Suhai, S.; Kaxiras, E. *J. Chem. Phys.* **2001**, *114*, 5149–5155.

- (53) Grimme, S. *J. Comput. Chem.* **2006**, *27*, 1787–1799.
- (54) Rappé, A. K.; Casewit, C. J.; Colwell, K. S.; Goddard, W. A., III; Skiff, W. M. *J. Am. Chem. Soc.* **1992**, *114*, 10024–10035.
- (55) Kitaura, K.; Ikeo, E.; Asada, T.; Nakano, T.; Uebayasi, M. *Chem. Phys. Lett.* **1999**, *313*, 701–706.
- (56) *The Fragment Molecular Orbital Method: Practical Applications to Large Molecular Systems*; Fedorov, D. G., Kitaura, K., Eds.; CRC Press: Boca Raton, FL, 2009.
- (57) Fedorov, D. G.; Kitaura, K. *J. Phys. Chem. A* **2007**, *111*, 6904–6914.
- (58) Fedorov, D. G.; Nagata, T.; Kitaura, K. *Phys. Chem. Chem. Phys.* **2012**, *14*, 7562–7577.
- (59) Tanaka, S.; Mochizuki, Y.; Komeiji, Y.; Okiyama, Y.; Fukuzawa, K. *Phys. Chem. Chem. Phys.* **2014**, *16*, 10310–10344.
- (60) Mazanetz, M. P.; Ichihara, O.; Law, R. J.; Whittaker, M. *J. Cheminf.* 2011, *3*, 2.
- (61) Sawada, T.; Fedorov, D. G.; Kitaura, K. *J. Am. Chem. Soc.* **2010**, *132*, 16862–16872.
- (62) Watanabe, T.; Inadomi, Y.; Fukuzawa, K.; Nakano, T.; Tanaka, S.; Nilsson, L.; Nagashima, U. *J. Phys. Chem. B* **2007**, *111*, 9621–9627.
- (63) Fukuzawa, K.; Komeiji, Y.; Mochizuki, Y.; Kato, A.; Nakano, T.; Tanaka, S. *J. Comput. Chem.* **2006**, *27*, 948–960.
- (64) Fukuzawa, K.; Watanabe, C.; Kurisaki, I.; Taguchi, N.; Mochizuki, Y.; Nakano, T.; Tanaka, S.; Komeiji, Y. *Comp. Theor. Chem.* **2014**, *1034*, 7–16.
- (65) Nakata, H.; Fedorov, D. G.; Yokojima, S.; Kitaura, K.; Nakamura, S. *Theor. Chem. Acc.* **2014**, *133*, 1477.
- (66) Fedorov, D. G.; Avramov, P. V.; Jensen, J. H.; Kitaura, K. *Chem. Phys. Lett.* **2009**, *477*, 169–175.
- (67) Carlson, P. J.; Bose, S.; Armstrong, D. W.; Hawkins, T.; Gordon, M. S.; Petrich, J. W. *J. Phys. Chem. B* **2012**, *116*, 503–512.
- (68) Avramov, P. V.; Fedorov, D. G.; Sorokin, P. B.; Sakai, S.; Entani, S.; Ohtomo, M.; Y. Matsumoto, H. N. *J. Phys. Chem. Lett.* **2012**, *3*, 2003–2008.
- (69) Okiyama, Y.; Tsukamoto, T.; Watanabe, C.; Fukuzawa, K.; Tanaka, S.; Mochizuki, Y. *Chem. Phys. Lett.* **2013**, *566*, 25–31.
- (70) Roskop, L.; Fedorov, D. G.; Gordon, M. S. *Mol. Phys.* **2013**, *111*, 1622–1629.
- (71) Sugiki, S.-I.; Kurita, N.; Sengoku, Y.; Sekino, H. *Chem. Phys. Lett.* **2003**, *382*, 611–617.
- (72) Fedorov, D. G.; Kitaura, K. *Chem. Phys. Lett.* **2004**, *389*, 129–134.
- (73) Chiba, M.; Fedorov, D. G.; Kitaura, K. *Chem. Phys. Lett.* **2007**, *444*, 346–350.
- (74) Nakata, H.; Fedorov, D. G.; Yokojima, S.; Kitaura, K.; Nakamura, S. *Theor. Chem. Acc.* **2014**, *133*, 1477.
- (75) Fedorov, D. G.; Kitaura, K. *Chem. Phys. Lett.* **2014**, *597*, 99–105.

- (76)Fedorov, D. G.; Kitaura, K. *J. Chem. Phys.* **2004**, *120*, 6832–6840.
- (77)Nakano, T.; Mochizuki, Y.; Yamashita, K.; Watanabe, C.; Fukuzawa, K.; Segawa, K.; Okiyama, Y.; Tsukamoto, T.; Tanaka, S. *Chem. Phys. Lett.* **2012**, *523*, 128–133.
- (78)Seifert, G.; Porezag, D.; Frauenheim, T. *Int. J. Quantum Chem.* **1996**, *58*, 185–192.
- (79)Frauenheim, T.; Weich, F.; Köhler, T.; Uhlmann, S.; Porezag, D.; Seifert, G. *Phys. Rev. B* **1995**, *52*, 11492–11501.
- (80)Haugk, M.; Elsner, J.; Frauenheim, T. *J. Phys.: Condens. Matter* **1997**, *9*, 7305–7315.
- (81)Zheng, G.; Irle, S.; Morokuma, K. *Chem. Phys. Lett.* **2005**, *412*, 210–216.
- (82)Irle, S.; Zheng, G.; Wang, Z.; Morokuma, K. *J. Phys. Chem. B* **2006**, *110*, 14531–14545.
- (83)Nishimoto, Y.; Wang, Z.; Morokuma, K.; Irle, S. *Phys. Status Solidi B* **2012**, *249*, 324–334.
- (84)Parr, R. G.; Pearson, R. G. *J. Am. Chem. Soc.* **1983**, *105*, 7512–7516.
- (85)Kaminski, S.; Gaus, M.; Elstner, M. *J. Phys. Chem. A* **2012**, *116*, 11927–11937.
- (86)Nakano, T.; Kaminuma, T.; Sato, T.; Fukuzawa, K.; Akiyama, Y.; Uebayasi, M.; Kitaura, K. *Chem. Phys. Lett.* **2002**, *351*, 475–480.
- (87)Nakano, T.; Kaminuma, T.; Sato, T.; Akiyama, Y.; Uebayasi, M.; Kitaura, K. *Chem. Phys. Lett.* **2000**, *318*, 614–618.
- (88)Nagata, T.; Fedorov, D. G.; Kitaura, K. *Chem. Phys. Lett.* **2010**, *492*, 302–308.
- (89)Zhechkov, L.; Heine, T.; Patchkovskii, S.; Seifert, G.; Duarte, H. A. *J. Chem. Theory Comput.* **2005**, *1*, 841–847.
- (90)Schmidt, N. W.; Baldridge, K. K.; Baldridge, J. A.; Boatz, J. A.; Elbert, S. T.; Gordon, M. S.; Jensen, J. J.; Koseki, S.; Matsunaga, N.; Nguyen, K. A.; Su, S.; Windus, T. L.; Dupuis, M.; Montgomery, J. A. *J. Comput. Chem.* **1993**, *14*, 1347–1363.
- (91)Johnson, D. D. *Phys. Rev. B* **1998**, *38*, 12807–12813.
- (92)Fedorov, D. G.; Olson, R. M.; Kitaura, K.; Gordon, M. S.; Koseki, S. *J. Comput. Chem.* **2004**, *25*, 872–880.
- (93)Frenzel, J. ; Oliveira, A. F. ; Jardillier, N. ; Heine, T. ; Seifert, G. Semi-relativistic, self-consistent charge Slater–Koster tables for density-functional based tight-binding (DFTB) for materials science simulations. TU-Dresden; 2004–2009.
- (94)<http://www.dftb.org/>.
- (95)Pipek, J.; Mezey, P. G. *J. Chem. Phys.* **1989**, *90*, 4916–4926.
- (96)Dennington, R. ; Keith, T. ; Millam, J. *GaussView Version 5*; Semichem Inc.: Shawnee Mission, KS, 2009.
- (97)Ponder, J.W. *TINKER: Software Tools forMolecular Design, 6.0*; Washington University School of Medicine: Saint Louis, MO, 2009.
- (98)Wang, J.; Cieplak, P.; Kollman, P. A. *J. Comput. Chem.* **2000**, *21*, 1049–1074.

- (99) Fedorov, D. G.; Ishida, T.; Uebayasi, M.; Kitaura, K. *J. Phys. Chem. A* **2007**, *111*, 2722–2732.
- (100) Brazhkin, V. V.; Lyapin, A. G.; Popova, S. V.; Voloshin, R. N.; Antonov, Y. V.; Lyapin, S. G.; Kluev, Y. A.; Naletov, A. M.; Mel'nik, N. N. *Phys. Rev. B* **1997**, *56*, 11465–11471.
- (101) Fedorov, D. G.; Slipchenko, L. V.; Kitaura, K. *J. Phys. Chem. A* **2010**, *114*, 8742–8753.
- (102) Li, H.; Fedorov, D. G.; Nagata, T.; Kitaura, K.; Jensen, J. H.; Gordon, M. S. *J. Comput. Chem.* **2010**, *31*, 778–790.
- (103) Nakata, H.; Nagata, T.; Fedorov, D. G.; Yokojima, S.; Kitaura, K.; Nakamura, S. *J. Chem. Phys.* **2013**, *138*, 164103.
- (104) Yang, Y.; Yu, H.; York, D.; Cui, Q.; Elstner, M. *J. Phys. Chem. A* **2007**, *111*, 10861–10873.
- (105) Alexeev, Y.; Mazanetz, M. P.; Ichihara, O.; Fedorov, D. G. *Curr. Top. Med. Chem.* **2012**, *12*, 2013–2033.

Chapter 4

Simulation of Vibrational Spectra of Large Molecular Systems with Radical or Metallic Electronic Structure

4.1 Introduction

Spectroscopic measurement, such as infrared (IR) and Raman spectroscopy,¹⁻³ is of particular importance in identifying structures and properties of nanostructures.^{4,5} In the history of nanostructures for example, the IR spectra of graphitic soot by Krätschmer et al.⁶ delivered strong experimental evidence for the presence of buckminsterfullerene C₆₀ in 1990. One of the first quantum chemical IR and Raman simulations for C₆₀ was performed by Giannozzi et al.⁷ using density-functional perturbation theory (DFPT)⁸ in 1994. On the other hand, graphene and certain carbon nanotubes are semi-metallic and metallic systems, respectively,⁴ complicating the theoretical simulation of their vibrational spectra.

It is a general difficulty for quantum chemical methods utilizing atomic orbital (AO) basis sets to tackle multiradical or metallic systems, because standard self-consistent-field (SCF) calculations cannot converge a stable electron configuration. Unstable SCF calculation for nearly-degenerated system is attributed to the fact that integer occupation of orbitals creates so strong potential that the electronic structure determined previously is upset by the potential newly generated. Although multi-reference methods, such as the density-matrix renormalization group (DMRG) method,⁹ are very powerful, they are computationally highly demanding. A more practical solution for extended molecular systems is to utilize fractional occupation numbers (FONs)¹⁰⁻¹² for the open-shell molecular orbitals (MOs). The concept of FONs was originally introduced by Mermin¹³ in 1965 to extend density functional theory (DFT) to an inhomogeneous electron gas at nonzero temperatures, and pictorially corresponds to using a smooth function in determining occupation numbers of MOs allowing fractionally occupied orbitals, while keeping the number of electrons in the system constant. This prevents orbitals from inter-conversion during SCF calculation and furthermore accelerates SCF convergence in ab initio calculations.¹⁴ One application study¹⁵ showed that DFT calculation with FONs improved the description of restricted DFT for multi-reference systems such as linear acenes, agreeing with an expensive multi-reference method.¹⁶ In spite of potentially useful features of FONs, the second-order geometrical derivative with FONs has not been developed yet, therefore spectroscopic investigations of large open-shell molecular systems in this line has been stayed clear of up to date.

4.2 Methodology

Here, we derive analytical second-order geometrical derivatives of free energy function for self-consistent charge density-functional tight-binding (DFTB2) method¹⁷⁻²² with FONs. Although the previous second-order derivative implementation by Witek et al.²³ limited their study to closed shell systems, our extension is in principle applicable for any restricted wave functions. The second-order derivative of free energy (\mathcal{E}) with respect to the displacement of nuclei a and b with FONs needs only one additional term to that of internal energy (E) with integer occupation numbers:

$$\frac{\partial^2 \mathcal{E}}{\partial a \partial b} = \frac{\partial^2 E}{\partial a \partial b} + 2 \sum_i^{\text{MO}} \frac{\partial f_i}{\partial b} \sum_{\mu\nu}^{\text{AO}} c_{\mu i} c_{\nu i} \left\{ \frac{\partial H_{\mu\nu}^0}{\partial a} + (\Omega_{AB} - \varepsilon_i) \frac{\partial S_{\mu\nu}}{\partial a} \right\} \quad (4.1)$$

where f_i ($0 < f_i < 1$) represents FON of i -th MO which consists of linear combination of AOs multiplied by $c_{\mu i}$. $H_{\mu\nu}^0$ and $S_{\mu\nu}$ is the zeroth order Hamiltonian and overlap matrix element in AO basis, and Ω_{AB} is the shift contribution of Coulomb interaction in the system. f_i is determined by the orbital energies (ε_i) and electronic temperature (T_e) following the Fermi-Dirac distribution function,^{24,25}

$$f_i = \left(1 + \exp \left(\frac{\varepsilon_i - \varepsilon_F}{kT_e} \right) \right)^{-1}, \quad (4.2)$$

where ε_F is the Fermi level, determined to keep the number of electrons in the system constant, and k is the Boltzmann constant. As shown for density functional theory (DFT) with localized Gaussian-type orbitals,²⁶ the derivative of FONs disappears in the first-order derivative of free energy, therefore only the first-order derivative of FONs is needed in the second-order derivative, as in eq (4.1). As this fact is true for DFT, we believe that our concept is applicable for other methods easily by small modifications. We restrict ourselves in the case with the Fermi-Dirac distribution function, which makes the free energy function variational and the first-order derivative simple. We summarize all the details in Appendix A.

Our implementation uses as many analytically differentiated expressions as possible, therefore calculated Hessian matrix is more robust than the previous implementation which uses many numerically differentiated expressions.²³ Besides FONs, restricted spin-polarized calculation with certain singly occupied MOs can be mimicked at zero electronic temperature. In that case, since the occupation numbers of doubly and singly occupied MOs are fixed, the additional term of eq. (4.1) is no longer needed. It should be noted that the wave function derived in this way is different from the restricted open-shell (RO) wave function.²⁷ The RO wave function allows different numbers of electrons for each α and β orbital space, however our restricted wave function forces the number of electrons for both orbital space same.

Our methodology requires the diagonalization of Hamiltonian matrix with incomplete Slater-type orbitals. This is different from previous first-order derivative research with plane wave^{28,29} or recursive update algorithm of Fock matrix.³⁰ Although it has been pointed out that a method with diagonalization is computationally demanding,³⁰ our methodology is well suited for studies of large systems since DFTB itself is computationally very efficient,²¹⁻²³ and therefore our development will be a powerful tool for the simulation of vibrational spectra of large systems.

4.3 Results and Discussions

4.3.1 Benchmark Calculation with Nitronyl Nitroxide Radicals

We next investigate the applicability of DFTB for nitronyl nitroxide (N-O) radical systems. Conceptually, the orbital occupation of singly occupied molecular orbital (SOMO) is be one, regardless of geometry. Since we requires the SOMO to be always singly occupied, the contribution of the second term in eq (4.1) is zero, therefore underlying theory remains same to the one for closed shell system.²³ Nevertheless, our calculation is the first simulation of IR spectra of radical system with analytical second-order derivative of DFTB as far as our knowledge reaches, and is worth challenging. We selected 21 N-O radical stretching modes listed in ref 31 where experimental frequencies are available and compared them with those calculated at unrestricted B3LYP/6-311++G(d,p) (UB3LYP) and DFTB using mio and slkoopt³² parameter sets. Since B3LYP overestimates vibrational frequencies,³³ we scaled all wavenumbers by a factor of 0.976, following the previous computational work by Rintoul et al.³¹ In the case of DFTB, we also scaled them by a factor of 0.952 and 0.959 determined so as to minimize each root mean square (RMS) deviation. We show the unscaled and scaled RMS and maximum deviations in Table 4.1.

Table 4.1. Comparison of root mean square (RMS) and maximum deviations (unit in cm^{-1}) from experimental N-O radical stretching modes at scaled and unscaled UB3LYP/6-311++G(d,p) and DFTB with mio and slkoopt parameter sets.

method	scaling factor	RMS deviation	max deviation
B3LYP	1.000	49.35	102.84
	0.976	28.10	67.56
mio	1.000	79.45	134.60
	0.952	38.43	125.21
slkoopt	1.000	68.85	129.19

Table 4.1 shows that the UB3LYP calculation predicts in a better accuracy than DFTB using both parameter sets. The RMS deviation of scaled UB3LYP result is similar as the previous work at B3LYP/6-31G(d) by Scott et al.³⁴ (34 cm⁻¹) and is 28.10 cm⁻¹. Maximum deviation of 67.56 cm⁻¹ is also satisfactory small, compared to the previous work.³⁴ On the other hand, unscaled DFTB gives larger deviation, and RMS deviations of mio and slkoopt are as high as 79.45 and 68.85 cm⁻¹. However, unlike DFT, DFTB is a semi-empirical method whose accuracy largely depends on the quality of parameters, therefore our numerical results strongly indicate that there is a plenty of room for parameterization. Scaling vibrational frequency is one of parameterization techniques, although the previous work focusing on typical molecules³⁵ concluded that scaling of SCC-DFTB frequencies does not improve much. In our case, however, scaling of DFTB wavenumbers by a factor of 0.952 (mio) and 0.959 (slkoopt) reduced the RMS deviations by 50 %, whereas UB3LYP by 0.976 does by 40 %. The RMS deviation of 34.15 cm⁻¹ using slkoopt parameter set with a scaling factor of 0.959 differs from B3LYP value by only 6.07 cm⁻¹. This result is an encouraging result, considering that our slkoopt parameter set does not include improved parameters for N-O interaction.³² We conclude our comparison here by mentioning that inclusion of spin-spin interaction does not dramatically improve DFTB frequencies. Numerical derivative with unrestricted DFTB for selected molecules improves only a few cm⁻¹. All structures and vibrational frequencies of N-O radical stretching mode are given in Appendix B.

5.3.2 Theoretical IR and Raman Spectra of Polyanulene

As a practical application for extended open-shell molecular system, we tested our method for the evolution of IR and Raman spectra of zigzag-type graphene nanoribbon (ZGNR)^{4,36,37} which consists of three rows of benzene ring with increasing the number of units (Figure 4.1). We changed the number of units from one (22 atoms) to twenty (212 atoms) systematically and set $T_e = 100$ K. The work by Luo et al.³⁸ changed the height of GNR while the width of GNR was infinite with periodic boundary condition, however we treated GNR as a molecular cluster and changed the width while keeping the height constant. The IR intensity spectra (Figure 4.2 (A)) show that there is a characteristic evolution of the strong IR intensity at around 3030 and 3040 cm⁻¹. These peaks correspond to the symmetric and antisymmetric C-H stretching at the terminals of elongating direction. This is clearly an artificial edge-effect because of our finite length model, and therefore such a strong peak has not been predicted in the previous work by Luo et al.³⁸ If we compare the relative intensity of these C-H stretching modes against the second highest peak at 750 to 800 cm⁻¹ which comes from synchronous out-

of-plane C-H wagging mode at zigzag edge, it increases gradually from 2.07 ($n = 2$) to 4.39 ($n = 20$). The IR intensity is calculated by the projection of derivatives of dipole moment onto each normal mode. Because the vibrational vectors of the terminal C-H stretching hardly change, the growth of relative intensity of C-H stretching should come from the growth of derivatives of dipole moment. As calculations of vibrational frequency require immense computational effort with QM methods,³⁹ discussions about the relation between relative intensity and derivatives of dipole moment for large open-shell systems are limited. As a qualitative explanation, small displacement of edge hydrogen atom induces gradient of potential along the elongating direction of ZGNR. Although the gradient may be small, the length of potential becomes longer as the number of units increases. Furthermore, the contribution of each atom to dipole moment increases as the distance from the arbitrary center increases, therefore derivatives of dipole moment of extended systems tends to be high.

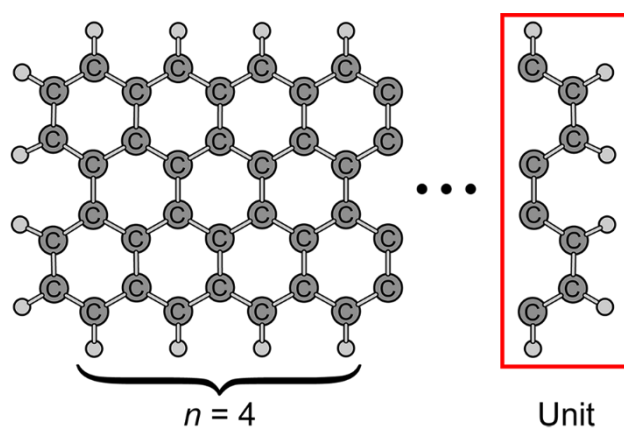


Figure 4.1. Definition of zigzag-type graphene nanoribbon ($n = 4$) and single unit boxed by red line. Gray spheres represent hydrogen atoms.

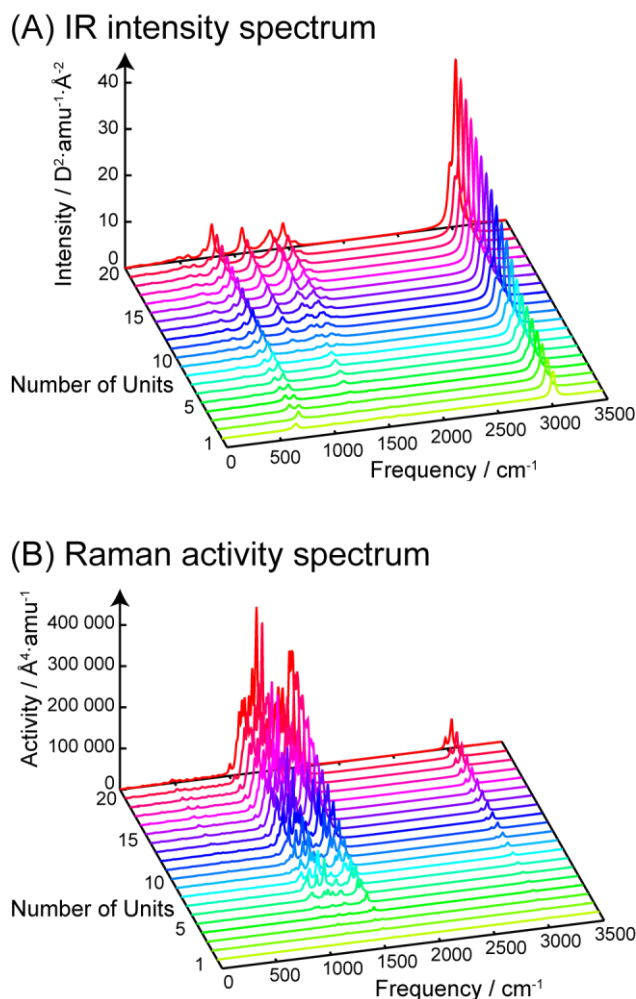


Figure 4.2. Evolution of (A) IR intensity and (B) Raman activity spectra of ZGNR at DFTB with slkoopt parameter set with increasing the number of units.

The Raman activity spectra (Figure 4.2 (B)) show that our strongest D and G band-like peak appears at 1213.46 and 1574.37 cm^{-1} ($n = 20$; see Supporting Information). The experimental D and G band of mono-layer graphene⁴⁰ is observed at around 1350 and 1580 cm^{-1} , so our result well agrees with the experimental G band. On the other hand, there is a large discrepancy of the position of D band and its relative intensity. Our vibrational mode of the highest peak of D band localizes at the terminals of elongating direction, therefore this is again an edge-effect. Our model system is too small to compare experiment, so follow-up study is now in progress.

4.3.3 Computational Timings of Numerical and Analytical Second Derivatives

We finally compare the wall-clock time of analytical and numerical (step size = 1.0×10^{-4} a.u.) second-order derivatives with increasing the size of ZGNR discussed in the previous paragraph, as shown in Figure 4.3. Our scaling behavior indicates that analytical second-

order derivative is marginally faster than numerical one. The trend lines fitted with $t = a \times n^b$ function corresponds to $t = 0.022n^{3.88}$ and $0.220n^{3.60}$ for analytical and numerical differentiation at $T_e = 100$ K respectively, therefore our analytical differentiation is around ten times more efficient than the numerical one. Once the electronic temperature is raised to 5,000 K, wall-clock time of analytical and numerical derivatives increased and decreased respectively, because the dimension of coupled perturbed DFTB becomes bigger with higher electronic temperature in analytical derivative, while SCF convergence is accelerated¹⁴ in numerical differentiation. The trend line now corresponds to $t = 0.041n^{3.78}$ and $0.136n^{3.89}$ for analytical and numerical differentiation at $T_e = 5,000$ K respectively. Even at higher electronic temperature, analytical derivative is certainly computationally less demanding.

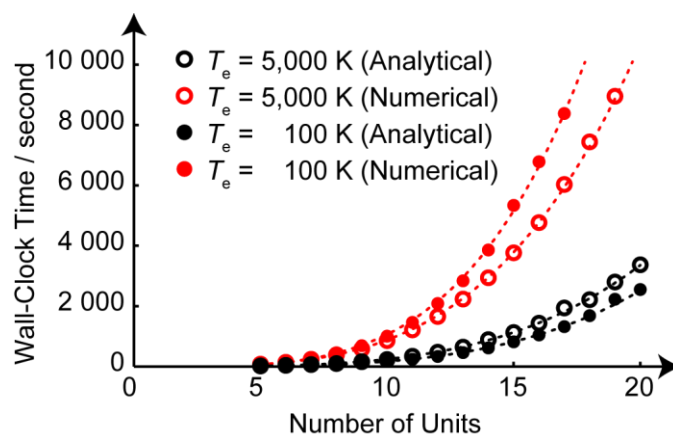


Figure 4.3. Scaling of wall-clock time for analytical and numerical second-order derivatives at $T_e = 100$ and 5,000 K for ZGNRs against the number of units.

4.4 Conclusions

In summary, we derived and implemented the second-order geometrical derivative of free energy function for DFTB2 with FONs, which is readily applicable for large open-shell molecular systems. Our benchmark calculation for N-O radical stretching modes indicates that the prediction by DFTB with an appropriate scaling factor is almost compatible with the moderately high level DFT calculation (B3LYP/6-311++G(d,p)). Our application for ZGNRs indicates that it is need to work on larger GNRs in future. We are investigating the evolution of IR and Raman spectra with increasing the number of units and with widening the width of GNRs utilizing our analytical second-order derivative, showing that our program is manageable more than 3,000 basis functions. Our approach is also promising for non-periodic large delocalized or open-shell molecular systems, such as fullerene and defected nanomaterials,⁴¹ too.

Computational Details

We implemented DFTB with energy and analytical first- and second-order geometrical derivatives into the development version of GAMESS software package.⁴² SCF density convergence criterion was 10^{-9} for numerical derivatives and 10^{-12} for any other computations, and all structures were optimized with maximum and RMS gradient elements of less than 10^{-9} and $10^{-9}/3$. We defined two parameter sets: “mio” (mio-0-1)²⁰ parameter set which was available from the DFTB web site, and another set, called “slkoopt” here, contains the optimized parameters by Makolepsza et al.³² for C-C, C-H, H-C, and H-H element pairs, although other pairs remain same to the mio set. “halorg-0-1” parameters⁴³ are used for two N-O radical molecules which contain either F or Br. In analytical second-order derivative calculations, $10^{-10} < 2f_i < 2 \cdot 10^{-10}$ was defined as fractionally occupied orbitals. The convergence of coupled-perturbed DFTB equations was reached when the maximum difference of the derivatives of Mulliken population between two consecutive cycles became less than 10^{-6} . Tightening these thresholds did not change results qualitatively. Raman activities were computed by calculating the second-order derivative of atomic forces with respect to finite electric field⁴⁴ of 0.002 a.u. Each IR and Raman peak was convoluted with the Lorentzian function with a 20 cm^{-1} line width. See Supporting Information for the details of DFT calculations.

We used Gaussian 09 Revision C.01⁴⁵ for all DFT calculations. Structures are first optimized at B3LYP⁴⁶/6-311+G(d) using unrestricted wave function, and successively re-optimized at U-B3LYP/6-311++G(d,p), to save computational cost. Default parameters are used for self-consistent-field (SCF) convergence, geometry optimization, and integral accuracy. Calculated vibrational frequencies at U-B3LYP/6-311++G(d,p) are scaled by a factor of 0.976 as in ref 31.

Bibliography

- (1) Wilson, E. B.; Decius, J. C.; Cross, P. C.; *Molecular Vibrations*; Dover Publications, Inc.: New York, 1955.
- (2) Li, Z. Q.; Henriksen, E. A.; Jiang, Z.; Hao, Z.; Martin, M. C.; Kim, P.; Stormer, H. L.; Basov, D. N. Dirac Charge Dynamics in Graphene by Infrared Spectroscopy. *Nat. Phys.* **2008**, *4*, 532-535.
- (3) *Raman Spectroscopy for Nanomaterials Characterization*; Kumar, C. S. S. R., Ed.; Springer – Verlag: Berlin, 2012.
- (4) *Chemistry of Nanocarbons*; Akasaka, T., Wudl, F., Nagase, S., Eds.; John Wiley & Sons, Ltd. Publication: Chichester, U.K., 2010.

- (5) Reichenbacher, M.; Popp, J.; *Challenges in Molecular Structure Determination*; Springer – Verlag: Berlin, 2012.
- (6) Krätschmer, W.; Fostiropoulos, K.; Huffman, D. R. The Infrared and Ultraviolet Absorption Spectra of Laboratory-Produced Carbon Dust: Evidence for the Presence of the C₆₀ Molecule *Chem. Phys. Lett.* **1990**, *170*, 167-170.
- (7) Giannozzi, P.; Baroni, S. Vibrational and Dielectric Properties of C₆₀ from Density-Functional Perturbation Theory. *J. Chem. Phys.* **1994**, *100*, 8537-8539.
- (8) Baroni, S.; de Gironcoli, S.; Dal Corso, A.; Giannozzi, P. Phonons and Related Crystal Properties from Density-Functional Perturbation Theory. *Rev. Mod. Phys.* **2001**, *73*, 515-562.
- (9) Schollwöck, U. The Density-Matrix Renormalization Group. *Rev. Mod. Phys.* **2005**, *77*, 259-314.
- (10) Slater, J. C.; Mann, J. B.; Wilson, T. M.; Wood, J. H. Nonintegral Occupation Numbers in Transition Atoms in Crystals. *Phys. Rev.* **1969**, *184*, 672-694.
- (11) Brandi, H. S.; de Matos, M. M.; Ferreira, R. Fractional Occupation in the Hartree-Fock Method. *Chem. Phys. Lett.* **1980**, *73*, 597-601.
- (12) Nesbet, R. K. Fractional Occupation Numbers in Density-Functional Theory. *Phys. Rev. A* **1997**, *56*, 2665-2669.
- (13) Mermin, N. D. Thermal Properties of the Inhomogeneous Electron Gas. *Phys. Rev.* **1965**, *137*, A1441-A1443.
- (14) Rabuck, A. D.; Scuseria G. E. Improving Self-Consistent Field Convergence by Varying Occupation Numbers. *J. Chem. Phys.* **1999**, *110*, 695.
- (15) Chai, J.-D. Density Functional Theory with Fractional Orbital Occupations. *J. Chem. Phys.* **2012**, *136*, 154104.
- (16) Hachmann, J.; Dorando, J. J.; Aviles, M.; Chan, G. K-L. The Radical Character of the Acenes: A Density Matrix Renormalization Group Study. *J. Chem. Phys.* **2007**, *127*, 134309.
- (17) Porezag, D.; Frauenheim, T.; Köhler, T.; Seifert, G.; Kaschner, R. Construction of Tight-Binding-Like Potentials on the Basis of Density-Functional Theory: Application to Carbon. *Phys. Rev. B* **1995**, *51*, 12947-12957.
- (18) Seifert, G.; Porezag, D.; Frauenheim, T. Calculations of Molecules, Clusters, and Solids with a Simplified LCAO-DFT-LDA Scheme. *Int. J. Quantum Chem.* **1996**, *58*, 185-192.
- (19) Elstner, M.; Porezag, D.; Jungnickel, G.; Elsner, J.; Haugk, M.; Trauenheim, Th.; Suhai, S.; Seifert, G. Self-Consistent-Charge Density-Functional Tight-Binding

- Method for Simulations of Complex Materials Properties. *Phys. Rev. B* **1998**, 58, 7260-7268.
- (20) Koskinen, P.; Mäkinen, V. Density-Functional Tight-Binding for Beginners. *Comput. Mater. Sci.* **2009**, 47, 237-253.
- (21) Seifert, G.; Joswig, J.-O. Density-Functional Tight-Binding – An Approximate Density-Functional Theory Method. *WIREs Comput. Mol. Sci.* **2012**, 2, 456-465.
- (22) Gaus, M.; Cui, Q.; Elstner, M. Density Functional Tight Binding: Application to Organic and Biological Molecules. *WIREs Comput. Mol. Sci.* **2014**, 4, 49-61.
- (23) Witek, H. A.; Irlé, S.; Morokuma, K. Analytical Second-Order Geometrical Derivatives of Energy for the Self-Consistent-Charge Density-Functional Tight-Binding Method. *J. Chem. Phys.* **2004**, 121, 5163-5170.
- (24) Fermi, E. Sulla Quantizzazione del Gas Perfetto Monoatomico. *Redn. Lincei* **1926**, 3, 145-149.
- (25) Dirac, P. A. M. On the Theory of Quantum Mechanics. *Proc. R. Soc. Lond. A* **1926**, 112, 661-677.
- (26) Warren, R. W.; Dunlap, B. I. Fractional Occupation Numbers and Density Functional Energy Gradients within the Linear Combination of Gaussian-Type Orbitals Approach. *Chem. Phys. Lett.* **1996**, 262, 384-392.
- (27) Roothaan, C. C. Self-Consistent Field Theory for Open Shells of Electronic Systems. *Rev. Mod. Phys.* **1960**, 32, 179-185.
- (28) Weinert, M.; Davenport, J. W. Fractional Occupations and Density-Functional Energies and Forces. *Phys. Rev. B* **1992**, 45, 13709.
- (29) Wentzcovitch, R. M.; Martins, J. L.; Allen, P. B. Energy versus Free-Energy Conservation in First-Principles Molecular Dynamics. *Phys. Rev. B* **1992**, 45, 11372-11374.
- (30) Niklasson, A. M. N. A Note on the Pulay Force at Finite Electronic Temperatures. *J. Chem. Phys.* **2008**, 129, 244107.
- (31) Rintoul, L.; Micallef, A. S.; Bottle, S. E. The Vibrational Group Frequency of the N-O Stretching Band of Nitroxide Stable Free Radicals. *Spectrochim. Acta Part A* **2008**, 70, 713-717.
- (32) Małolepsza, E.; Witek, H. A.; Morokuma, K. Accurate Vibrational Frequencies Using the Self-Consistent-Charge Density-Functional Tight-Binding Method. *Chem. Phys. Lett.* **2005**, 412, 237-243.
- (33) Koch, W.; Holthausen, M. C.; *A Chemist's Guide to Density Functional Theory*; WILEY-VCH Verlag GmbH: Weinheim, 2001.

- (34) Scott, A. P.; Radom, L. Harmonic Vibrational Frequencies: An Evaluation of Hartree-Fock, Møller-Plesset, Quadratic Configuration Interaction, Density Functional Theory, and Semiempirical Scale Factors. *J. Phys. Chem.* **1996**, *100*, 16502-16513.
- (35) Witek, H. A.; Morokuma, K. Systematic Study of Vibrational Frequencies Calculated with the Self-Consistent Charge Density Functional Tight-Binding Method. *J. Comput. Chem.* **2004**, *25*, 1858-1864.
- (36) Dutta, S.; Pati, S. K. Novel Properties of Graphene Nanoribbons: A Review. *J. Mat. Chem.* **2010**, *20*, 8207-8223.
- (37) Han, M. Y.; Özyilmaz, B.; Zhang, Y.; Kim, P. Energy Band-Gap Engineering of Graphene Nanoribbons. *Phys. Rev. Lett.* **2007**, *98*, 206805.
- (38) Luo, G.; Li, H.; Wang, L.; Lai, L.; Zhou, J.; Qin, R.; Lu, J.; Mei, W.-N.; Gao, Z. Vibrational Infrared Absorption of Graphene Nanoribbons. *J. Phys. Chem. C* **2010**, *114*, 6959-6965.
- (39) Jensen, F; *Introduction to Computational Chemistry*; John Wiley & Sons, Ltd.: England, 2007. (BOOK)
- (40) Reina, A.; Jia, X.; Ho, J.; Nezich, D.; Son, H.; Bulovic, V.; Dresselhaus, M. S.; Kong, J. Large Area Few-Layer Graphene Films on Arbitrary Substrates by Chemical Vapor Deposition. *Nano Lett.* **2009**, *9*, 30-35.
- (41) Banhart, F.; Kotakoski, J.; Krasheninnikov, A. V. Structural Defects in Graphene. *ACS Nano* **2011**, *5*, 26-41.
- (42) Schmidt, M. W.; Baldrige, K. K.; Boatz, J. A.; Elbert, S. T.; Gordon, M. S.; Jensen, J. H.; Koseki, S.; Matsunaga, N.; Nguyen, K. A.; Su, S. et al. General Atomic and Molecular Electronic Structure System. *J. Comput. Chem.* **1993**, *14*, 1347-1363.
- (43) Kubař, T.; Bodrog, Z.; Gaus, M.; Köhler, C.; Aradi, B.; Frauenheim, T.; Elstner, M. Parameterization of the SCC-DFTB Method for Halogens. *J. Chem. Theory Comput.* **2013**, *9*, 2939-2949.
- (44) Witek, H. A.; Morokuma, K.; Stradomska, A. Modeling Vibrational Spectra Using the Self-Consistent Charge Density-Functional Tight-Binding Method. I. Raman Spectra. *J. Chem. Phys.* **2004**, *121*, 5171-5178.
- (45) Gaussian 09, Revision C.01, Frisch, M. J.; Trucks, G. W.; Schlegel, H. B.; Scuseria, G. E.; Robb, M. A.; Cheeseman, J. R.; Scalmani, G.; Barone, V.; Mennucci, B.; Petersson, G. A.; Nakatsuji, H.; Caricato, M.; Li, X.; Hratchian, H. P.; Izmaylov, A. F.; Bloino, J.; Zheng, G.; Sonnenberg, J. L.; Hada, M.; Ehara, M.; Toyota, K.; Fukuda, R.; Hasegawa, J.; Ishida, M.; Nakajima, T.; Honda, Y.; Kitao, O.; Nakai, H.; Vreven, T.; Montgomery, J. A., Jr.; Peralta, J. E.; Ogliaro, F.; Bearpark, M.; Heyd, J. J.; Brothers, E.; Kudin, K. N.; Staroverov, V. N.; Kobayashi, R.; Normand, J.; Raghavachari, K.;

Rendell, A.; Burant, J. C.; Iyengar, S. S.; Tomasi, J.; Cossi, M.; Rega, N.; Millam, M. J.; Klene, M.; Knox, J. E.; Cross, J. B.; Bakken, V.; Adamo, C.; Jaramillo, J.; Gomperts, R.; Stratmann, R. E.; Yazyev, O.; Austin, A. J.; Cammi, R.; Pomelli, C.; Ochterski, J. W.; Martin, R. L.; Morokuma, K.; Zakrzewski, V. G.; Voth, G. A.; Salvador, P.; Dannenberg, J. J.; Dapprich, S.; Daniels, A. D.; Farkas, Ö.; Foresman, J. B.; Ortiz, J. V.; Cioslowski, J.; Fox, D. J. Gaussian, Inc., Wallingford CT, 2009.

- (46) Becke, A. D. Density-Functional Thermochemistry. III. The Role of Exact Exchange. *J. Chem. Phys.* **1993**, 98, 5648-5652.

Chapter 5

Super-Reduced Polyoxometalates: Excellent Molecular Cluster Battery Components and Semipermeable Molecular Capacitors

5.1 Introduction

Polyoxometalate (POM) was first reported by Jöns Jacob Berzelius in 1826,^{1,2} and it was later found that this substance contains the $[\text{PMo}_{12}\text{O}_{40}]^{3-}$ anion. However, its precise molecular structure remained unknown for more than 100 years, until James F. Keggin resolved the structure of a related heteropoly acid species, $\text{H}_3[\text{PW}_{12}\text{O}_{40}] \cdot n\text{H}_2\text{O}$, using X-ray spectroscopy in 1933.³ His data indicated that a central PO_4^{3-} tetrahedral group is surrounded by twelve fused WO_6 octahedrons sharing oxygens at their edges or vertices, and that the trianion adopts T_d symmetry. It later was confirmed that virtually all $[\text{XM}_{12}\text{O}_{40}]^{x-}$ type POMs feature this same structure, referred to as α -Keggin ($\text{X} = \text{P}, \text{Si}, \text{Al}$ etc., $\text{M} = \text{Mo}, \text{W}, \text{V}$, etc.). Other relevant POM structures, for instance, the smaller homopoly Lindqvist⁴ ($[\text{M}_6\text{O}_{19}]^{2-}$), and larger heteropoly structures, such as Anderson-Evans^{5,6} ($[\text{XM}_6\text{O}_{24}]^{x-}$) and Dawson⁷ ($[\text{X}_2\text{M}_{18}\text{O}_{62}]^{x-}$), have been reported as well. With only few exceptions, almost all chemical elements have been incorporated either in the POM structures themselves, or were encapsulated within.⁸

In recent years, the number of experimental⁹⁻¹² as well as theoretical¹³⁻¹⁸ investigations of various POM clusters has increased, due to their fascinating molecular and electronic structures and properties. However, the presence of a minimum of six transition metal atoms in even the smallest possible POM anions represents a challenge for substantive quantum chemical studies.⁸ Fortunately, in recent years, reasonably accurate density functional theory (DFT) has become applicable to such large and complicated molecular systems. Thus, thanks to combined experimental and theoretical efforts, a variety of POM properties such as catalytic activity,^{9,10,16} single molecular magnetism,¹¹ and electrochemical redox potentials^{12,18-20} are now fairly well understood.

One of the most intriguing properties of POM clusters is the highly unusual capability to accept a large number of electrons,²¹⁻²⁴ a property which finds its expression in the term “electron reservoir”² or “electron sponge”²⁵ that is sometimes applied to them. This means for instance that POM clusters have the potential to play an important role as a cathode-active

material. Jean Pierre Launay²⁴ had already reported in the mid 1970's the preparation and characterization of electrochemically highly reduced metatungstate anions.² Based on the observation of irreversible electrode reactions, and simple molecular orbital considerations, he and his coworkers proposed that *three* joint octahedra comprising each of the four corners of the POM cluster would be reduced by up to six electrons, and that *this locally reduced structure would feature W^{IV} - W^{IV} bonds arranged in the form of triangles*.²⁴ However, these suggestions were mere speculation and lacked any direct evidence. More recently, our team reported that in high-capacity lithium batteries,^{23,25-27} a Keggin POM anion containing 12 Mo atoms may indeed hold 24 excess electrons, as determined by *in situ* observed changes of the Mo ion average valences, derived from Mo K-edge X-ray absorption near-edge structure (XANES) absorption edge energies.²⁵ This high uptake of excess electrons (termed “super-reduction” in ref. 25) is the current confirmed record for a single molecular cluster, and certainly remarkable since usually highly charged anions are prone to break covalent bonds and decompose spontaneously. Other chemical compounds exhibiting the features of super-reduction are Mn_x ^{26,27} and iron-sulfur^{28,29} clusters, although these compounds can only accommodate up to 8 and 4 excess electrons per cluster, respectively. Thus, to achieve super-reduction, it is necessary to use molecular clusters with a large number of transition metal atoms. Since POMs are famous for their capability to form supramolecular condensates of well-defined structures,² they possess tremendous potential for the design of molecular clusters capable of super-reduction, possibly even exceeding the current record of 24 electron “super-reduction”.

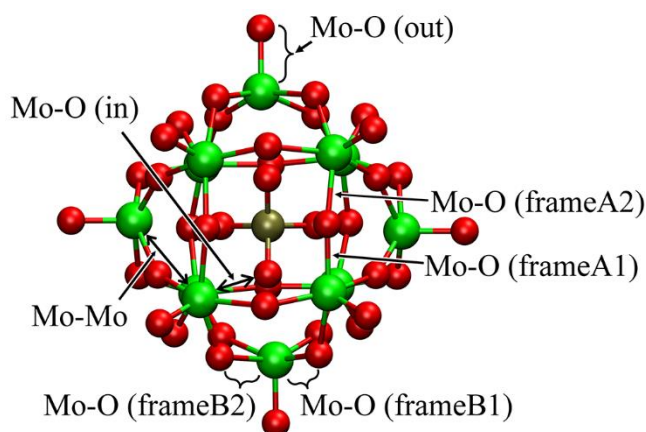


Figure 5.1. BP86-D-optimized structure of $[PMo_{12}O_{40}]^{3-}$ and definitions of characteristic bond lengths. The green, red and olive colored spheres correspond to molybdenum, oxygen and phosphorous atoms, respectively.

In the present work, we focus on the question as to how the Keggin type POM cluster can reach a super-reduced state in a molecular cluster battery (MCB) without being ripped apart by the repulsive Coulombic forces from the large number of excess electrons. In the extended X-ray absorption fine structure (EXAFS) spectrum reported by Wang *et al.*,²⁵ three unique structural changes were reported during reduction by up to 24 electrons: i) Most notably, overall Mo-Mo distances shrank from about 3.6 Å in the “native” Keggin [PMo₁₂O₄₀]³⁻ cluster trianion³⁰ to about 2.6 Å; ii) the Mo-O bonds pointing outward, away from the cluster, increased in length from 1.7 (Mo-O (out) bonds, see Figure 5.1) to about 1.9 Å; and iii) the inner Mo-O bonds (Mo-O (in)) were shortened from 2.4 to about 2.0 Å.

To better understand these structural changes recorded *in situ* by EXAFS, we performed our study theoretically by means of DFT calculations, using both static as well as first principles molecular dynamics (FPMD) approaches. For the discussion of molecular and electronic state structure changes during reduction, we combined available experimental and theoretical data, and employed molecular orbital (MO) analyses in combination with ligand field theory.³¹ Our approach models the super-reduced state of POM by supplying explicit alkali metal atoms around the POM cluster in the DFT calculations.

5.2 Computational Details

The present study mainly employs the heteropoly molybdate α -Keggin ([XMo₁₂O₄₀]³⁻, X=P) polyoxometalate cluster as model system, and we refer to this particular Keggin cage as “POM” in the remainder of the paper. Several calculations were also carried out for its tungsten analog [XW₁₂O₄₀]³⁻ (X=P), and in these cases we will refer to the Keggin cage as “W-POM”. All molecular and electronic structure calculations, as well as on-the-fly direct FPMD simulations, were carried out using DFT^{32,33} as implemented in the TURBOMOLE code.³⁴ We selected the BP86 exchange-correlation^{35,36} and B3LYP³⁷ hybrid functionals with the all-electron, polarized split-valence-type def-SV(P) basis set³⁸ for Li, O, Na and P atoms (def-SV(P) will be abbreviated as SV(P) hereafter), and for Mo and W we employed the TURBOMOLE standard effective core potentials (ECP).³⁹ The semi-empirical dispersion correction as formulated by Grimme⁴⁰ was introduced in order to describe long-range van der Waals interactions, and the functionals are suffixed with “-D” for the correction. A geometry optimization using a larger valence triple- ζ quality basis set (TZVPP)⁴¹ for all elements was also performed for the “native” POM³⁻ cluster. For all BP86 DFT calculations, we introduced the resolution of the identity (RI) approximation⁴² in combination with optimized auxiliary basis sets,^{38,39,41,43} which significantly enhanced the speed of calculation with negligible loss of accuracy. No symmetry constraints were applied in the calculations if not explicitly mentioned otherwise. In all calculations we assumed a closed-shell singlet state using spin-

restricted MOs. For few selected cases, we computed triplet energies and found that they were always higher in energy, indicating that the system tries to adopt a low-spin electronic ground state.

The calculations on the POM^{3-} cluster were carried out in the absence of explicit counterions, i.e. assuming three negative charges on this cluster, unless indicated otherwise. In order to model the reduced $\text{POM}^{(3+n)-}$ clusters, we added $3+n$ neutral alkali metal atoms, either lithium or sodium, around a neutral POM cluster, and set the total charge state of the system in the DFT calculation to zero. For the FPMD simulations in the canonical NVT ensemble, the environmental target temperature was controlled by the Nose-Hoover chain thermostat⁴⁴⁻⁴⁶ as implemented in the TURBOMOLE code (program ‘frog’), and the target temperature was set to 500 K. The thermostat relaxation time was 12.094 fs and the time integration interval was 1.935 fs, since no light hydrogen atoms are included in the system.

For MO-based population analyses, we employed the AOMix^{47,48} code, and analysis of the charge densities was carried out based on natural population analysis (NPA)⁴⁹ as well as Wiberg bond orders.⁵⁰ For visualization of molecular and electronic structures, the VMD⁵¹ and gOpenMol^{52,53} software was used.

5.3 Results and Discussions

5.3.1 Molecular structure of the native Keggin POM^{3-}

The initial geometry of the heteropoly molybdate POM^{3-} ($\text{X}=\text{P}$) cluster was taken from the X-ray structure of Liu *et al.*³⁰ We subjected this geometry to structural optimization at the BP86-D/SV(P) and B3LYP-D/SV(P) levels of theory in vacuum without explicit counterions, assuming a total charge of 3-. Table 5.1 displays key structural parameters for the crystal structure as well as BP86-D- and B3LYP-D-optimized geometries, along with root mean square deviations (RMSDs) of the theoretical geometries from the crystal structure. Although experimentally metal-oxygen bond lengths for the α -Keggin POMs are typically divided into three categories, we identified four different types, consistent with a previous theoretical study by the Poblet group.¹⁷ Six types of Mo-O bonds are distinguished, namely Mo-O (out), Mo-O (in), Mo-O (frameA1), Mo-O (frameA2), Mo-O (frameB1), and Mo-O (frameB2), where the pairs of Mo-O (frameA1) – Mo-O (frameA2) and Mo-O (frameB1) – Mo-O (frameB2) are identical in T_d symmetry but are in fact nonequivalent in lower symmetry calculations, as will be discussed below. The RMSD of the Cartesian coordinates was defined as usual without mass weighting, and measures deviations for maximally overlapping structures. It can be seen that the DFT bond lengths do not deviate from the X-ray structure by more than 0.1 Å. The largest deviation can be seen for the Mo-O (frame) bond lengths.

Table 5.1. Comparison of key structural parameters for POM³⁻ between X-ray³⁰ and DFT-optimized structures. All values are given in units of Å. The location of the bond types is given in Figure 5.1.

	X-ray	BP86-D	B3LYP-D
Mo-Mo	3.563	3.606	3.609
Mo-O (out)	1.684	1.719	1.703
Mo-O (in)	2.442	2.452	2.461
Mo-O (frameA1)	1.920	1.882	1.855
Mo-O (frameA2)		2.011	2.031
Mo-O (frameB1)	1.915	1.867	1.843
Mo-O (frameB2)		1.995	2.016
RMSD^a	0.000	0.127	0.152

^a RMSD values of BP86-D and B3LYP-D are calculated with respect to the X-ray structure as reference.

The existence of four different Mo-O (frame) bond lengths in POMs was already reported in the theoretical study by Yan *et al.*¹⁷ They observed alternating bond length (ABL) distortions for the ring framework Mo-O bonds of POMs, and found that the origin of these distortions, lowering the point group symmetry from T_d to chiral T , is a pseudo Jahn-Teller vibronic instability. In Table 5.1, the ABL distortions are clearly visible in our computed geometries, obtained without symmetry restrictions. The averages over these four Mo-O types are 1.939 Å and 1.936 Å at BP86-D and B3LYP-D respectively, in good agreement with the X-ray structure. In fact, the BP86-D- and B3LYP-D-optimized geometries are remarkably similar, even though B3LYP itself is typically more suitable for systems containing main group elements.⁵⁴ Indeed, the RMSD values indicate that the BP86-D is slightly better in agreement with the X-ray data than B3LYP-D, confirming a general trend in the performance of various DFT functions for transition metal-containing systems.⁵⁵ We additionally performed a BP86-D calculation with a larger basis set (TZVPP) to validate our general use of the double- ζ quality SV(P) basis set. The geometry was similar to the SV(P)-optimized result, and the corresponding RMSD value of this structure with respect to the X-ray geometry was 0.134 Å, indicating that our results did not have significant basis set dependence in the prediction of geometries. Overall, the trend of DFT gas phase optimizations towards larger cage structures is indicative of the important role of crystal field effects on POM³⁻ molecular

cluster geometries. Based on these results, we therefore decided to employ the BP86-D method for the study of POM redox processes, due to its reasonable performance and low computational cost.

5.3.2 Strategies for modeling the molecular and electronic structures of reduced POMs

The quantum chemical study of anions is notoriously difficult, and to make matters worse, even though multiply charged anions in gas phase, such as SO_4^{2-} , CO_3^{2-} , and PO_4^{3-} are ubiquitous in chemistry, they are not stable with respect to autodetachment as isolated species in the gas phase.⁵⁶ Clearly, to accurately describe polyanionic species theoretically, it would be required to a) accurately account for electron correlation, b) use sufficiently large-enough basis sets to accommodate the diffuse electron density of negatively charged species, and c) include the environment of the molecular polyanion in the quantum chemical calculation. Presently none of the available quantum chemical methodologies are capable to “precisely” take into account any of these three important theoretical requirements, let alone all three of them together. Thus, any attempt to model a super-reduced POM molecular cluster has to be conducted within the current limits of computational feasibility, and methodological deficiencies have to be compensated by comparison with solid experimental observations.

Since Keggin POM contains 12 transition metal atoms plus 40 oxygen atoms, *ab initio* methods such as second-order Møller–Plesset perturbation⁵⁷ or configuration interaction⁵⁸ are out of the question for the treatment of electron correlation effects. DFT is presently the only computationally feasible method here, and we have to accept its predictions without a thorough check by more accurate methods, with only limited complimentary information from EXAFS spectra. In terms of the basis set, as we have already indicated above, the split-valence polarized basis set plus ECP for transition metals is sufficiently accurate to describe the geometry of the POM^{3-} cluster. Since our approach of modeling the super-reduced state involves the calculation of charge neutral species by way of inclusion of explicit counterions, the use of larger basis sets is not expected to qualitatively change the BP86-D/SV(P) results of our investigations, in particular since the large number of diffuse basis functions from the alkali metal atoms provides additional flexibility in the description of the MOs of the super-reduced POMs.

Finally, the atomistic structure of the POM cluster environment in the MCB during charging and discharging is presently unknown, and we are thus relying on the assumption that close contacts between the reduced POMs and the counteranions (Li^+) and the dielectric field of the graphitic solid, surrounded by the ethylene carbonate solvent, stabilize the super-reduced species.²⁵ The influence of the counteranions is dominant among the interactions with the cluster environment, and for this reason we explicitly included them in all calculations of the

super-reduced POM. However, an estimate of their number or positions is not available from experiment, and it can be expected that in MCBs large ion density fluctuations can easily occur. Our approach for adding Li or Na counterions in the DFT calculations followed therefore a somewhat heuristic approach. We note in passing that Fleming *et al.* theoretically investigated the effect of absorption of a cluster anion onto a gold surface using polarization-induced mirror charges,⁵⁹ but the explicit use of alkali counterions is more accurate for modeling of a Li-ion battery component than a mirror charge model. Since no detailed structural information for solid and liquid environmental compounds is available from the experiment, we resorted to neglect their influence entirely.

5.3.3 Geometry optimizations of super-reduced POMs

At first we attempted to perform calculations with 27 Li atoms surrounding a neutral POM cluster starting from the POM³⁻ Keggin trianion X-ray structure.³⁰ The Li atoms were initially positioned randomly around the cage, sufficiently close for interaction. After a full geometry optimization of this system, we obtained the structure shown in Figure 5.2. We noticed substantial rearrangement of the positions of Li atoms during the relaxation of the structure. The final POM structure contained four significantly shortened Mo-Mo distances (less than 3.0 Å), three of which formed a triangular Mo site consisting of Mo-Mo bonds in the range from 2.65 to 2.77 Å, their average being 2.73 Å (see Figure 5.2A). These bond lengths are only slightly longer than the previously reported experimental bond length of 2.6 Å for the super-reduced POM from EXAFS,²⁵ and confirm that super-reduction induces Mo-Mo bond formation. In addition, we found that Mo-O (out) bonds for Mo atoms involved in Mo-Mo bonding had significantly stretched by ~0.2 Å to 1.97 Å, while the Mo-O (in) bonds were compressed by a similar amount to 2.18 to 2.20 Å (see Figure 5.2B). These changes in Mo-O bond distances are also in agreement with experimental findings. The ABL related to Mo-O (frame1) and Mo-O (frame2) bonds vanished, and the Mo-O (frame) bonds in this geometry exhibited values between 2.13 to 2.23 Å. This makes the Mo-O (frame) bonds difficult to distinguish from significantly shortened Mo-O (in) bonds in the super-reduced species.

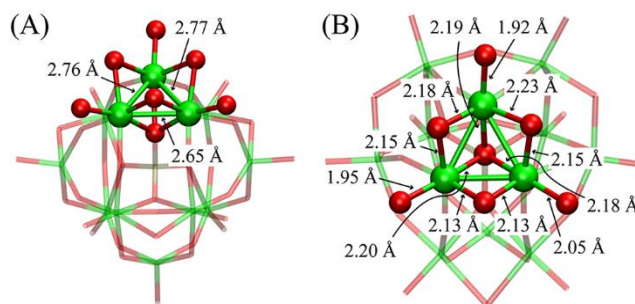


Figure 5.2. Optimized structure of POM with 27 Li labeled structure **4** in Appendix C (alkali metal atoms are omitted for clarity): (A) side view showing Mo-Mo distances, and (B) top view of the triangular Mo site showing Mo-O (in), Mo-O (out), and Mo-O (frame) distances. See Figure 5.1 for the definition of colors.

NPA⁴⁹ carried out for this *ad hoc* optimized POM + 27 Li structure indicated that the POM cluster had only taken up 21.2 electrons from the Li atoms, estimated from the NPA point charge distribution. We performed similar calculations with modified initial geometries of Li atoms, and obtained varying structures, sometimes with, sometimes without Mo triangles. The corresponding total energies of these POM + 27 Li isomers varied on a hundred kcal/mol energy scale, due to the strong Coulombic interaction between counteranions and the negatively charged POM cluster. These explorative studies demonstrated that the potential energy surface (PES) of the POM + 27 Li system is very rough, featuring high barriers separating minimum energy structures associated with Li migration and associated POM structural changes.

Clearly, *ad hoc* geometry optimizations become trapped in local minima, structurally related to the initial choice of Li atom placement. In order to investigate the PES more broadly, and avoid entrapment close to initial geometries, we decided to perform on-the-fly FPMD simulations with subsequent structure optimization (“quenching”) on the basis of BP86-D/SV(P) energies and gradients.

5.3.4 Molecular dynamics simulations of super-reduced POMs

We adopted a relatively high temperature of 500 K for the FPMD simulations in order to more fully explore the associated PES. We note that, although the MCB experiments had been carried out at room temperature,²⁵ the local temperature close to the POM clusters might actually be closer to the target temperature of our MD simulation.

At first, we subjected the previously described POM + 27 Li system to FPMD simulations (trajectory A), starting from the POM³⁻ X-ray geometry. Figure 5.3A displays structural changes during the entire length of the MD simulation, traced by the bond lengths for Mo-Mo in pink, Mo-O (out) in red, Mo-O (in) in green, and Mo-O (frame) in blue color. The FPMD simulation was performed for 1,000 time integration steps, i.e. for a total of 1.935 ps. Three to four short Mo-Mo distances around 2.5 Å ~ 2.8 Å quickly appear in this FPMD simulation, starting around 390 fs. When a bond is formed between two Mo centers, it follows that their distances to other Mo centers has to increase, therefore a large variation in Mo-Mo distances can be observed. Mo-O (out) bonds significantly stretch immediately in FPMD simulations from 1.7 Å, characteristic for the optimized POM³⁻ structure, to an average of 1.85

Å. Mo-O (in) and Mo-O (frame) bond lengths fluctuate with larger amplitudes around average values of 2.47 and 2.06 Å, respectively, indicating that the structural integrity of the POM cluster is compromised. The averages and amplitudes of these particular bond length fluctuations appear converged after around 1 ps simulation time.

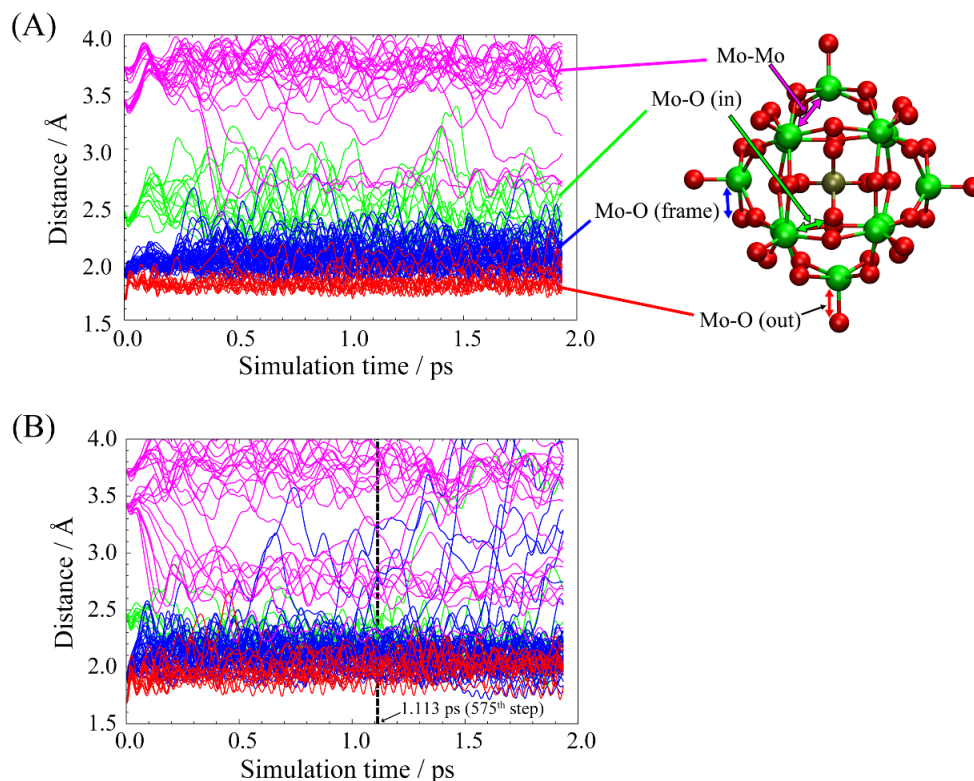


Figure 5.3. Histograms of the bond length fluctuations during the MD simulations of the POM cluster with explicit (A) 27 Li and (B) 35 Li atoms. Bond types are color-coded as follows: Mo-Mo – pink, Mo-O (out) – red, Mo-O (in) – green, Mo-O (frame) – blue, as illustrated in the right-hand side figure. The vertical dotted line in panel (B) indicates the snapshot geometry we selected at 1.113 ps for subsequent geometry optimization of the POM + 35 Li system.

We then proceeded to perform geometry optimization of the final trajectory snapshot at 1.935 ps, which resulted in a structure that features three short Mo-Mo bonds (< 3.0 Å) with bond lengths around 2.68 to 2.69 Å, creating one Mo triangle. The NPA of the charge distribution in this POM + 27 Li cluster shows that 22.7 electrons were transferred to the POM, indicating once again that charge transfer from Li is only partial in nature, at least within the limitations of an atomic point charge analysis. Replacing 27 Li atoms with the more electropositive Na resulted to the counterintuitive result of reduced charge transfer to the POM.

This simulation, the resulting POM + 27 Na structure, and the origin of the ineffectiveness of the larger sodium atoms⁶⁰ to reduce the POM cluster, is discussed in Appendix C. We note that such a counterintuitive result also has been reported for instance in the difference of the solvent stabilization potential between small, polar water molecules and larger, purely ionic liquid cations.⁶¹

To summarize, the simulations we had performed thus far hinted at a qualitative relationship between the numbers of excess electrons on POM and the appearance of short Mo-Mo bonds. Since Li was apparently more effective to afford POM reduction, we decided to add up to 8 more Li atoms to the POM + 27 Li system. Geometry optimizations, starting from the initial structure after adding 8 more Li atoms in random initial positions around the cluster resulted in a structure that featured a total of six short Mo-Mo bonds, one complete and one partial triangular Mo site, and one Mo-Mo single bond with a Wiberg bond order⁵⁰ of 0.936. We then proceeded with FPMD simulations of the POM + 35 Li system, following the same “recipe” as before, i.e. starting from the X-ray POM³⁻ geometry, and supplying randomly 35 Li atoms around this cluster. As before, we employed a target temperature of 500 K and ran the simulation for 1.935 ps, generating trajectory B. Figure 5.4 displays selected snapshot geometries representing the structural changes occurring in this trajectory. In this case, we observed that during the FPMD simulation the POM + 35 Li cluster gradually disintegrated after around 1.26 ps, as can be seen in the rotated view of the final geometry in Figure 5.4D, which shows completely dissociated oxygen binding to nearby Li. The tendency towards disintegration can also be seen in the time evolution of Mo-O (frame) bond lengths in Figure 5.3B, which start to exceed distances around 3.0 Å starting from 1.2 ps.

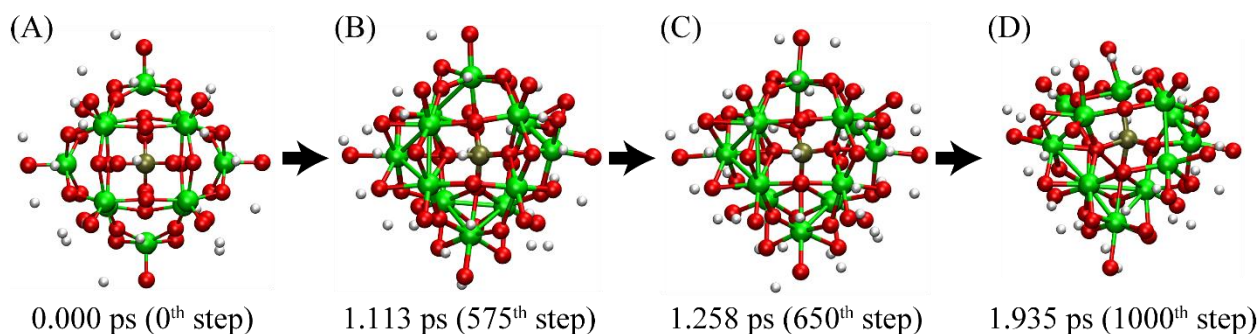


Figure 5.4. Selected snapshots of trajectory B, (A) initial structure at 0.000 ps, (B) snapshot after 1.113 ps, (C) after 1.258 ps, and (D) at the end of the MD simulation after 1.935 ps. See Figure 5.1 for the definition of P, O, and Mo colors; white spheres represent Li atoms.

Figure 5.5 displays the RMSD of the POM cluster atomic coordinates in trajectory B, except for Li atoms, with respect to the initial geometry (POM^{3-}) X-ray geometry. At first, the RMSD value steeply increases as a sign of POM molecular structural changes, then relatively quickly stabilizes around 0.5 Å up to 1.3 ps, just after the snapshot (C) in Figure 5.4. Afterwards, gradual disintegration of the cluster is visible by a continuous increase of the RMSD. We conclude that 35 Li atoms are difficult to accommodate around the Keggin POM cluster, at least at the high temperature of our MD simulation.

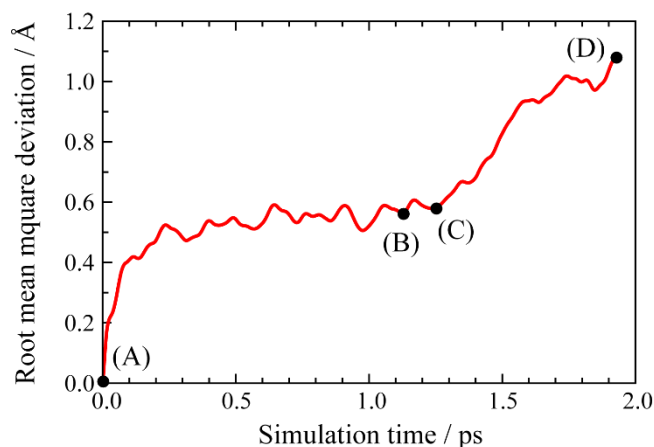


Figure 5.5. RMSD of the POM cluster with respect to the POM^{3-} X-ray geometry during trajectory B as function of the simulation time. The alphabetic letters in the plot identify the snapshots displayed in Figure 5.4.

For further geometry analysis, in this case we decided to extract a snapshot geometry before cage disintegration, in this case at 1.113 ps (see Figure 5.4B corresponding to the structure at the vertical dotted line in Figure 5.3B), and subjected it to geometry optimization. The resulting POM + 35 Li molecular structure featured *two* triangular Mo sites, two single

Mo-Mo bonds, and even one Mo=Mo double bond. The NPA indicates a charge transfer of 28.3 from Li to POM. The bond orders were estimated by Wiberg bond order analysis:⁵⁰ the Wiberg Mo-Mo bond order sums for each triangular Mo site were 2.32 and 2.51, the bond orders of Mo-Mo single bonds were 0.97 and 1.15, and the Mo=Mo double bond had a Wiberg bond order of 2.20, consistent with a very short distance of only 2.33 Å. Similar results were obtained for W-POM + 35 Li systems, only here the number of W-W bonds was typically smaller with about one metal triangle plus an addition metal-metal bond. The POM + 35 Li structure obtained by MD quenching is substantially more stable than the initially optimized structure by 2.95 eV (67.9 kcal/mol), although it is difficult to clarify whether this difference originates from the difference in the number of Mo triangles and Mo-Mo interactions, or from the difference in the positions of Li atoms.

5.3.5 Four metal atom triangles in super-reduced Keggin POMs

The quenched POM + 35 Li structure from trajectory B was the lowest energy structure we could identify thus far, and had the largest number of Mo-Mo bonds (8 single bonds and 1 double bond) and Mo triangles (2). However, the reported experimental structural data supports the notion that *all* Mo-Mo distances in super-reduced POM are converted to short (< 3.0 Å) Mo-Mo single bonds, suggesting that each Keggin cage contains four triangular Mo sites.²⁵ One possible reason for this discrepancy is that, despite the relatively high temperature of 500 K, the MD simulation became still entrapped in a local minimum.

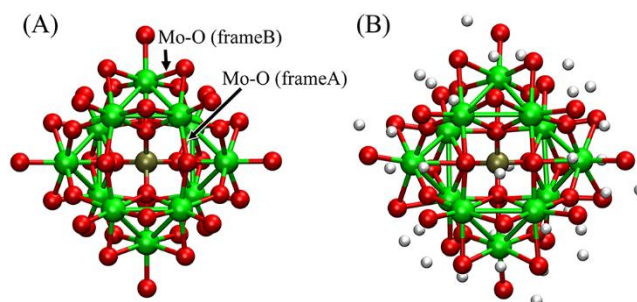


Figure 5.6. (A) Constructed structure, which has four triangular Mo sites, and (B) its optimized structure with 35 Li atoms. The bond threshold for Mo-Mo is 3.0 Å. See Figure 5.1 for the definition of colors, and the white spheres correspond to Li atoms.

In order to theoretically investigate the hypothesis of a super-reduced POM cage with the maximum number of four Mo triangles, we “constructed” a super-reduced POM geometry in T_d symmetry by combining four subunits of three octahedrons to create four Mo-Mo triangles, similar to the proposed structure by Launay²⁴ and others.² In this “constructed”

structure, shown in Figure 5.6A, where all Mo-O (out) distances were set to 1.90 Å and the Mo-O (frame) and Mo-O (in) were set to 2.00 Å following the experimental observation,²⁵ while Mo-Mo distances were assumed to be 2.65 Å on the basis of our previous geometry optimizations of super-reduced POM models. After adorning this cluster with 35 Li atoms in random positions around this constructed structure, we performed a geometry optimization without symmetry constraint. As a result, we obtained a less symmetric cluster as shown in Figure 5.6B, which however now featured the maximum number of four triangular units with 12 Mo-Mo bonds in the range from 2.61 Å to 2.84 Å, indicating the existence of such a minimum energy structure with the maximum number of Mo-Mo triangles. Mo-O (in) and Mo-O (out) bonds were optimized to values ranging from 2.06 Å to 2.15 Å and from 1.93 Å to 2.15 Å, respectively. We note that Mo-O (frame) bonds now split into two groups, termed Mo-O (frameA) and Mo-O (frameB). Their bond lengths are similar, within a range from 2.0 to 2.1 Å. However, while the distance of O (frameA) atoms from the central phosphorous atom does not change significantly during super-reduction with about 3.2 Å, the O (frameB) atoms are “squeezed out” of the cage due to the formation of the underlying Mo-Mo bond, and their distance to the P atom is greatly elongated during the reduction by up to 4.7 Å. Consequently, Mo-O(frameA)-Mo and Mo-O(frameB)-Mo angles are very different with values around 133° and 77°, respectively. Thus, the structural change of the POM cage during super-reduction causes a greater presence of oxygen atoms on its outer surface.

The “constructed” and subsequently optimized POM + 35 Li structure agrees well with our previously reported EXAFS data. NPA shows that the cluster has 28.3 excess electrons. Its energy is 1.44 eV (33.2 kcal/mol) higher than the quenched POM + 35 Li structure, which may be due to an unfavorable arrangement of the Li atoms in the initial geometry. The frontier MO patterns for the W-analog of the previously described Mo-based POM²⁷⁻ super-reduced cluster are identical. Thus, we conclude that the occurrence of metal triangles during super-reduction of Keggin POM clusters is not limited to only heteropolyoxomolybdate but also applies to W-POM.

5.3.6 Molecular orbital analysis of POM super-reduction

For the detailed electronic structure analysis of the super-reduced species, we did not include explicitly alkali metal atoms, since their atomic orbitals strongly mix with the molecular orbitals of the cluster anions, complicating the orbital analysis. Instead, at least to partially stabilize the excessive negative charges, we employed the conductor-like screening model (COSMO)⁶² with a dielectric constant of $\epsilon = 46.3$.⁶³ This particular value of ϵ corresponds to the average value⁶⁴ of the two polar solvents, ethylene carbonate ($\epsilon = 2.8$) and diethyl carbonate ($\epsilon = 89.8$),⁶⁵ used in the experimental MCB setup.²⁵ In order to analyze the super-reduced POM cluster with maximum number of Mo triangles, we firstly examined a *molecular substructure fragment* $[\text{Mo}_3\text{O}_{13}\text{H}_7]^{7-}$ containing a single metal triangle, as shown in

Figure 5.7, created from the “constructed” structure by saturating edge oxygen atoms by hydrogen atoms where necessary. Since there are four such substructures in the α -Keggin POM, and the super-reduction involves 24 excess electrons, one such substructure formally gains six electrons. The substructure fragment possesses C_{3v} symmetry, and BP86-D/SV(P) calculations including the COSMO dielectric continuum solvation model were performed using this point group symmetry.

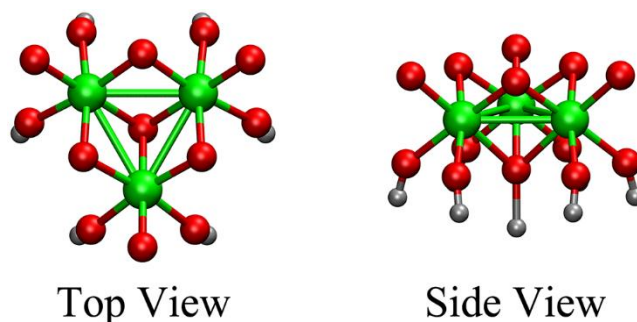


Figure 5.7. Top and side views of the constructed Mo triangle substructure. The gray spheres indicate hydrogen atoms, other colors are consistent with the caption of Figure 5.1.

The Kohn-Sham frontier MOs of the $[\text{Mo}_3\text{O}_{13}\text{H}_7]^{7-}$ subunit, shown in Figure 5.8, indicate that the irreducible representations of the newly occupied three doubly-occupied orbitals are e and a_1 (center column of Figure 5.8). These 3 MOs arise from the hybridization of the 3 Mo 4d orbitals, and with the decreased Mo-Mo distances in the Mo triangle, the overlap of these orbitals has been enhanced and their relative orbital energies lowered. Especially, in the lowest occupied orbital containing two excess electrons, which have a_1 irreducible representation, all three Mo atoms interact via a three-center two-electron bonding orbital. The degenerate e MOs correspond to Mo-Mo bonds, and simultaneously exhibit a strong antibonding character between Mo atoms participating in the metal-metal bond, and the attached outer oxygen atoms, which correspond to the Mo-O (out) bonds of the POM cluster. On the other hand, the LUMO of the reduced substructure possesses anti-bonding character between the three-center bond and the sp^3 hybrid orbitals on the central oxygen atom. Occupation of this MO by additional excess electrons would result in severe weakening of the cage structure, thus a maximum of six excess electrons seems very reasonable for this substructure. As a matter of fact, the existence of triangular metal oxide sites, including the above described orbital patterns, has been predicted previously^{24,66,67} experimentally and theoretically. Our MOs here agree quite well with those predicted by Cotton⁶⁶ in the 1960’s.

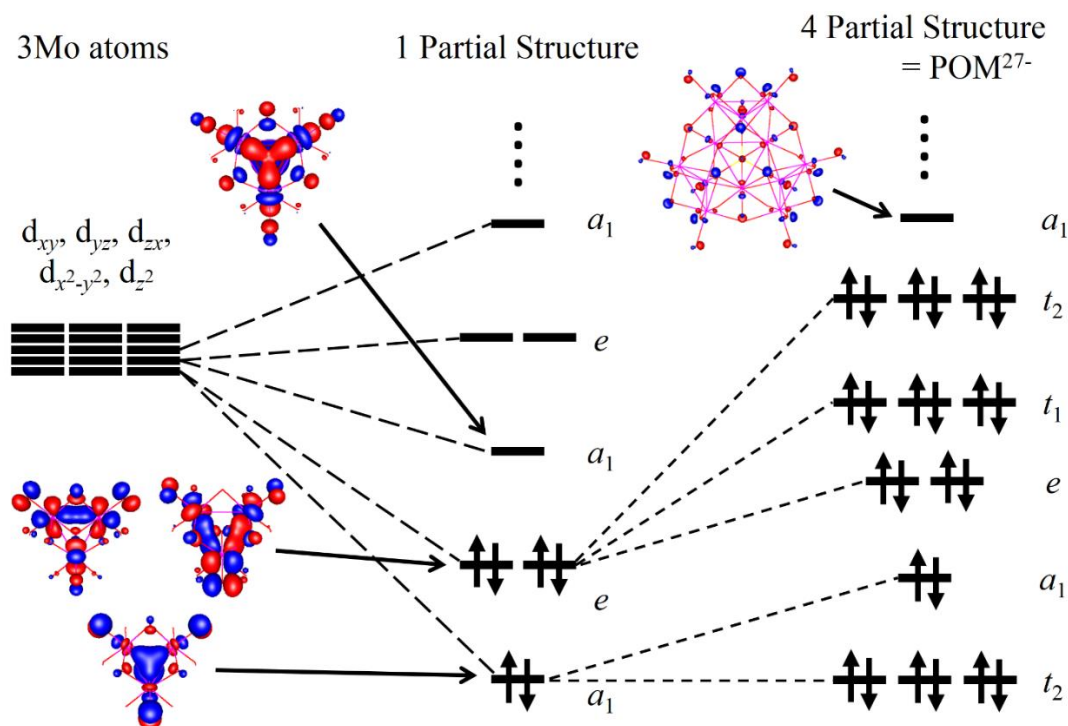


Figure 5.8. MO diagram for one partial structure (center) and POM²⁷⁻ (right). Arrows indicate excess electrons during reduction (6 and 24 electrons for the partial substructure and POM²⁷⁻, respectively). The MO isovalue surface corresponds to $\pm 0.05 (e/a_0)^{1/2}$.

In order to extend the MO analysis to the complete POM²⁷⁻ cluster, we used the constructed POM²⁷⁻ structure (Figure 5.6A) with T_d symmetry. As with the partial substructure MO calculation, the symmetry constraint was used in the BP86-D/SV(P) calculation including the COSMO dielectric continuum solvation method. Once four partial substructures are connected and assembled into POM²⁷⁻, the four a_1 and eight e frontier orbitals containing the excess electrons split into groups of 3 t_2 + 1 a_1 (the four a_1) and 2 e + 3 t_1 + 3 t_2 (the eight e) MOs (see the right column of Figure 5.8). We verified the irreducible representations of the POM²⁷⁻ orbitals and their correspondence to the substructure MOs visually. The LUMO of POM²⁷⁻ is mainly composed of Rydberg 3p orbitals on oxygen atoms (see for instance the visualization of the a_1 LUMO of POM²⁷⁻ in Figure 5.8), indicating that it is impossible to further reduce the α -Keggin POM beyond adding 24 electrons.

The Kohn-Sham occupied frontier MOs of the constructed structure can further be analyzed towards an even more detailed understanding of the origin of the structural changes of the POM cluster upon super-reduction. In Figure 5.9, five MOs representing

the five different irreducible representations of the 12 MOs containing the 24 excess electrons are visualized (only one MO for each degenerate MO level was selected). Three-center orbitals are clearly visible, along with Mo-Mo bonding orbitals. In addition, we find MOs with Mo-O (out) anti-bonding character. The frontier orbital features are consistent with the existence of Mo triangles and the elongation of Mo-O (out) bonds observed in the experiment.²⁵

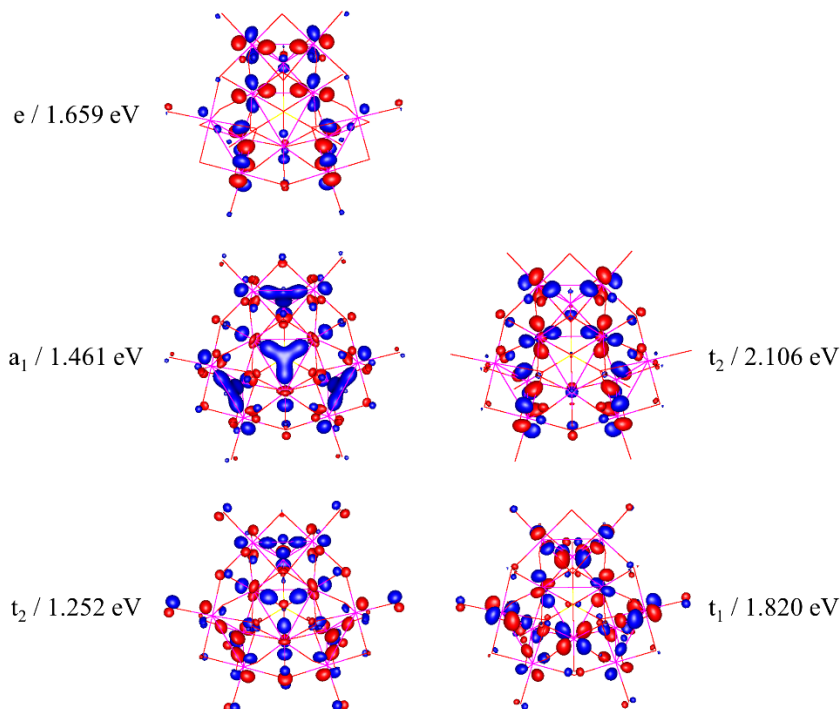


Figure 5.9. Occupied MOs of the constructed structure with 27 negative charges. The MO isovalue surface corresponds to $\pm 0.05 (e/a_0)^{1/2}$. The captions denote irreducible representations / orbital energies

All calculations described above were performed for closed-shell singlet electronic states. The formal charge of all Mo atoms on POM^{3-} is +6, which means that there are no occupied $4d$ levels on the quasi-octahedrally coordinated Mo atoms (see Figure 5.10, left), therefore the ground state of POM^{3-} is famously a singlet,^{68,69} denoted as $^1\text{POM}^{3-}$. However, it is not immediately clear that this is the ground state of the super-reduced POM cluster as well. Thus, we computed low- and high-spin energy gap at the native X-ray (POM^{3-} , symmetrized to T_d) as well as at the “constructed” (POM^{27-}) T_d geometry. We found that the ground state of POM^{27-} at the POM^{3-} geometry (no Mo-Mo bonds) is actually a state with multiplicity $M=2S+1=25$ ($^{25}\text{POM}^{27-}$). In terms of ligand field theory, in this state, two electrons occupy the triply degenerate t_2 atomic $4d$

levels of each octahedrally coordinated Mo center. The closed-shell singlet $M=1$ state is 2.63 eV higher in energy. The occupation of the triply degenerate t_2 Mo 4d level (Figure 5.10, middle) by only two electrons in this geometry triggers a first-order Jahn-Teller effect, reducing the local symmetry of each sixfold coordinated Mo site from quasi- O_h to quasi- C_{4v} , resulting in largely elongated Mo-O(out) bonds and the formation of Mo-Mo bonds. Correspondingly, the large, local Jahn-Teller effects associated with each Mo site hugely stabilizes the closed-shell singlet state (Figure 5.10, right). The gap between closed-shell ground and high-spin $M=25$ state in the distorted structure is 9.76 eV! The local Jahn-Teller effect is the driving force for the molecular and electronic structure changes during super-reduction of the α -Keggin POM cluster.

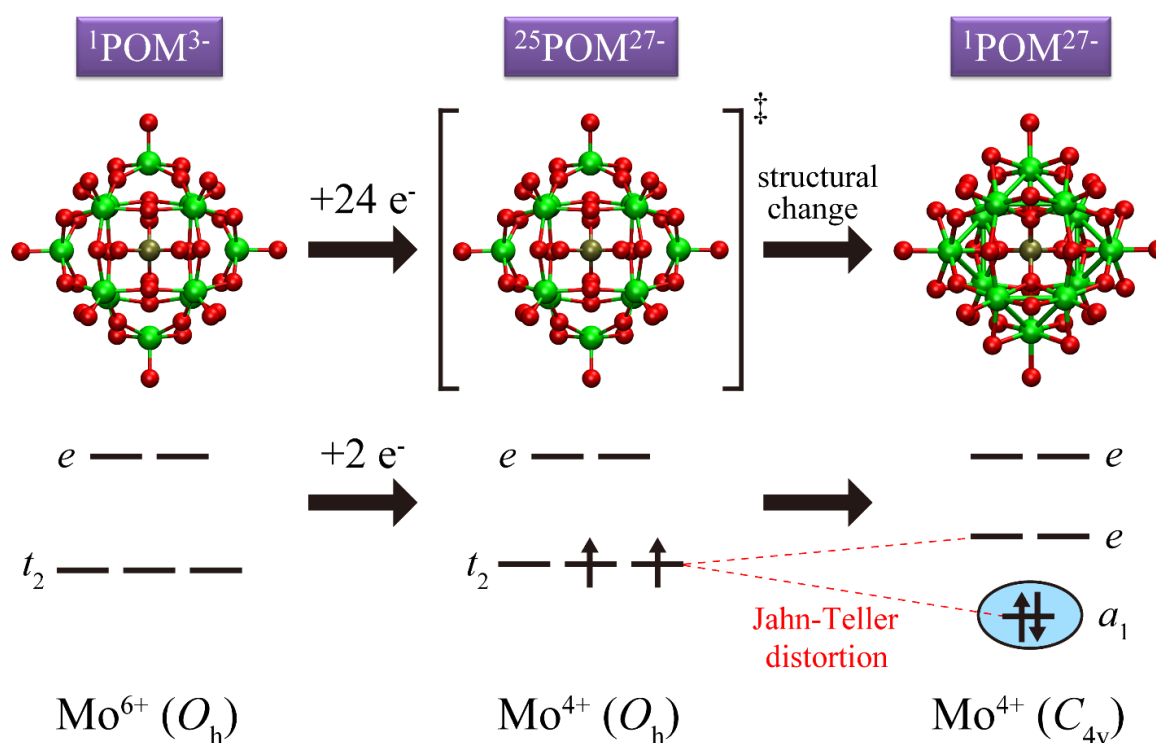


Figure 5.10. Electronic state change during super-reduction of POM^{3-} by 24 excess electrons. The top panel indicates geometries used to compute the $^1\text{POM}^{3-}$ as well as $^{25}\text{POM}^{27-}$ and $^1\text{POM}^{27-}$ geometries, while the bottom panel illustrates the ligand field orbital occupation patterns for a single Mo site, coordinated by six oxygen atoms. A Jahn-Teller distortion to a local C_{4v} environment (with the outward-pointing, axial Mo-O bond becoming elongated) lifts the local orbital degeneracy in the doubly-occupied t_2 level, resulting in a more stable closed-shell singlet electronic state $^1\text{POM}^{27-}$.

5.3.7 Super-reduced POM^{27-} as a semipermeable molecular capacitor

Analysis of NPA point charges on the atoms of the constructed and subsequently optimized structure including 35 Li atoms, depicted in Figure 5.6B, shows that the outer Li shell is strongly positively charged, whereas oxygen atoms “sticking out” from the POM cluster, namely O(out) and, to a lesser degree, O(frameB) are strongly negatively charged, Figure 5.11A depicts NPA atomic charges integrated around spherical shells around the central phosphorous atom. Roughly speaking, there are three “solvation shells” created by the Li atoms: the innermost layer interacting with O(frameA) type oxygen atoms, the second solvation shell interacting with O(frameB) and O(out) type atoms, and the outermost layer, interacting mostly with O(out). Second and third solvation shells are close enough to nearly overlap, so can be classified as a single outer Li shell. The charge-charge interaction between oxygen and Li atoms is difficult to evaluate in this plot, due to the presence of the still strongly positively charged, albeit reduced Mo atoms. Therefore, the changes in NPA atomic charges upon super-reduction, defined as the difference between charges of the optimized structure with four metal triangle sites and POM³⁻ structure are shown in Figure 5.11B. The molecular orientation conforms to that of Figure 5.6B. The electron uptake on Mo is clearly visible, indicated by the red color, as well as slight and stronger electron uptake on frame- and the outward-pointing oxygen atoms, respectively. Li atoms are nearly uniformly positively charged, independent of their position. The situation is schematically depicted in Figure 5.11C, where it becomes clear that interspersing of outer negatively charged oxygen atoms with a large number of positively charged Li atoms in inner and outer shells clearly plays an important role to overcome the huge Coulombic repulsive force due to excess charge on the POM cluster by converting it into attractive Li^{δ+}-O^{δ-} Coulombic interactions, with Li penetrating deep into the negatively charged outer oxygen layer. Thus, super-reduced POM²⁷⁻ can be viewed as a “semipermeable molecular capacitor” with possible future applications in molecular electronics, in addition to its proven effectiveness as cathode material in MCBs.

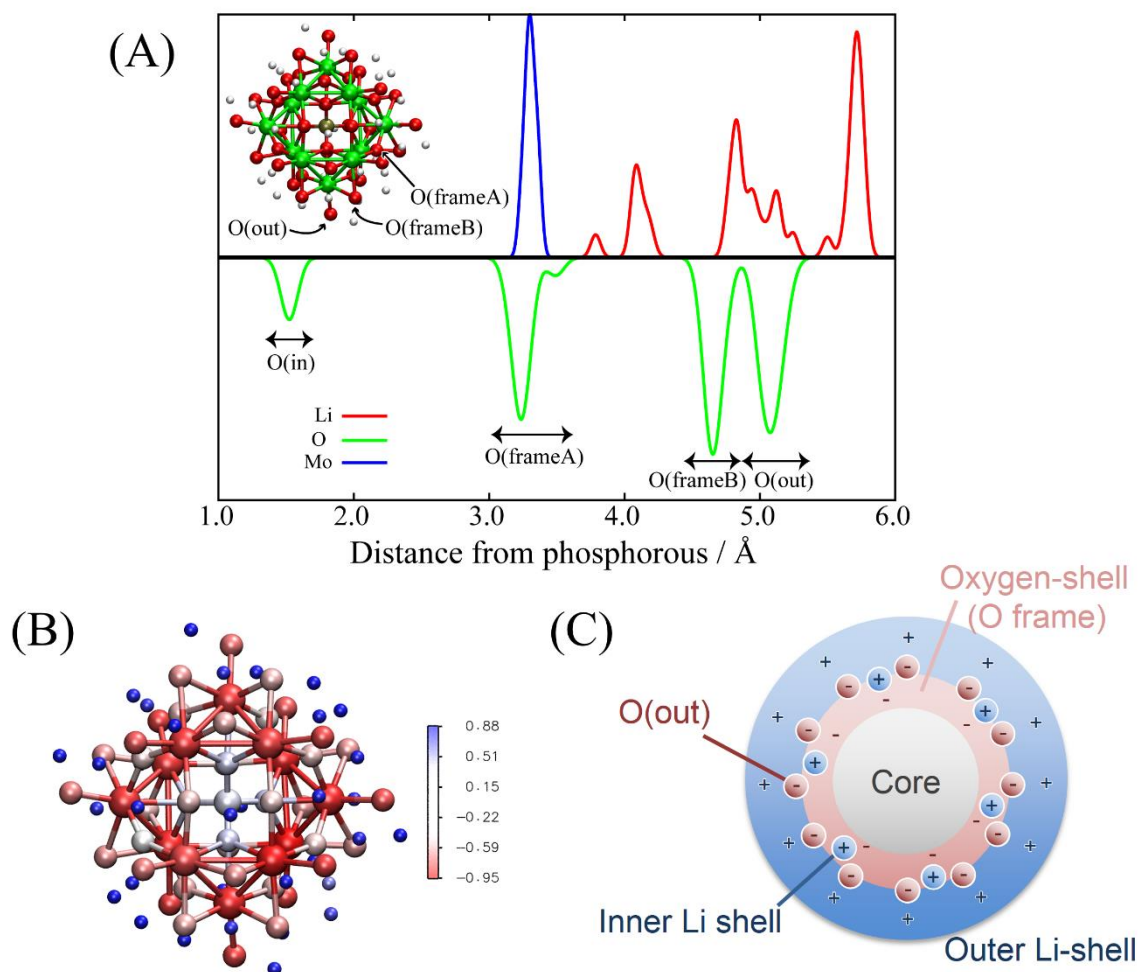


Figure 5.11. Charge distribution in the constructed and subsequently optimized structure including 35 Li atoms, depicted in Figure 5.6B. (A) visualizes integrated NPA atomic charges in shells around the phosphorous center, (B) shows charge changes during the super-reduction of the POM³⁻ cluster by neutral Li atoms, and (C) schematically illustrates the notion of a “semipermeable molecular capacitor”.

5.3.8 Reversibility of the structural changes

Thus far, we have discussed structural changes during reduction of the cluster (POM³⁻ → POM²⁷⁻). In this subsection, we focus on the reverse structural changes for POM²⁷⁻ → POM³⁻, as observed in experiment: even after ten charging and discharging cycles, the decrease in the battery capacity was insignificant.²⁵ Therefore, the structural changes during reduction and oxidation processes must be reversible. To mimic the “oxidation” of the super-reduced POM²⁷⁻ back to POM³⁻, we performed geometry optimizations starting from the neutral “constructed” and optimized structure with 35 Li

atoms, and removed two Li atoms from random positions at the time, and re-optimized the resulting structure, again with 0 charge. This procedure was continued until only 3 Li atoms remained in the system, formally corresponding to POM^{3-} . The procedure is schematically depicted in Figure 5.12. Indeed, the final structure is very similar to the original BP86-D/SV(P) optimized POM^{3-} . The average discrepancy of bond distances is actually only 0.002 Å, therefore we are confident to say that the reversible reduction and oxidation process of the POM cluster is supported by theory.

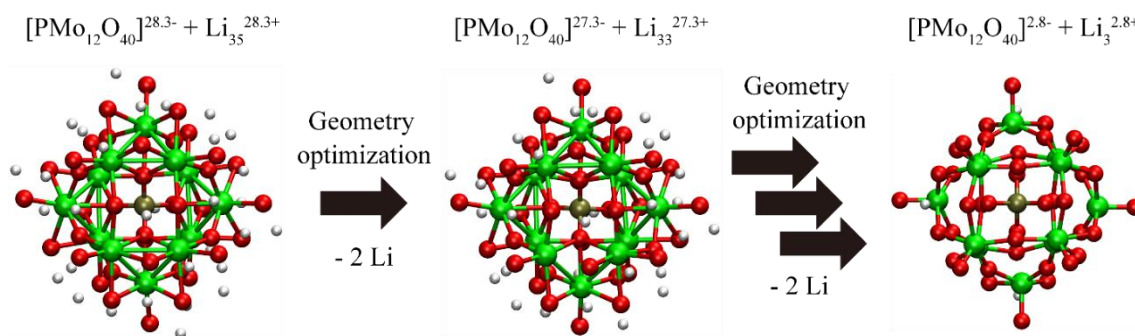


Figure 5.12. Charging of the super-reduced POM^{27-} . Two Li atoms were removed randomly, and the geometry was re-optimized at the BP86-D/SV(P) level of theory until only three Li atoms remained. The total charge of the system was always set to 0.

Since our study indicates the clear correlation between the number of excess electrons and the number of Mo-Mo bonds, it is interesting to follow this trend during our artificial oxidation of POM^{27-} . In Figure 5.13, we plot the number of Mo-Mo bonds that are shorter than 3.0 Å as a function of the NPA-calculated number of excess electrons on the cluster. Interestingly, the number of Mo-Mo bonds is nearly linearly dependent on the number of excess electrons! Our analysis indicates that the first Mo-Mo bond formation may start around the 12th to 14th excess electron, suggesting that local Jahn-Teller distortions due to partially filled t_2 4d levels of *all* Mo atoms of the POM cluster are required for stable metal-metal bond formation.

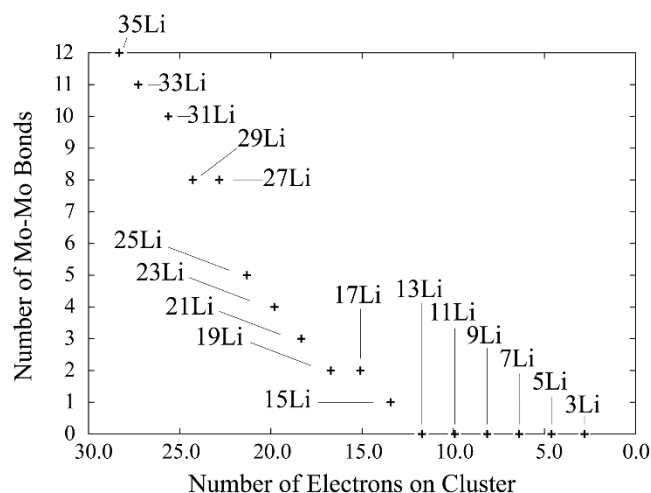


Figure 5.13. Correlation between the number of electrons on the cluster and the number of Mo-Mo bonds (less than 3.0 Å).

5.3.9 Design principles for improved MCB cathode materials

In this work, we have theoretically discussed the structural changes in POMs during discharging in a MCB setup, and the origin of its excellent performance *via* electronic structure analysis. We noted the importance of metal-metal bonding within the POM cluster, and its ability of charge compensation by counterions surrounding it. In order to design even better MCB cathode materials in the future, we conclude from our study that the following structural and electronic features need to be present:

- 1) high density of oxygen atoms on the outside of the cluster,
- 2) transition metal atoms with empty degenerate *d* levels,
- 3) geometrical proximity of these metal atoms such that metal-metal bonds can be formed,
- 4) ability of Li counterions to at least partially migrate into the negatively charged outer oxygen shell to counterbalance repulsive Coulomb forces due to the presence of excess charges.

In preliminary explorations, we already carried out analogous calculations on a Dawson POM cluster, $[\text{P}_2\text{Mo}_{18}\text{O}_{62}]^{6-}$, and its super-reduced analog, $[\text{P}_2\text{Mo}_{18}\text{O}_{62}]^{42-}$. Similar to α -Keggin POM, we observed the formation of Mo-Mo bonds, but in this case Li atoms migrated into the hollow central site and ripped the cluster apart. Further attempts to design enhanced MCB components are currently ongoing in our labs.

5.4 Summary

We theoretically investigated the molecular and electronic structures of the heteropoly molybdate α -Keggin ($[\text{XMo}_{12}\text{O}_{40}]^{3-}$, $\text{X}=\text{P}$) polyoxometalate cluster and its super-reduced state ($[\text{PMo}_{12}\text{O}_{40}]^{27-}$) as well as its tungsten analogue, $[\text{PW}_{12}\text{O}_{40}]^{3-}$ and $[\text{PW}_{12}\text{O}_{40}]^{27-}$. DFT geometry optimizations and FPMD simulations of neutral aggregate species with explicit inclusion of Li atoms around the POM cluster as counterions showed that metal-metal bonds and triangular metal sites are formed due to increasing uptake of excess electrons on the molecular cage. The formation of Mo-Mo bonds during discharging in a MCB is in agreement with previous EXAFS structural data.²⁵ At that time, elongation of Mo-O bonds was also observed, which we attribute to the conversion of Mo=O double bonds pointing outwards of the individual Mo octahedral to Mo-O single bonds, where the oxygen atom becomes negatively charged and favorably interacts with the surrounding Li counteranions. At the same time, during the formation of the Mo triangles, O atoms (frameB) bridging the participant Mo atoms become “squeezed out” and form another attraction point for favorable interaction with the Li counteranions, which were found to form an inner and an outer shell around the POM cluster. The interspersing of positive and negative charges on the outside of the cluster core contributes to overcoming the huge repulsive Coulombic forces due to the presence of 27 negative charges on the POM. *The super-reduced POM can be viewed as a “semiporous molecular capacitor” with possibly broader applications in molecular electronics.*

Electronic structure analysis for a “constructed” structure with T_d symmetry, possessing the maximum number of four Mo triangles in the α -Keggin POM, was carried out in order to understand the origin of the structural changes during super-reduction. The existence of three-center-two-electron bonds at the center of each triangular Mo site was confirmed, and it was found that Mo-Mo bonds are strongly mixed with Mo-O antibonds, shuffling electrons partially away from the Mo sites to the increasingly negatively charged oxygen atoms, which then favorably interact with positive Li counterions. The driving force for the formation of Mo-Mo bonds was found to be local Jahn-Teller distortion at individual Mo octahedral sites, where the triply degenerate t_2 4d orbitals become partially filled during reduction.

Finally, we verified that the reversible structural change of oxidation is plausible theoretically, and indirectly indicate that Mo-Mo bond formation is a stepwise process. Our calculation implies that the first Mo-Mo bond formation may occur after reduction by 12 to 14 electrons. Calculations on the W analogs indicate that the same molecular and electronic structure changes in W-POM can be expected, however, due to the heavier mass of W in comparison to Mo, its capacity in MCBs is expected to be much smaller.

From the above findings, we derived design principles for future, improved MCB cathode materials on the basis of POMs.

Bibliography

- (1) Hill, C. L. *Chem. Rev.* **1998**, 98, 1-2.
- (2) Gouzerh, P.; Che, M. *L'Actualité Chimique*, **2006**, 298, 9/1-14.
- (3) Keggin, J. F. *Nature* **1933**, 131, 908-909.
- (4) Lindqvist, I. *Acta Cryst.* **1950**, 3, 159-160.
- (5) Evans, H. T., Jr. *J. Am. Chem. Soc.* **1948**, 70, 1291-1292.
- (6) Anderson, J. S. *Nature* **1937**, 140, 850-850.
- (7) Dawson, B. *Acta. Cryst.* **1953**, 6, 113-126.
- (8) López, X.; Miró, P.; Carbó, J. J.; Rodríguez-Forteza, A.; Bo, C.; Poblet, J. M. *Theor. Chem. Acc.* **2011**, 128, 393-404.
- (9) Neumann, R.; Dahan, M. *Nature* **1997**, 388, 353-355.
- (10) Sartorel, A.; Carraro, M.; Scorrano, G.; Zorzi, R. D.; Geremia, S.; McDaniel, N. D.; Bernhard, S.; Bonchio, M. *J. Am. Chem. Soc.* **2008**, 130, 5006-5007.
- (11) Compain, J.-D.; Mialane, P.; Dolbecq, A.; Mbomekallé, I. M.; Marrot, J.; Sécheresse, F.; Rivière, E.; Rogez, G.; Wernsdorfer, W. *Angew. Chem.* **2009**, 121, 3123-3127.
- (12) Chiang, M.-H.; Dzielawa, J. A.; Dietz, M. L.; Antonio, M. R. *J. Electroanal. Chem.* **2004**, 567, 77-84.
- (13) Volkmer, D.; Bredenköcker, B.; Kögerler, P.; Kurth, D. G.; Lehmann, P.; Schnablegger, H.; Schwahn, D.; Pipenbrink, M.; Krebs, B. *J. Am. Chem. Soc.* **2002**, 124, 10489-10496.
- (14) Bagno, A.; Bonchio, M. *Angew. Chem.* **2005**, 117, 2059-2062.
- (15) Rodríguez-Forteza, A.; de Graaf, C.; Poblet, J. M. *Chem. Phys. Lett.* **2006**, 428, 88-92.
- (16) Macht, J.; Janik, M. J.; Neurock, M.; Iglesia, E. *Angew. Chem.* **2007**, 119, 8010-8014.
- (17) Yan, L.; López, X.; Carbó, J. J.; Sniatynsky, R.; Duncan, D. C.; Poblet, J. M. *J. Am. Chem. Soc.* **2008**, 130, 8223-8233.
- (18) Aparicio, P. A.; Poblet, J. M.; López, X. *Eur. J. Inorg. Chem.* **2013**, 1910-1916.
- (19) Lira-Cantú, M.; Gómez-Romero, P. *Chem. Mater.* **1998**, 10, 698-704.
- (20) Azumi, B. M.; Ishihara, T.; Nishiguchi, H.; Takita, Y. *Electrochemistry* **2002**, 70, 869-874.
- (21) Pope, M. T.; Müller, A. *Angew. Chem. Int. Ed.* **1991**, 30, 34-38.

- (22) Kuznetsov, A. E.; Geletii, Y. V.; Hill, C. L.; Morokuma, K.; Musaev, D. G. *J. Am. Chem. Soc.* **2009**, *131*, 6844-6854.
- (23) Kawasaki, N.; Wang, H.; Nakanishi, R.; Hamanaka, S.; Kitaura, R.; Shinohara, H.; Yokoyama, T.; Yoshikawa, H.; Awaga, K. *Angew. Chem. Int. Ed.* **2011**, *123*, 3533–3536.
- (24) Launay, J. P. *J. Inorg. Nucle. Chem.* **1976**, *38*, 807-816.
- (25) Wang, H.; Hamanaka, S.; Nishimoto, Y.; Irle, S.; Yokoyama, T.; Yoshikawa, H.; Awaga, K. *J. Am. Chem. Soc.* **2012**, *134*, 4918-4924.
- (26) Yoshikawa, H.; Hamanaka, S.; Miyoshi, Y.; Kondo, Y.; Shigematsu, S.; Akutagawa, N.; Sato, M.; Yokoyama, T.; Awaga, K. *Inorg. Chem.* **2009**, *48*, 9057-9059.
- (27) Wang, H.; Hamanaka, S.; Yokoyama, T.; Yoshikawa, H.; Awaga, K. *Chem. Asian J.* **2011**, *6*, 1074-1079.
- (28) Heering, H. A.; Bultink, Y. B. M.; Hagen, W. R.; Meyer, T. E. *Eur. J. Biochem.* **1995**, *232*, 811-817.
- (29) Torres, R. A.; Loveil, T.; Noodleman, L.; Case, D. A. *J. Am. Chem. Soc.* **2003**, *125*, 1923-1936.
- (30) Liu, S.; Wang, C.; Zhai, H.; Li, D.; *J. Mol. Struct.* **2003**, *654*, 215-221.
- (31) Atkins, P.; Friedman, R. *Molecular Quantum Mechanics*, Oxford University Press Inc., New York, 2005, pp. 122-167.
- (32) Hohenberg, P.; Kohn, W. *Phys. Rev.* **1964**, *136*, B864-B871.
- (33) Kohn, W.; Sham, L. J. *Phys. Rev.* **1965**, *140*, A1133-A1138.
- (34) TURBOMOLE V6.2 2010, a development of University of Karlsruhe and Forschungszentrum Karlsruhe GmbH, 1989-2007, TURBOMOLE GmbH since 2007; available from <http://www.turbomole.com>.
- (35) Becke, A. D. *Phys. Rev. A* **1988**, *38*, 3098-3100.
- (36) Perdew, J. P. *Phys. Rev. B* **1986**, *33*, 8822-8824.
- (37) Becke, A. D. *J. Chem. Phys.* **1993**, *98*, 5648-5652.
- (38) Schäfer, A.; Horn, H.; Ahlrichs, R. *J. Chem. Phys.* **1992**, *97*, 2571-2577.
- (39) Eichkorn, K.; Weigend, F.; Treutler, O.; Ahlrichs, R. *Theor. Chem. Acc.* **1997**, *97*, 119-124.
- (40) Weigend, F.; Häser, M.; Patzelt, H.; Ahlrichs, R. *Chem. Phys. Lett.* **1998**, *294*, 143-152.
- (41) Eichkorn, K.; Treutler, O.; Öhm, H.; Häser, M.; Ahlrichs, R. *Chem. Phys. Lett.* **1995**, *240*, 652-660.
- (42) Weigend, F. *Phys. Chem. Chem. Phys.* **2006**, *8*, 1057-1065.
- (43) Grimme, S. *J. Comp. Chem.* **2006**, *27*, 1787-1799.

- (44)Nose, S. *J. Chem. Phys.* **1984**, *81*, 511-519.
- (45)Hoover, W. G. *Phys. Rev. A* **1985**, *31*, 1695-1697.
- (46)Martyna, G. J.; Klein, M. L.; Tuckerman, M., *J. Chem. Phys.* **1992**, *97*, 2634-2643.
- (47)Gorelsky, S. I. AOMix: Program for Molecular Orbital Analysis; University of Ottawa, 2011, <http://www.sg-chem.net/>
- (48)Gorelsky, S. I.; Lever, A. B. P. *J. Organomet. Chem.* **2001**, *635*, 187-196.
- (49)Reed, A. B.; Weinstock, R. B.; Weinhold, F. *J. Chem. Phys.* **1985**, *2*, 735-746.
- (50)Wiberg, K. B. *Tetrahedron* **1968**, *24*, 1083-1096.
- (51)Humphrey, W.; Dalke, A.; Schulten, K. *J. Mol. Graphics* **1996**, *14*, 33-38.
- (52)Laaksonen, L. *J. Mol. Graphics* **1992**, *10*, 33-34.
- (53)Bergman, D. L.; Laaksonene, L.; Laaksonen, A. *J. Mol. Graphics Mod.* **1997**, *15*, 301-306.
- (54)Koch, W.; Holthausen, M. C. *A Chemist's Guide to Density Functional Theory Second Edition*, WILEY-VCH Verlag GmbH, Weinheim, 2001, pp. 119-136.
- (55)Minenkov, Y.; Singstad, A.; Occhipinti, G.; Jensen, V. R. *Dalton Trans.* **2012**, *41*, 5526-5541.
- (56)Simons, J. *Molecular Anions*, web-based text book, <http://www.hec.utah.edu/anions/Molecular%20Anions.pdf>
- (57)Møller, Chr.; Plesset, M. S. *Phys. Rev.* **1934**, *46*, 618-622.
- (58)Szabo, A.; Ostlund, N. S. *Modern Quantum Chemistry*, Dover Publications, Inc., New York, 1996, pp. 231-270.
- (59)Fleming, C; Long, D.-L.; McMillan, N.; Johnston, J.; Bovet, N.; Dhanak, V.; Gadegaard, N.; Kögerler, P.; Cronin, L.; Kadodwala, M. *Nat. Nanotechnol.* **2008**, *3*, 229-233.
- (60)Slater, J. C. *J. Chem. Phys.* **1964**, *41*, 3199-3204.
- (61)Hayaki, S.; Kido, K.; Yokogawa, D.; Sato, H.; Sakaki, S. *J. Phys. Chem. B* **2009**, *113*, 8227-8230.
- (62)Klamt, A.; Schüürmann, G. *J. Chem. Soc. Perkin Trans. 2* **1993**, *5*, 799-805.
- (63)The conductor-like screening model (COSMO) solvation model was also tried instead of using counteranions, however the dielectric continuum-type solvation model cannot stabilize surplus electrons sufficiently, and failed during self-consistent field (SCF) cycles to converge after several geometry optimization cycles.
- (64)Lide, D. R. ed., *CRC Handbook of Chemistry and Physics, 89th Edition (CD-ROM Version 2009)*, CRC Press/Taylor and Francis, Boca Raton, FL.

- (65) Using the average of two dielectric constants is only a compromise, since we had no other means to treat the solvent structure of the mixture of two solvents in more sophisticated ways.
- (66) Cotton, F. A. *Inorg. Chem.* **1964**, *3*, 1217-1220.
- (67) Ansell, G. B.; Katz, L. *Acta. Cryst.* **1966**, *21*, 482-485.
- (68) Fricke, R.; Öhlmann, G. *J. Chem. Soc., Faraday Trans. 1* **1986**, *82*, 263-271.
- (69) Xu, M.-X.; Lin, S.; Xu, L.-M.; Zhen, S.-L. *Transition Met. Chem.* **2004**, *29*, 332-335.

Chapter 6

Conclusions and Future Perspectives

In this thesis, the two developments of the self-consistent-charge density-functional tight-binding (SCC-DFTB) based methods and a clarification of molecular and electronic structures of super-reduced polyoxometalate (POM^{27-}) cluster have been summarized.

In Chapter 3, the new almost linear scaling method, FMO-DFTB, is introduced by combining DFTB and the fragment molecular orbital (FMO) approach. The scaling of FMO-DFTB is $O(N^{1.1-1.2})$, and the demonstration with a one-million-system is shown. FMO-DFTB calculation for a water cluster with 18 432 atoms is estimated to be around 4 orders of magnitude faster than the corresponding full SCC-DFTB calculation (Figure 6.1). The present method is promising for future application studies for such as proteins, enzymes, DNA, and some nanostructures, due to its advantage of lower computational cost, despite of accurate prediction of energy and geometrical properties (Figure 6.2). However, FMO-DFTB method is still the right after its birth, and many further developments such as including third-order energy expansion of density functional theory (DFT) energy, three-body energy correction, fully analytical gradient, etc., are under progress.

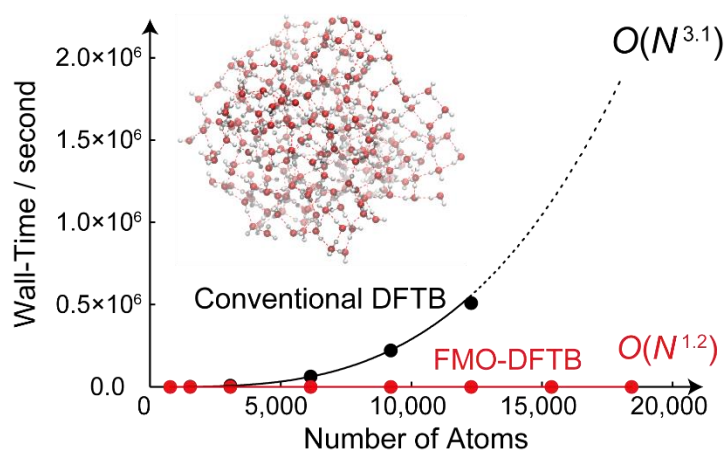


Figure 6.1. Correlation between the number of electrons on the cluster and the number of Mo-Mo bonds (less than 3.0 Å).

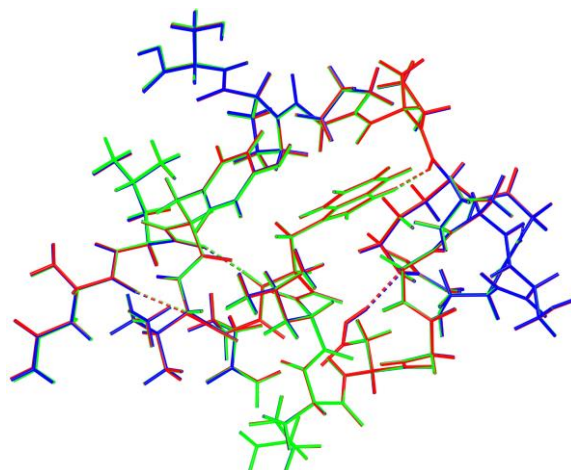


Figure 6.2. Superposition of the optimized structures of the neutralized Trp-cage protein. The blue, red and green lines are used to plot the optimized structures obtained with full SCC-DFTB and FMO-DFTB with 1 and 2 residues per fragment, respectively.

In Chapter 4, the implementation and an application of the second-order geometrical derivative of energy functional of SCC-DFTB with fractional occupation numbers have been discussed. The method developed in this study let us widen the scope of investigation of infrared (IR) and Raman spectroscopy. In this thesis, only a short application for small graphene nanoribbons (GNRs) is reviewed and briefly reviewed IR and Raman spectra (Figure 6.3), however the present methodology is readily applicable for most nanostructures, such as graphene and carbon nanotubes in principle. As DFTB itself is a computationally less demanding method, applications for about a thousand atoms are not very difficult. The spectroscopic information with non-trivial magnetic moment is also important, therefore the extension along this direction is under progress. All implementations in Chapter 3 and 4 will be appeared as a part of the well-known general atomic and molecular electronic structure system (GAMESS) package in near future.

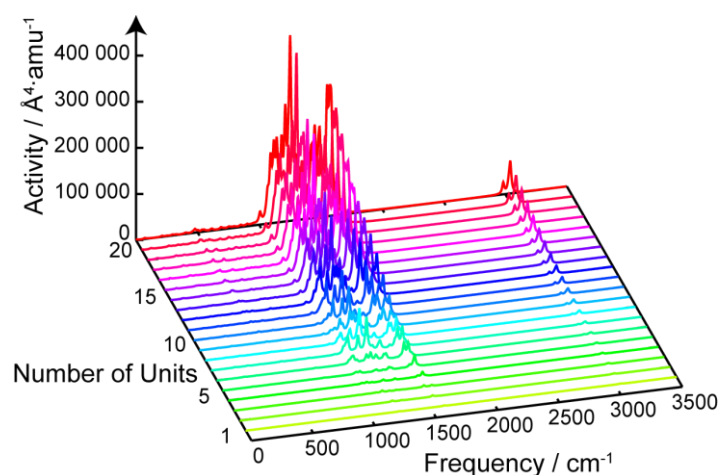


Figure 6.3. Simulated Raman activity spectra of zigzag-GNRs at DFTB with fractional occupation numbers with increasing the number of GNR units.

In addition to the method development, the investigation of the molecular and electronic structures of the super-reduced polyoxometalate (POM^{27-}) cluster with DFT is discussed in detail in Chapter 5. The present study theoretically predicts that metal-metal (Mo and W) bonds and triangular metal sites are formed as a result of increasing uptake of excess electrons on the molecular cluster, overcoming the huge repulsive Coulombic forces due to the presence of 27 negative charges. It must be remarked that there are no former research of such a highly reduced state, and therefore this is the first example in this area. The author hopes that the strategy given in the study helps experimental work aiming at higher capacity.

Acknowledgement

I would like to express my deepest gratitude to my supervisor Professor Stephan Irle. His many suggestions are always my best guidelines so that I can present my achievements and finish this Ph.D thesis. Also I would like to thank my co-supervisors Professor Kunio Awaga and Associate Professor Daisuke Yokogawa for giving insightful comments and suggestions to revise this Ph.D thesis. I really appreciate Associate Prof. Daisuke Yokogawa, Assistance Prof. Yuh Hijikata, and current and former group members for all helps. I would like to sincerely thank Dr. Dmitri G. Fedorov and Mr. Hiroya Nakata, Assistant Professor Hirofumi Yoshikawa, and Dr. Marcus Lundberg for many supports and successfully work collaboration of FMO-DFTB, POM, and Mn₁₂ works respectively. I appreciate many advises and assists of Professor Susumu Saito, Assistant Professor Hiroshi Naka, and Mr. Richiro Ushimaru in Noyori laborabory, and Associate Professor Junichiro Yamaguchi and Mr. Hiroki Kondo in Itami laboratory for the reaction pathway projection with metal catalysts, and current and former group members for all helps.

I would like to thank the financial support by a Research Fellowship of the Japan Society for Promotion of Science for Young Scientists (DC1) and Nagoya University Program for Leading Graduate Schools “Integrative Graduate Education and Research Program in Green Natural Sciences”. Many calculations were performed on powerful computers in the Research Center for Computational Science in Okazaki. Finally, I never forget to appreciate my parents’ support.

Appendix

A. Derivation of Second-Order Geometrical Derivative of Free Energy for Density-Functional Tight-Binding (DFTB) Method with Fractional Occupation Numbers (FONs)

In this Appendix, i, j , and m are the indices of molecular orbitals (MOs), and Greek letters (μ, ν, ρ , and σ) are the indices of atomic orbitals (AOs). A, B, C , and D denote the indices of atoms. a and b for derivatives denote $3N$ Cartesian coordinates (along x, y , and z) of the system of N atoms. The total energy of internal energy is written with the ordinary italic letters (E, F , and G), whereas the total free energy with FONs will be displayed with calligraphic letters, \mathcal{E} , \mathcal{F} , and \mathcal{G} . Complete insights can be accessible with previous literature.¹⁻⁶

Energy and gradient of nonself-consistent-charge (NCC) DFTB method without FONs

For simplicity, we first discuss the NCC-DFTB energy without FONs. The total energy of first-order DFTB (DFTB1), also called as NCC-DFTB, is written as

$$E^{\text{NCC}} = 2 \sum_i^{\text{MO}} f_i \sum_{\mu\nu}^{\text{AO}} c_{\mu i} c_{\nu i} H_{\mu\nu}^0 + \sum_{A>B} V_{AB}^{\text{rep}}, \quad (\text{A.1})$$

where f_i is the occupation number in the i -th MO. In this subsection, we consider the case for the electronic temperature is zero, and thus electronic configuration obeys the Aufbau principle exactly. The $c_{\mu i}$ are the expansion coefficients of the i -th MO in an AO basis. $H_{\mu\nu}^0$ and $S_{\mu\nu}$ is the non-perturbed diatomic-based Hamiltonian and overlap matrix element in the basis of optimized AOs, precomputed for atoms and diatomic systems over a range of bond lengths in reference density-functional theory (DFT) calculations. V_{AB}^{rep} is the two-body repulsive energy term, which is also precomputed and tabulated as a function of interatomic distance from DFT calculations of model systems containing the chemical elements of the A and B atoms. As a result of this approach, V_{AB}^{rep} is independent of the electronic structure and only a function of the interatomic distances. Because of this character and for simplicity, therefore we will abbreviate the second term of eq A.1 as E_{rep} . Because $H_{\mu\nu}^0$ does not depend on \mathbf{c} , NCC-

DFTB is a non-iterative method and hence computationally very economical. When $T_e = 0$, f_i can be classified into only three cases: $f_i = 1$ for doubly occupied orbitals, $f_i = 0.5$ for singly occupied orbitals, and $f_i = 0$ for unoccupied orbitals. Note that our wave function is restricted, so $2f_i$ electrons occupy one spatial orbital. In any cases, the derivative of f_i results in zero. The gradient of energy is then derived as follows:

$$\begin{aligned}
F_a &= \frac{\partial E^{\text{NCC}}}{\partial a} \\
&= 2 \frac{\partial}{\partial a} \sum_i^{\text{MO}} f_i \sum_{\mu\nu}^{\text{AO}} c_{\mu i} c_{\nu i} H_{\mu\nu}^0 + \frac{\partial E^{\text{rep}}}{\partial a} \\
&= 2 \sum_i^{\text{MO}} f_i \sum_{\mu\nu}^{\text{AO}} \left\{ \frac{\partial c_{\mu i}}{\partial a} c_{\nu i} H_{\mu\nu}^0 + c_{\mu i} \frac{\partial c_{\nu i}}{\partial a} H_{\mu\nu}^0 + c_{\mu i} c_{\nu i} \frac{\partial H_{\mu\nu}^0}{\partial a} \right\} + \frac{\partial E^{\text{rep}}}{\partial a} \\
&= 2 \sum_i^{\text{MO}} f_i \sum_{\mu\nu}^{\text{AO}} \sum_m^{\text{MO}} U_{mi}^a (c_{\mu m} c_{\nu i} + c_{\mu i} c_{\nu m}) H_{\mu\nu}^0 + 2 \sum_i^{\text{MO}} f_i \sum_{\mu\nu}^{\text{AO}} c_{\mu i} c_{\nu i} \frac{\partial H_{\mu\nu}^0}{\partial a} + \frac{\partial E^{\text{rep}}}{\partial a} . \quad (\text{A.2})
\end{aligned}$$

In eq (A.2), we have U_{mi}^a which is defined by the following relation,

$$\frac{\partial c_{\mu i}}{\partial a} = \sum_m^{\text{MO}} U_{mi}^a c_{\mu m} . \quad (\text{A.3})$$

To obtain U_{mi}^a coefficients, we usually have to solve the coupled-perturbed (CP) DFTB equation, however we can omit it for first-order derivative case by using the orthonormality of orbitals,

$$S_{ij} = \sum_{\mu\nu} c_{\mu i} c_{\nu j} S_{\mu\nu} = \delta_{ij} . \quad (\text{A.4})$$

The right hand side of eq (A.4) is the Kronecker's delta and is a constant for every i and j , so the derivative of eq (A.4) will be

$$\frac{\partial S_{ij}}{\partial a} = \sum_{\mu\nu}^{\text{AO}} \sum_m^{\text{MO}} U_{mi}^a c_{\mu m} c_{\nu j} S_{\mu\nu} + \sum_{\mu\nu}^{\text{AO}} \sum_m^{\text{MO}} U_{mj}^a c_{\mu i} c_{\nu m} S_{\mu\nu} + \sum_{\mu\nu}^{\text{AO}} c_{\mu i} c_{\nu j} \frac{\partial S_{\mu\nu}}{\partial a} = 0 . \quad (\text{A.5})$$

Eq (A.5) can be made simpler using eq (A.4),

$$\begin{aligned}
\frac{\partial S_{ij}}{\partial a} &= \sum_m^{\text{MO}} U_{mi}^a S_{mj} + \sum_m^{\text{MO}} U_{mj}^a S_{im} + \sum_{\mu\nu}^{\text{AO}} c_{\mu i} c_{\nu j} \frac{\partial S_{\mu\nu}}{\partial a} \\
&= U_{ji}^a S_{jj} + U_{ij}^a S_{ii} + \sum_{\mu\nu}^{\text{AO}} c_{\mu i} c_{\nu j} \frac{\partial S_{\mu\nu}}{\partial a} \\
&= U_{ji}^a + U_{ij}^a + \sum_{\mu\nu}^{\text{AO}} c_{\mu i} c_{\nu j} \frac{\partial S_{\mu\nu}}{\partial a} = 0 . \quad (\text{A.6})
\end{aligned}$$

In order to use eq (A.6), we need to transform the first term of eq (A.2) slightly. The Hamiltonian, which is equivalent to Fock matrix of Hartree-Fock, in MO space of NCC-DFTB is simply

$$F_{ij} = \sum_{\mu\nu}^{\text{AO}} c_{\mu i} c_{\nu j} F_{\mu\nu} = \sum_{\mu\nu}^{\text{AO}} c_{\mu i} c_{\nu i} H_{\mu\nu}^0 = \delta_{ij} \varepsilon_i \quad (\text{A.7})$$

Therefore, the first term of eq (A.2) can be transformed as following,

$$\begin{aligned} \sum_i^{\text{MO}} f_i \sum_{\mu\nu}^{\text{AO}} \sum_m^{\text{MO}} U_{mi}^a (c_{\mu m} c_{\nu i} + c_{\mu i} c_{\nu m}) H_{\mu\nu}^0 &= \sum_i^{\text{MO}} f_i \sum_m^{\text{MO}} U_{mi}^a (F_{mi} + F_{im}) \\ &= \sum_i^{\text{MO}} f_i U_{ii}^a (\varepsilon_i + \varepsilon_i) \\ &= 2 \sum_i^{\text{MO}} f_i U_{ii}^a \varepsilon_i \\ &= - \sum_i^{\text{MO}} f_i \sum_{\mu\nu}^{\text{AO}} c_{\mu i} c_{\nu i} \frac{\partial S_{\mu\nu}}{\partial a} \cdot \varepsilon_i \quad (\text{A.8}) \end{aligned}$$

Here we used the relation of eq (A.7) for $i=j$. With eq (A.8), eq (A.2) becomes the final form,

$$F_a = 2 \sum_i^{\text{MO}} f_i \sum_{\mu\nu}^{\text{AO}} c_{\mu i} c_{\nu i} \left(\frac{\partial H_{\mu\nu}^0}{\partial a} - \varepsilon_i \frac{\partial S_{\mu\nu}}{\partial a} \right) + \frac{\partial E^{\text{rep}}}{\partial a} \quad (\text{A.9})$$

This is the one we usually see in literature.¹

In our implementation, the derivative of Hamiltonian and overlap matrix

($\frac{\partial H_{\mu\nu}^0}{\partial a}$ and $\frac{\partial S_{\mu\nu}}{\partial a}$) are analytically differentiated. We implemented first- and second-order symbolically differentiated terms up to p shells. The analytical differentiation is advantageous for small wave numbers of rotational and translational modes by comparison with numerical differentiation.

Energy and gradient of NCC-DFTB with FONs.

We define DFTB free energy for the case with FONs. Suppose that NCC-DFTB Mermin free energy (\mathcal{E}^{NCC}) is given as

$$\mathcal{E}^{\text{NCC}} = E^{\text{NCC}} + E^{\text{M}}, \quad (\text{A.10})$$

where E^{M} is the correction term for free energy, defined as

The FON, f_i , is governed by the Fermi-Dirac distribution function, and it is a function of the electronic temperature, orbital energies, and Fermi-level. The denominator of two comes from the fact that we assume that we use restricted wave function. Among three parameters, orbital energies and Fermi-level vary against the displacement of nuclear coordinate, so we first note that the derivative of FON solution has to include the derivatives of orbital energies and Fermi-level. Omitting the explicit dependency of temperature for simpler notation, the occupation number of i -th MO is written as

$$f_i = \frac{1}{1 + \exp\left(\frac{\varepsilon_i - \varepsilon_F}{kT_e}\right)} = \left(1 + \exp\left(\frac{\varepsilon_i - \varepsilon_F}{kT_e}\right)\right)^{-1}, \quad (\text{A.12})$$

where ε_i is the eigenvalue (or orbital energy) of i -th MO, and ε_F is the Fermi-level. In our derivation, Fermi-level is numerically decided to satisfy the following equation,

$$N_e = 2 \sum_i^{\text{MO}} f_i, \quad (\text{A.13})$$

where N_e is the number of electrons in the system.

For gradient, we need an additional term of the derivative of occupation number, and the derivative of Mermin free energy, therefore what we need to calculate is

$$\mathcal{F}_a = \frac{\partial \mathcal{E}^{\text{NCC}}}{\partial a} = F_a + 2 \sum_i^{\text{MO}} \frac{\partial f_i}{\partial a} \sum_{\mu\nu}^{\text{AO}} c_{\mu i} c_{\nu i} H_{\mu\nu}^0 + \frac{\partial E^{\text{M}}}{\partial a}. \quad (\text{A.14})$$

The second term becomes simpler expression with eq (A.7),

$$\sum_i^{\text{MO}} \frac{\partial f_i}{\partial a} \sum_{\mu\nu}^{\text{AO}} c_{\mu i} c_{\nu i} H_{\mu\nu}^0 = \sum_i^{\text{MO}} \frac{\partial f_i}{\partial a} \varepsilon_i. \quad (\text{A.15})$$

We can verify that the derivative of free energy correction term is cancelled out with eq (A.15) from the following transformation,

$$\begin{aligned}
\frac{\partial E^M}{\partial a} &= 2kT_e \sum_i^{\text{MO}} \frac{\partial}{\partial a} \{f_i \log f_i + (1 - f_i) \log(1 - f_i)\} \\
&= 2kT_e \sum_i^{\text{MO}} \frac{\partial f_i}{\partial a} \log \left(\frac{f_i}{1 - f_i} \right) \\
&= 2kT \sum_i^{\text{MO}} \frac{\partial f_i}{\partial a} \log \left\{ \left(\exp \left(\frac{\varepsilon_i - \varepsilon_F}{kT} \right) \right)^{-1} \right\} \\
&= -2 \sum_i^{\text{MO}} \frac{\partial f_i}{\partial a} (\varepsilon_i - \varepsilon_F) \\
&= -2 \sum_i^{\text{MO}} \frac{\partial f_i}{\partial a} \varepsilon_i .
\end{aligned} \tag{A.16}$$

The Fermi-level term has disappeared because the sum of the derivative of occupation number disappears with eq (A.13). Since eqs (A.15) and (A.16) are now identical, two terms are cancelled out, giving the final simple result,

$$\mathcal{F}_a = F_a \tag{A.17}$$

This implies that the first-order derivative of free energy is identical to that of internal energy. The derivation above is discussed in the work by Warren et al.⁷ Their work indicated that another broadening function (i.e., Gaussian broadening function) does not cancel itself out in the first derivative formula.

Variational Principle of DFTB with FONs

The general proof for DFT is given in the work by Weinert et al.⁸ and Warren et al.⁷ Since DFTB is derived from the DFT total energy functional, the derivation in the literature above is valid for DFTB, too.

For the case with fixed occupation numbers, the Lagrangian function is given by

$$\mathcal{L} = E^{\text{NCC}} - 2 \sum_i f_i \varepsilon_i \left(\sum_{\mu\nu}^{\text{AO}} c_{\mu i} c_{\nu i} S_{\mu\nu} - 1 \right) \tag{A.18}$$

The stationary condition $\left(\frac{\partial \mathcal{L}}{\partial c_{\mu i}} \right) = 0$ yields the well-known one-electron equations of NCC-DFTB,

$$\sum_{\nu}^{\text{AO}} c_{\mu i} H_{\mu\nu}^0 = \varepsilon_i \sum_{\nu}^{\text{AO}} c_{\nu i} S_{\mu\nu} \tag{A.19}$$

When we use FONs, we need to consider the occupation numbers as an additional variational parameter in the total energy. As a constraint parameter, we use eq (A.13), and the new Lagrangian function is given by

$$\mathcal{L}' = \mathcal{E}^{\text{NCC}} - 2 \sum_i^{\text{MO}} f_i \varepsilon_i \left(\sum_{\mu\nu}^{\text{AO}} c_{\mu i} c_{\nu i} S_{\mu\nu} - 1 \right) - \lambda \left(2 \sum_i^{\text{MO}} f_i - N_e \right) \quad (\text{A.20})$$

where λ is the Lagrangian multiplier for the constraint. If the broadening function for FON is the Fermi-Dirac distribution function (eq (A.12)) and the additional free energy correction term is in the form of eq (A.11) the stationary condition $\left(\frac{\partial \mathcal{L}'}{\partial f_i} \right) = 0$ is fulfilled when $\lambda = \varepsilon_F$. At the same time, the new Lagrangian function, \mathcal{L}' , is stationary with respect to the molecular orbital coefficients $c_{\mu i}$, when eq (A.19) is satisfied for each i which runs over all occupied MOs.

Second-Order Geometrical Derivative of NCC-DFTB without and with FONs

For the case with $T_e = 0$, the second-order geometrical derivative of energy is written as

$$\begin{aligned} G_{ab} = \frac{\partial F_a}{\partial b} = & 2 \sum_i^{\text{MO}} f_i \sum_{\mu\nu}^{\text{AO}} c_{\mu i} c_{\nu i} \left(\frac{\partial^2 H_{\mu\nu}^0}{\partial a \partial b} - \varepsilon_i \frac{\partial^2 S_{\mu\nu}}{\partial a \partial b} - \frac{\partial \varepsilon_i}{\partial b} \cdot \frac{\partial S_{\mu\nu}}{\partial a} \right) \\ & + 2 \sum_i^{\text{MO}} f_i \sum_{\mu\nu}^{\text{AO}} \sum_m^{\text{MO}} U_{mi}^b (c_{\mu m} c_{\nu i} + c_{\mu i} c_{\nu m}) \left(\frac{\partial H_{\mu\nu}^0}{\partial a} - \varepsilon_i \frac{\partial S_{\mu\nu}}{\partial a} \right) + \frac{\partial^2 E^{\text{rep}}}{\partial a \partial b} \end{aligned} \quad (\text{A.21})$$

This is derived by Henryk et al.⁹ (see eq (27) in ref 9). We need U_{mi}^b terms, however for NCC-DFTB, we do not have to calculate CP-DFTB equation. Since off-diagonal elements of Fock matrix in MO basis is zero (eq (A.7)), its derivative will also be zero,

$$\sum_{\mu\nu}^{\text{AO}} \left(\frac{\partial c_{\mu i}}{\partial a} c_{\nu j} H_{\mu\nu}^0 + c_{\mu i} \frac{\partial c_{\nu j}}{\partial a} H_{\mu\nu}^0 + c_{\mu i} c_{\nu j} \frac{\partial H_{\mu\nu}^0}{\partial a} \right) = 0 \quad (i \neq j) \quad (\text{A.22})$$

With eq (A.7), the equation above will be

$$\sum_m^{\text{MO}} (U_{mi}^a F_{mj} + U_{mj}^a F_{im}) + \sum_{\mu\nu}^{\text{AO}} c_{\mu i} c_{\nu j} \frac{\partial H_{\mu\nu}^0}{\partial a} = 0 \quad (\text{A.23})$$

and then, with the diagonal character of Fock matrix,

$$U_{ji}^a \varepsilon_j + U_{ij}^a \varepsilon_i + \sum_{\mu\nu}^{\text{AO}} c_{\mu i} c_{\nu j} \frac{\partial H_{\mu\nu}^0}{\partial a} = 0 \quad (\text{A.24})$$

Finally, with eq (6), we get

$$U_{ij}^a = \frac{1}{\varepsilon_j - \varepsilon_i} \sum_{\mu\nu}^{\text{AO}} c_{\mu i} c_{\nu j} \left(\frac{\partial H_{\mu\nu}^0}{\partial a} - \varepsilon_j \frac{\partial S_{\mu\nu}}{\partial a} \right) \quad (\text{A.25})$$

This procedure is general and valid for self-consistent charge (SCC) DFTB (DFTB2) too. The derivative of eigenvalues can also be obtained with a procedure already shown above, and it will be

$$\frac{\partial \varepsilon_i}{\partial a} = \sum_{\mu\nu}^{\text{AO}} c_{\mu i} c_{\nu i} \left(\frac{\partial H_{\mu\nu}^0}{\partial a} - \varepsilon_i \frac{\partial S_{\mu\nu}}{\partial a} \right) \quad (\text{A.26})$$

The second-order derivative of NCC-DFTB free energy can also be derived from eq (A.9), however of course we need the derivative of occupation number,

$$\mathcal{G}_{ab} = \frac{\partial \mathcal{F}_a}{\partial b} = G_{ab} + 2 \sum_i^{\text{MO}} \frac{\partial f_i}{\partial b} \sum_{\mu\nu}^{\text{AO}} c_{\mu i} c_{\nu i} \left(\frac{\partial H_{\mu\nu}^0}{\partial a} - \varepsilon_i \frac{\partial S_{\mu\nu}^0}{\partial a} \right) \quad (\text{A.27})$$

Regarding the derivative of occupation number, if we differentiate with respect to the displacement of a ,

$$\begin{aligned} \frac{\partial f_i}{\partial a} &= \left(\left(1 + \exp \left(\frac{\varepsilon_i - \varepsilon_F}{kT_e} \right) \right)^{-1} \right)' \\ &= - \left(1 + \exp \left(\frac{\varepsilon_i - \varepsilon_F}{kT_e} \right) \right)^{-2} \cdot \left(1 + \exp \left(\frac{\varepsilon_i - \varepsilon_F}{kT_e} \right) \right)' \\ &= -f_i^2 \cdot \exp \left(\frac{\varepsilon_i - \varepsilon_F}{kT_e} \right) \cdot \frac{1}{kT_e} \left(\frac{\partial \varepsilon_i}{\partial a} - \frac{\partial \varepsilon_F}{\partial a} \right) \\ &= -\frac{f_i^2}{kT_e} \exp \left(\frac{\varepsilon_i - \varepsilon_F}{kT_e} \right) \cdot \left(\frac{\partial \varepsilon_i}{\partial a} - \frac{\partial \varepsilon_F}{\partial a} \right). \end{aligned} \quad (\text{A.28})$$

The exponential of eq (A.28) can be substituted by the following relation. It should be derived from eq (A.12).

$$\exp \left(\frac{\varepsilon_i - \varepsilon_F}{kT_e} \right) = \frac{1 - f_i}{f_i} \quad (\text{A.29})$$

Eq (A.28) is then simplified with eq (A.29) as

$$\frac{\partial f_i}{\partial a} = -\frac{f_i(1 - f_i)}{kT_e} \cdot \left(\frac{\partial \varepsilon_i}{\partial a} - \frac{\partial \varepsilon_F}{\partial a} \right) \quad (\text{A.30})$$

$$\frac{\partial \varepsilon_i}{\partial a}$$

In actual calculation, $\frac{\partial \varepsilon_i}{\partial a}$ term is directly computed at NCC-DFTB from eq (A.26). For

higher order DFTB (SCC-DFTB and DFTB3), it is obtained during coupled-perturbed (CP) DFTB iteration, so the term we have to consider is the unknown term of $\frac{\partial \varepsilon_F}{\partial a}$. If we differentiate both sides of eq (A.13), since the number of electrons in a system is fixed, we get the relation,

$$\sum_i^{\text{MO}} \frac{\partial f_i}{\partial a} = 0 \quad . \quad (\text{A.31})$$

Substituting $\frac{\partial f_i}{\partial a}$ in eq (A.31) with eq (A.30),

$$-\sum_i^{\text{MO}} \frac{f_i(1-f_i)}{kT_e} \cdot \left(\frac{\partial \varepsilon_i}{\partial a} - \frac{\partial \varepsilon_F}{\partial a} \right) = 0 \quad . \quad (\text{A.32})$$

After some transformations, we will get

$$\frac{\partial \varepsilon_F}{\partial a} = \frac{\sum_i^{\text{MO}} f_i(1-f_i) \frac{\partial \varepsilon_i}{\partial a}}{\sum_i^{\text{MO}} f_i(1-f_i)} = \frac{\sum_i^{\text{MO}} f_i(1-f_i) \frac{\partial \varepsilon_i}{\partial a}}{\sum_i^{\text{MO}} f_i(1-f_i)} \quad . \quad (\text{A.33})$$

Once we obtain $\frac{\partial \varepsilon_F}{\partial a}$ with eq (A.33), we can then compute $\frac{\partial f_i}{\partial a}$ with eq (A.30) because there are no unknown terms any more.

Energy and gradient of SCC-DFTB without and with FONs

We have discussed NCC-DFTB zeroth-, first-, and second-order geometrical derivative of energy and free energy (without and with FONs). Now, we are going to discuss these derivatives with SCC-DFTB formalism.¹ Because SCC-DFTB is more or less similar as we have done for NCC-DFTB, we will not repeat all the details. The SCC-DFTB free energy is given as

$$\mathcal{E}^{\text{SCC}} = E^{\text{SCC}} + E^{\text{M}}, \quad (\text{A.34})$$

where

$$E^{\text{SCC}} = 2 \sum_i^{\text{MO}} f_i \sum_{\mu\nu}^{\text{AO}} c_{\mu i} c_{\nu i} H_{\mu\nu}^0 + \frac{1}{2} \sum_{AB} \gamma_{AB} \Delta q_A \Delta q_B + E^{\text{rep}} \quad . \quad (\text{A.35})$$

In SCC-DFTB, we usually calculate Mulliken charges, defined by $\Delta q_A = q_A - q_A^0$, where

$$q_A = 2 \sum_i^{\text{MO}} f_i \sum_{\mu \in A} \sum_{\nu} c_{\mu i} c_{\nu i} S_{\mu\nu}, \quad (\text{A.36})$$

and q_A^0 is the Mulliken population on atom A in the neutral form. The Hamiltonian becomes now

$$H_{\mu\nu} = H_{\mu\nu}^0 + \Omega_{AB} S_{\mu\nu} \quad (\text{A.37})$$

where $\mu \in A$ and $\nu \in B$, and

$$\Omega_{AB} = \frac{1}{2} \sum_C (\gamma_{AC} + \gamma_{BC}) \Delta q_C. \quad (\text{A.38})$$

As the Hamiltonian depends on Ω_{AB} contribution, which depends on Mulliken populations, that depends on c , the solution of SCC-DFTB requires an iterative procedure.

The gradient of SCC-DFTB is written as follows,

$$F_a = 2 \sum_i^{\text{MO}} f_i \sum_{\mu\nu}^{\text{AO}} c_{\mu i} c_{\nu i} \left\{ \frac{\partial H_{\mu\nu}^0}{\partial a} + (\Omega_{AB} - \varepsilon_i) \frac{\partial S_{\mu\nu}}{\partial a} \right\} + \sum_{CD} \frac{\partial \gamma_{CD}}{\partial a} \Delta q_C \Delta q_D + \frac{\partial E^{\text{rep}}}{\partial a} \quad (\text{A.39})$$

The derivative of SCC-DFTB free energy is also identical to the derivative of SCC-DFTB internal energy (Eq. (A.17)).

Second-Order Geometrical Derivative of SCC-DFTB without and with FONs

We are going to discuss the second derivative of SCC-DFTB. First when $T_e = 0$, the second-

order geometrical derivative of SCC-DFTB is

$$\begin{aligned} G_{ab} = & 2 \sum_i f_i \sum_{\mu\nu} c_{\mu i} c_{\nu i} \left\{ \frac{\partial^2 H_{\mu\nu}^0}{\partial a \partial b} + (\Omega_{AB} - \varepsilon_i) \frac{\partial^2 S_{\mu\nu}}{\partial a \partial b} + \left(\frac{\partial \Omega_{AB}}{\partial b} - \frac{\partial \varepsilon_i}{\partial b} \right) \frac{\partial S_{\mu\nu}}{\partial a} \right\} \\ & + 2 \sum_i f_i \sum_{\mu\nu} \sum_m U_{mi}^b (c_{\mu m} c_{\nu i} + c_{\mu i} c_{\nu m}) \left\{ \frac{\partial H_{\mu\nu}^0}{\partial a} + (\Omega_{AB} - \varepsilon_i) \frac{\partial S_{\mu\nu}}{\partial a} \right\} \\ & + \sum_{CD} \left(\Delta q_C \Delta q_D \frac{\partial^2 \gamma_{CD}}{\partial a \partial b} + \frac{\partial \gamma_{CD}}{\partial a} \frac{\partial q_D}{\partial b} \Delta q_D + \frac{\partial \gamma_{CD}}{\partial a} \Delta q_C \frac{\partial q_D}{\partial b} \right) + \frac{\partial^2 E^{\text{rep}}}{\partial a \partial b} \end{aligned} \quad (\text{A.40})$$

where

$$\frac{\partial q_A}{\partial a} = 2 \sum_i f_i \sum_{\mu \in A} \sum_{\nu} \left\{ c_{\mu i} c_{\nu i} \frac{\partial S_{\mu\nu}}{\partial a} + \sum_m U_{mi}^a (c_{\mu m} c_{\nu i} + c_{\mu i} c_{\nu m}) S_{\mu\nu} \right\} \quad (\text{A.41})$$

$$\frac{\partial \Omega_{AB}}{\partial a} = \sum_C \left\{ \frac{1}{2} \left(\frac{\partial \gamma_{AC}}{\partial a} + \frac{\partial \gamma_{BC}}{\partial a} \right) \Delta q_C + \frac{1}{2} (\gamma_{AC} + \gamma_{BC}) \frac{\partial \Delta q_C}{\partial a} \right\} \quad (\text{A.42})$$

$$U_{ij}^a = \frac{1}{\varepsilon_j - \varepsilon_i} \sum_{\mu\nu} c_{\mu i} c_{\nu j} \left\{ \frac{\partial H_{\mu\nu}^0}{\partial a} + (\Omega_{AB} - \varepsilon_j) \frac{\partial S_{\mu\nu}}{\partial a} + S_{\mu\nu} \frac{\partial \Omega_{AB}}{\partial a} \right\} \quad (\text{A.43})$$

$$U_{ii}^a = -\frac{1}{2} \sum_{\mu\nu} c_{\mu i} c_{\nu i} \frac{\partial S_{\mu\nu}}{\partial a} \quad (\text{A.44})$$

and

$$\frac{\partial \varepsilon_i}{\partial a} = \sum_{\mu\nu} c_{\mu i} c_{\nu i} \left\{ \frac{\partial H_{\mu\nu}^0}{\partial a} + (\Omega_{AB} - \varepsilon_i) \frac{\partial S_{\mu\nu}}{\partial a} + S_{\mu\nu} \frac{\partial \Omega_{AB}}{\partial a} \right\}. \quad (\text{A.45})$$

The set of equations indicates that we need to solve the CP-DFTB equation, because in order to obtain U_{ij}^a , we need $\frac{\partial \Omega_{AB}}{\partial a}$, which depends on the derivative of Mulliken charges

$\left(\frac{\partial \Delta q_C}{\partial a} \right)$, which depends on U_{ij}^a matrix. The CP equation sometimes behaves divergently as pointed out in ref 9. We used the modified Broyden charge mixing¹⁰ to control the convergence of CP-DFTB equation. Instead of explicitly control \mathbf{U} matrix, we controlled the $\frac{\partial \Delta q_C}{\partial a}$ vector because the dimension is smaller.

The second derivative of SCC-DFTB with FONs requires an additional term of derivative of occupation numbers,

$$\mathcal{G}_{ab} = G_{ab} + 2 \sum_i^{\text{MO}} \frac{\partial f_i}{\partial b} \sum_{\mu\nu}^{\text{AO}} c_{\mu i} c_{\nu i} \left\{ \frac{\partial H_{\mu\nu}^0}{\partial a} + (\Omega_{AB} - \varepsilon_i) \frac{\partial S_{\mu\nu}}{\partial a} \right\} \quad (\text{A.46})$$

However, there is one more complexation. The derivative of Mulliken charge needs one more

term of the derivative of occupation number. For the case with FON, we use the notation

of \mathcal{Q} , giving that

$$\frac{\partial \mathcal{Q}_A}{\partial a} = \frac{\partial q_A}{\partial a} + 2 \sum_i^{\text{MO}} \frac{\partial f_i}{\partial a} \sum_{\mu \in A} \sum_{\nu}^{\text{AO}} c_{\mu i} c_{\nu i} S_{\mu\nu} \quad (\text{A.47})$$

Now that, we have obtained all information to solve the CP-DFTB equation and to get \mathcal{G}_{ab} .

B. Structures and Vibrational Frequencies of Nitroxyl Radicals

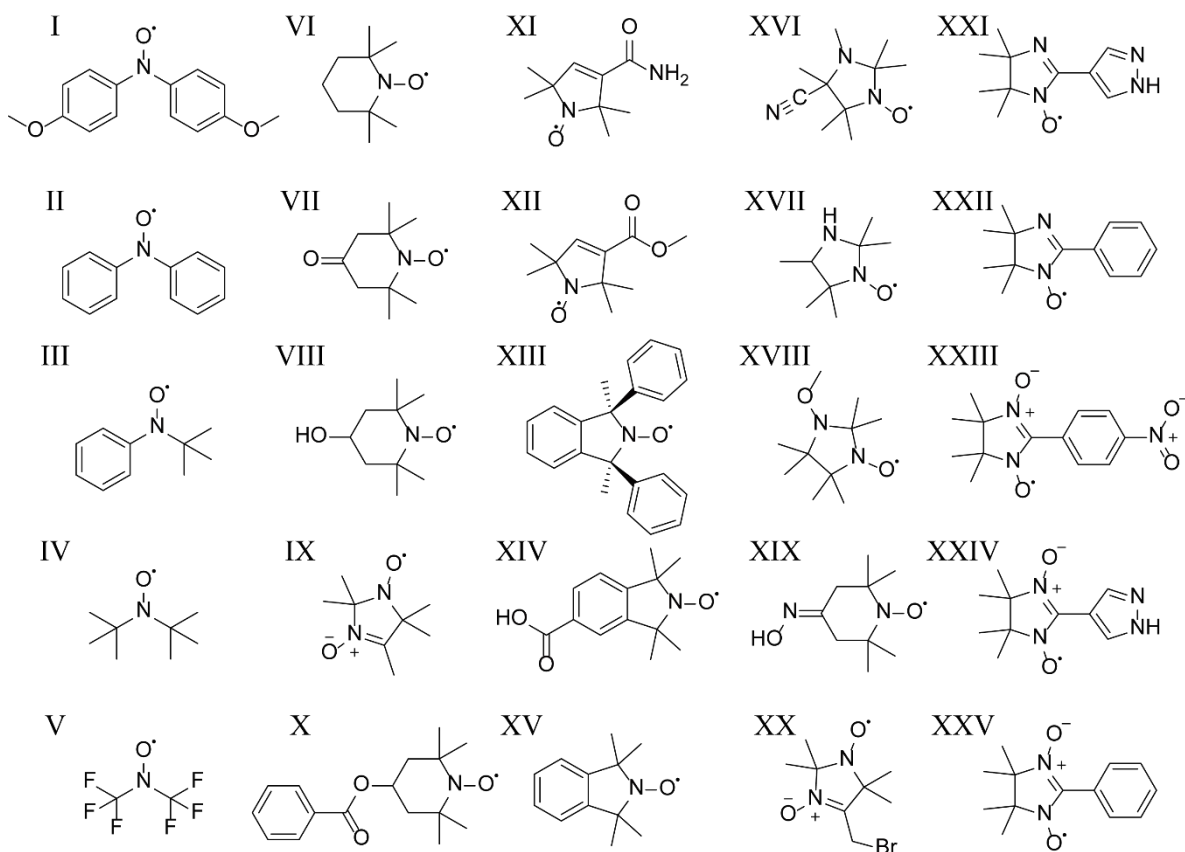


Figure B1. Structures containing N-O radical stretching mode, corresponding to Table S2.

Table B1. Experimental (Exp.) vibrational frequencies (unit in cm^{-1}) of N-O radical stretching mode, and calculated frequencies at B3LYP/6-311++G(d,p) and at DFTB with mio and slkoopt parameter sets. Calculated frequencies are scaled by each scaling factor (SF). See Figure B1 for schematic structures.

	Exp.	B3LYP		DFTB (mio)		DFTB (slkoopt)	
SF		1.000	0.976	1.000	0.952	1.000	0.959
I	1344	1380.05	1346.93	1430.64	1361.97	1382.28	1325.61
II	1342	1384.59	1351.36	1435.06	1366.18	1387.82	1330.92

III	1370	1390.74	1357.36	1307.55	1244.79	1318.62	1264.56
IV	1342	1368.39	1335.55	1430.27	1361.62	1408.67	1350.91
V ^a	1397	1415.55	1381.58	1444.62	1375.28	←	1385.39
VI	1339	1371.90	1338.97	1422.10	1353.84	1427.71	1369.17
VII	1380	1381.03	1347.89	1430.33	1361.67	1439.98	1380.94
VIII	1371	1376.17	1343.14	1424.31	1355.94	1430.28	1371.64
IX	1362	1380.25	1347.12	1431.41	1362.70	1439.90	1380.86
X	1350	1381.80	1348.64	1418.60	1350.51	1425.90	1367.44
XI	1438	1465.56	1430.39	1509.36	1436.91	1502.64	1441.03
XII	1435	1468.04	1432.81	1509.20	1436.76	1501.45	1439.89
XIII	1366	1457.30	1422.32	1485.89	1414.57	1470.49	1410.20
XIV	1367	1469.84	1434.56	1501.60	1429.52	1496.19	1434.85
XV	1428	1465.95	1430.77	1501.80	1429.71	1497.38	1435.99
XVI	1438	1464.35	1429.21	1499.37	1427.40	1504.01	1442.35
XVII	^b	1467.88	1432.65	1515.86	1443.10	1501.04	1439.50
XVIII	^b	1454.08	1419.18	1485.71	1414.40	1501.33	1439.78
XIX	1436	1469.20	1433.94	1491.11	1419.54	1499.63	1438.15
XX ^a	1436	1469.73	1434.46	1489.99	1418.47	←	1428.90
XXI	1370	1461.31	1426.24	1387.71	1321.10	1360.98	1305.18
XXII	^b	1459.05	1424.03	1434.71	1365.84	1383.40	1326.68
XXIII ^c	2457 /	1485.02	1485.02	1675.84	1595.40	1671.49	1602.96
	2695 /	/	/	/	/	/	/
		1474.35	1474.35	1505.40	1433.14	1448.10	1388.73
XXIV	1367	1445.11	1445.11	1437.66	1368.65	1416.50	1358.42
XXV	1371	1438.23	1438.23	1501.61	1429.53	1441.30	1382.21
RMS		49.35	28.10	79.45	38.43	68.85	34.15
MAX		102.84	67.56	134.60	125.21	129.19	105.44

^a Pure “halorg-0-1” parameters are used for both mio and slkoopt sets

^b Experimental data are not available.

^c Experimental values are so different from all calculated vibrational frequencies that these data are excluded as an exception.

C. Molecular Dynamics Simulations of Supre-Reduced POM with Sodium Atoms

To further enhance charge transfer, we substituted lithium atoms in the POM + 27 Li system by the more electropositive sodium to create a POM + 27 Na system and performed a similar FPMD simulation as described in the manuscript for the POM + 27 Li system. Figure S1 displays the corresponding time evolution of the characteristic Mo-Mo and Mo-O bonds for this trajectory. Contrary to our expectation, only one short Mo-Mo was obtained during the entire length of the simulation, and the fluctuations of Mo-O (in) and (frame) bonds showed smaller amplitudes relative to the POM + 27 Li simulation. After geometry optimization of the final MD snapshot (structure **6** in Appendix C), only one short Mo-Mo bond survived, and the NPA indicated that the number of transferred electrons to the POM cluster was only 16.0. Surprisingly, the more electropositive Na proved less efficient for simulating electron transfer to POM than Li.

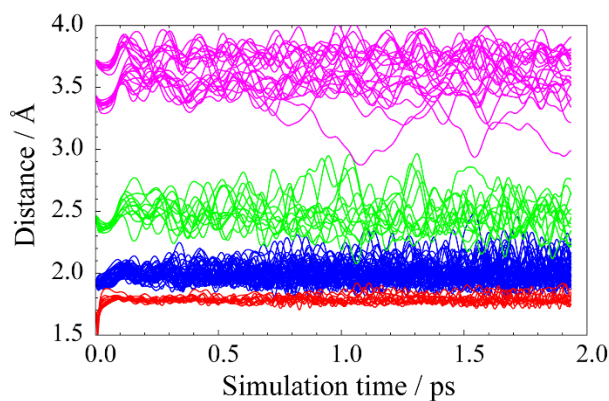


Figure S1. Histogram of the bond length fluctuations during the MD simulations of the POM cluster with explicit 27 Na atoms. Bond types are color-coded as follows: Mo-Mo – pink, Mo-O (out) – red, Mo-O (in) – green, Mo-O (frame) – blue.

Understanding the molecular structure of the counterion-“solvated” POM cluster is important to understand why the more electropositive Na is less effective than Li in inducing the metal oxide cluster reduction. Figure S2 displays the radial distribution functions for the distances between oxygen atoms belonging to the POM frame, and the

alkali metal atoms. The distribution is sampled over the entire 1.935 ps simulation time span in case of 27 Li (red) and Na (green), and over the first 1.113 ps in case of the 35 Li (blue) simulation. The approximate sizes of the first “solvation” shell are notably different: Li-O (frame) distances are about 0.4 Å shorter than corresponding Na-O (frame) distances. This finding can be rationalized by the fact that the ionic radius of tetracoordinated Li^+ is significantly smaller with 0.59 Å than that of tetracoordinated Na^+ with 0.99 Å.¹ Since the Coulomb potential is proportional to the inverse of the distance between two point charges, the electrostatic potential by Li would be about 1.68 times stronger than that by Na, if charge transfer from each type of alkali metal was identical. Even if this cannot be assumed, there clearly is a delicate interplay between charge transfer and the distance of metal counteranions to the cluster, in particular to the negatively charged oxygen atoms of the POM cluster which “stick out” more in the compressed, super-reduced species. It is clear that, since the Li ion is already smaller by around 0.40 Å compared to the Na ion,¹ it is able to achieve a potentially stronger attractive Coulombic interaction during its movement around POM, compared to Na. Consequently, charge transfer from Li to POM is enhanced in comparison to Na, with $22.7/27=0.84$ excess charge per Li atom for the quenched POM + 27 Li structure (structure 5), compared to $16.0/27=0.59$ excess charge per Na atom for the corresponding POM + 27 Na structure (structure 6). Such counterintuitive result has been reported for instance also in the difference of the solvent stabilization potential between small water molecules and larger ionic liquid ions.²

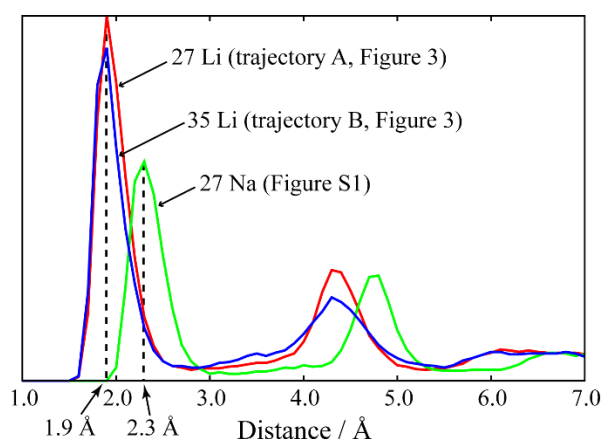


Figure S2. Radial distribution functions for the distances between oxygen (frame) and alkali metal cations, sampled over the entire timespan of trajectories A and POM + 27 Na, and up to 1.113 ps in case of the trajectory B (see Figure 5.3 for trajectories A and B).

Bibliography

Appendix A (tentative)

- (1) Elstner, M.; Porezag, D.; Jungnickel, G.; Elsner, J.; Haugk, M.; Frauenheim, T.; Suhai, S.; Seifert, G. *Phys. Rev. B* **1998**, *58*, 7260-7268.
- (2) Koskinen, P.; Mäkinen, V. *Comput. Mater. Sci.* **2009**, *47*, 237–253.
- (3) Oliveira, A. F.; Seifert, G.; Heine, T.; Duarte, H. A. *J. Braz. Chem. Soc.* **2009**, *20*, 1193–1205.
- (4) Gaus, M.; Cui, Q.; Elstner, M. *J. Chem. Theory Comput.* **2011**, *7*, 931–948.
- (5) Seifert, G.; Joswig, J.-O. *WIREs Comput. Mol. Sci.* **2012**, *2*, 456–465.
- (6) Gaus, M.; Cui, Q.; Elstner, M. *WIREs Comput. Mol. Sci.* **2014**, *4*, 49–61.
- (7) Warren, R. W.; Dunlap, B. I. *Chem. Phys. Lett.* **1996**, *262*, 384–392.
- (8) Weinert, M.; Davenport, J. W. *Phys. Rev. B* **1992**, *45*, 13709–13712.
- (9) Witek, H. A.; Irle, S.; Morokuma, K. *J. Chem. Phys.* **2004**, *121*, 5163–5170.

Appendix C

- (10) Slater, J. C. *J. Chem. Phys.* **1964**, *41*, 3199-3204.
- (11) Hayaki, S.; Kido, K.; Yokogawa, D.; Sato, H.; Sakaki, S. *J. Phys. Chem. B* **2009**, *113*, 8227-8230.

List of Publications

Chapter 3

Nishimoto, Y.; Fedorov, D. G.; Irle, S. “Density-Functional Tight-Binding Combined with the Fragment Molecular Orbital Method”, *J. Chem. Theory Comput.* **2014**, *10*, 4801-4812.

Chapter 4

Nishimoto, Y.; Irle, S. “Simulation of Vibrational Spectra of Large Molecular Systems with Radical or Metallic Electronic Structure”, to be submitted.

Chapter 5

Nishimoto, Y.; Yokogawa, D.; Yoshikawa, H.; Awaga, K. Irle, S. “Super-Reduced Polyoxometalates: Excellent Molecular Cluster Battery Components and Semipermeable Molecular Capacitors”, *J. Am. Chem. Soc.* **2014**, *136*, 9042-9052.

Other Publications

1. Wang, Y.; Page, A. J.; Nishimoto, Y.; Qian, H.-J.; Morokuma, K.; Irle, S. “Template Effect in the Competition between Haeckelite and Graphene Growth on Ni(111): Quantum Chemical Molecular Dynamics Simulations”, *J. Am. Chem. Soc.* **2011**, *133*, 18837-18842.
2. Lundberg, M.; Nishimoto, Y.; Irle, S. “Delocalization Errors in a Hubbard-like Model: Consequences for Density-Functional Tight-Binding Calculations of Molecular Systems”, *Int. J. Quant. Chem.* **2012**, *112*, 1701-1711.
3. Nishimoto, Y.; Wang, Z.; Morokuma, K.; Irle, S. “Molecular and electronic structures of endohedral fullerenes, $\text{Sc}_2\text{C}_2@C_{3v}\text{-C}_{82}$ and $\text{Sc}_2@C_{3v}\text{-C}_{82}$: Benchmark for SCC-DFTB and proposal of new inner cluster structures”, *Phys. Status Solidi B* **2012**, *249*, 324-334.
4. Wang, H.; Hamanaka, S.; Nishimoto, Y.; Irle, S.; Yokoyama, T.; Yoshikawa, H.; Awaga, K. “In Operando X-ray Absorption Fine Structure Studies of

Polyoxometalate Molecular Cluster Batteries: Polyoxometalates as Electron Sponges”, *J. Am. Chem. Soc.* **2012**, *134*, 4918-4924.

5. Irle, S.; Page, A. J.; Saha, B.; Wang, Y.; Chandrakumar, K. R. S.; Nishimoto, Y.; Qian, H.-J.; Morokuma, K. “Atomistic mechanism of carbon nanostructure self-assembly as predicted by nonequilibrium QM/MD simulations”, *Practical Aspects of Computational Chemistry II: An Overview of the Last Two Decades and Current Trends*, Springer-European Academy of Sciences, **2012**.
6. Lim, H. E.; Miyata, Y.; Kitaura, R.; Nishimura, Y.; Nishimoto, Y.; Irle, S.; Warner, J. H.; Kataura, H.; Shinohara, H. “Growth of carbon nanotubes via twisted grapheme nanoribbons”, *Nat. Comm.* **2013**, *4*, 2548-2554.
7. Nishimoto, Y.; Yoshikawa, H.; Awaga, K.; Lundberg, M.; Irle, S. “Theoretical investigation of molecular and electronic structure changes of the molecular magnet Mn₁₂ cluster upon super-reduction”, *Phys. Status Solidi RRL* **2014**, *8*, 517-521.